

Development of Metal 3D-Printed Helium-Filled Soap Bubble Nozzles

by

Paul Allen Swiney

A thesis submitted to the Graduate Faculty of
Auburn University
in partial fulfillment of the
requirements for the Degree of
Master of Science

Auburn, Alabama
December 12, 2020

Keywords: Helium-Filled Soap Bubbles, Particle Image Velocimetry, Additive
Manufacturing, Laser-Powder Bed Fusion, Computed Tomography

Copyright 2020 by Paul Allen Swiney

Approved by

Vrishank Raghav, Chair, Assistant Professor of Aerospace Engineering
Brian Thurow, W. Allen and Martha Reed Professor of Aerospace Engineering
Bart Prorok, Professor of Materials Engineering

Abstract

Particle Image Velocimetry (PIV) is a useful flow visualization technique to obtain instantaneous velocity measurements of a fluid. The use of traditional tracer particles for PIV measurements is limited to small field of view measurements. This is due to the fact that the illumination source energy is nominally low, and these particles have a finite scattering efficiency. One solution to overcome this limitation is to use neutrally buoyant helium-filled soap bubbles (HFSBs) as tracer particles. HFSBs have a higher light scattering intensity than traditional tracer particles, enabling larger field of view measurements for PIV. A HFSB system was designed and fabricated at Auburn University to enable velocity field measurements. Using knowledge of previous HFSB nozzle designs, a HFSB orifice nozzle was designed to be completely fabricated using a metal 3D printer. Additive manufacturing can be used to print multiple HFSB nozzles quickly and cost-effectively with little post-processing required. The HFSB nozzle was characterized by its bubble diameter and production rate as a function of air, helium, and soap flow rates. This characterization was compared to other working HFSB nozzles in literature to ensure the metal 3D printed nozzles produced comparable results. Models representing the bubble diameter based on the flow rates to one of the nozzles were created using a linear regression analysis. Finally, the robustness of metal additive manufacturing as a solution to produce consistent HFSB nozzles was evaluated using computed tomography. The nozzles presented in this thesis are the first metal 3D printed HFSB nozzles to not require modifications after printing that successfully produced helium-filled soap bubble tracer particles.

Acknowledgments

The research presented in this thesis could not have been completed without the help and support of many people. I would like to express my sincerest gratitude to my advisor, Dr. Vrishank Raghav for his guidance in the completion of this research. I am extremely grateful for his support, guidance, and knowledge that has helped me improve both technically through my research abilities and through communication and professional skills which are essential to my future career. I would also like to thank Dr. Brian Thurow and Dr. Bart Prorok for their willingness to serve on my committee and the knowledge they have provided.

I would like to thank all members of the Applied Fluids Research Group for their help and knowledge they have provided during my time as a graduate student. I specifically would like to thank Harrison Taylor for his extensive help with conducting experiments on this project. I wish to thank Ralf Fischer for all of his work in 3D printing the nozzles and his assistance on the project, as well as Andrii Shmatok for his help with analyzing the CT scans for this research. I would like to thank Andy Weldon for his machining expertise and making any parts that I needed for this project.

Lastly, I would like to thank my parents George and Virginia Swiney and my girlfriend Reagan Mosley for all the support and encouragement of my education throughout graduate school.

Table of Contents

Abstract	ii
Acknowledgments	iii
List of Figures	vi
List of Tables	x
List of Symbols	xi
1 Introduction	1
2 Background	3
2.1 Particle Image Velocimetry	3
2.2 Helium-Filled Soap Bubbles	5
3 Methods	8
3.1 Additive Manufacturing	8
3.2 Nozzle Designs	9
3.2.1 Preliminary 3D Printed Nozzles	10
3.2.2 3D Printed Nozzle Design	15
3.3 Fluid Supply Unit	16
3.4 Characterization of HFSB Diameter and Production Rate	22
3.5 Computed Tomography Methods	26
3.6 Statistical Methods	28

4	Results	30
4.1	Effect of operating parameters on nozzle performance	30
4.1.1	Influence of Air Flow Rate	30
4.1.2	Influence of Helium Flow Rate	34
4.1.3	Influence of Soap Flow Rate	35
4.1.4	Linear regression model for HFSB diameter	37
4.2	Performance consistency of 3D printed nozzles	39
4.2.1	Consistency of nozzle performance parameters across 3D printed nozzles	40
4.2.2	Relationship between internal surface roughness and nozzle performance	43
4.3	Benchmarking nozzle performance	47
5	Conclusion	51
6	Future Work	52
	References	54
	Appendices	61
A	Drawing of Final Integrated Nozzle Design	61
B	Tested Flow Rates and Bubble Characteristics	62
C	FFT Production Rate Plots	64
D	Computed Tomography Scans	65
E	SAS Figures	67
F	Parts List	77
G	MATLAB Code	79

List of Figures

Figure 1	2D PIV setup in a wind tunnel. Taken from Raffel et al. [1]	4
Figure 2	Example of a HFSB Pitot style nozzle	5
Figure 3	Large body aircraft cabin seeded with HFSB tracers (left) and the average flow velocities of airflow within the cabin using PIV (right). Taken from Müller et al. [2]	6
Figure 4	GE Concept Laser Mlab cusing R metal 3D printer used to print HFSB nozzles (left) and 3D printer scanning strategies that were implemented to print the HFSB nozzles (right)	9
Figure 5	3D printed stainless steel orifice nozzle with machined cap (left), 3D printed nozzle without the orifice cap (center), and wireframe drawing of 3D printed nozzle showing internal design (right)	10
Figure 6	3D printed nozzle cutout showing internal design	11
Figure 7	CAD drawing cutaway depicting gap distance between cap and nozzle and the height difference between the soap and helium tube	12
Figure 8	Shadowgraph images depicting the bubble diameters for the HFSB nozzle with a machined cap. The left image depicts two HFSB nozzles operating. The right top images depict one HFSB nozzle operating with its corresponding HFSB diameter while the right bottom image shows the shadowgraph setup.	12
Figure 9	3D printed nozzle and cap with four air exits	13
Figure 10	3D printed nozzle and cap with air ring	14
Figure 11	3D printed nozzle with air ring without cap	14
Figure 12	HFSB integrated cap and nozzle design picture (left) and shaded section drawing of the nozzle (right)	15
Figure 13	Fluid supply unit setup controls the flow rates of air, helium, and soap solution. The soap pressure vessel in the far-right image was placed inside the large aluminum pipe behind the flow meters and valves.	17

Figure 14	HFSB fluid supply unit schematic diagram showing the main components. All components are connected with 1/8" OD plastic tubing with push-to-connect fittings.	18
Figure 15	Soap valve calibration with Sage Action soap depicting the flow rate through the valve for different Vernier valve settings	20
Figure 16	Setup of the 3D calibration plate used to calibrate the camera from the image space in pixels to the physical space in millimeters (top), and shadowgraph setup to record illuminated images of HFSBs (bottom)	23
Figure 17	Shadowgraph image of HFSBs using the integrated nozzle and Sage Action soap solution	24
Figure 18	Location on HFSB nozzle where the surface roughness was analyzed from CT scans	26
Figure 19	XCT scan of the HFSB nozzle showing how it is rotated while being scanned	27
Figure 20	Pinnacle X-ray Solutions 500/90 XLW XCT cabinet used to evaluate HFSB nozzles	28
Figure 21	Average diameter and standard deviations of HFSBs (mm) for varying air flow rates (L/h). These bubble diameters were recorded for approximately neutrally buoyant flow conditions at optimal air flow rates for nozzle 1.	31
Figure 22	Diameter of HFSBs (mm) for varying air flow rates (L/h) for all flow conditions for nozzle 1. The shaded regions depict the different flow regimes corresponding to the HFSB images at the right side. The optimal air flow rate for the 3D printed nozzles is depicted in the center green shaded region which had the best and most consistent bubble diameter and production rate. (a) Bubbling regime with optimal air flow rate, (b) bubbling regime with a low air flow rate, (c) transitioning to jetting regime, (d) jetting regime with a high air flow rate.	32
Figure 23	Diameter of HFSBs (mm) for varying air flow rates (L/h) for all flow conditions for nozzle 1. Each plotted line represents a different He:Soap ratio. The range of He:Soap ratios from 901 to 1083 have standard deviations shown.	33
Figure 24	Production rate of HFSBs (bubbles/s) for varying air flow rates (L/h) averaged for ten metal 3D printed nozzles at neutrally buoyant He:Soap flow conditions	34
Figure 25	Diameter of HFSBs (mm) for varying helium flow rates (L/h) while the soap flow rate was held constant at 10.50 mL/h, 12.62 mL/h, and 15.23 mL/h	35

Figure 26	Diameter of HFSBs (mm) for varying soap flow rates (mL/h) while the helium flow rate was held constant at 11.37 L/h, 17.05 L/h, and 22.74 L/h	36
Figure 27	HFSB diameter is linearly proportional to the ratio of helium to air flow rates. The bubble diameter data for the metal HFSB nozzle was compared to the proportionality equation published in Faleiros et al.'s paper.	38
Figure 28	HFSB diameter and standard deviation for each metal 3D printed nozzle for He:Soap = 981 and 1083 at an air flow rate of 152.27 L/h	40
Figure 29	FFT production rate plots of two HFSB nozzles that had the worst internal surface roughness (top) and two nozzles that had the best surface roughness (bottom)	41
Figure 30	HFSB production rate and standard deviation for each metal 3D printed nozzle for He:Soap = 981 and 1083 at an air flow rate of 152.27 L/h	42
Figure 31	Normalized surface area of each 3D printed nozzle in relation to its deviation from the nominal surface of the inside of the HFSB nozzle	44
Figure 32	CT scan of the analyzed region of nozzle 1 depicting a rather smooth overhanging cap surface (left), and the CT scan of nozzle 2 depicting a large dimple and a spike on the surface of the cap (right)	45
Figure 33	HFSB diameter for each metal 3D printed nozzle at He:Soap = 981 (top) and He:Soap = 1083 (bottom) versus the internal surface roughness deviation at the 90 th percentile	45
Figure 34	HFSB production rate for each metal 3D printed nozzle at He:Soap = 981 (top) and He:Soap = 1083 (bottom) versus the internal surface roughness deviation at the 90 th percentile	46
Figure 35	The average diameters and standard deviations for various HFSB produced from different nozzles published in literature are depicted. The x-axis has the last name of the primary author and year of the paper that the data was obtained from, and the y-axis is the HFSB diameter in millimeters. Papers that published a HFSB diameter above 1 mm are not shown in this plot (Müller [2] - 2 mm, Macháček [3] - 2-4.5 mm, Sun [4] - 1.3-3 mm, Lobutova [5] - 4 mm, Borer [6] - 2-3 mm, Sage Action Inc. - 1-4 mm).	48

Figure 36	The ranges of production rates from different nozzles published in literature are depicted. The x-axis has the last name of the primary author and year of the paper that the data was obtained from, and the y-axis has the production rate in bubbles/s. An average of the ten metal 3D printed nozzles used in this study is shown by the far-right data points and the ranges that were observed at neutrally buoyant flow conditions is shown by error bars. Other papers that published a HFSB production rate below 1,000 bubbles/s or above 120,000 bubbles/s are not shown in this plot (Bosbach [7] - 200,000 bubbles/s, Macháček [3] - 500-700 bubbles/s, Borer [6] - 5-10 bubbles/s, Sage Action Inc. - 300-400 bubbles/s).	50
Figure 37	CAD drawing of final HFSB nozzle design	61
Figure 38	FFT production rate plots for all HFSB nozzles	64
Figure 39	CT scans depicting the surface deviation for the analyzed region of the cap for all ten 3D printed HFSB nozzles	66
Figure 40	Neutrally buoyant fit plot for air flow rate in SAS	67
Figure 41	Neutrally buoyant SAS data	68
Figure 42	Neutrally buoyant SAS data	69
Figure 43	Neutrally buoyant SAS data	70
Figure 44	Neutrally buoyant SAS data	71
Figure 45	Neutrally and non-neutrally buoyant fit plot for air flow rate in SAS	72
Figure 46	Neutrally and non-neutrally buoyant SAS data	73
Figure 47	Neutrally and non-neutrally buoyant SAS data	74
Figure 48	Neutrally and non-neutrally buoyant SAS data	75
Figure 49	Neutrally and non-neutrally buoyant SAS data	76
Figure 50	MATLAB code for calculating HFSB diameters	80
Figure 51	MATLAB code for calculating production rate using FFT	84

List of Tables

Table 1	Tested flow rate values of air, helium, and soap to the nozzle	22
Table 2	3D printed nozzles' surface roughness deviations for the inside of the HFSB nozzle at the 90 th , 95 th , and 98 th percentiles	44
Table 3	3D printed HFSB nozzle's average bubble diameters, production rates, standard deviations, and internal surface roughness deviations at two He:Soap ratios	47
Table 4	Tested flow rate ranges and bubble characteristics with sample HFSB images	63
Table 5	Parts list for HFSB system	78

List of Symbols

$3D$	three-dimensional
μA	microamp
μm	micrometer
μs	microsecond
ρ	density
AM	additive manufacturing
CAD	computer aided design
CT	computed tomography
d	diameter
f	bubble production frequency
FFT	fast Fourier transform
fps	frames per second
h	hour
$HFSB$	helium-filled soap bubble
Hz	hertz
kg	kilogram
kV	kilovolt
L	liter
$L - PBF$	laser-powder bed fusion

<i>m</i>	meter
<i>mL</i>	milliliter
<i>mm</i>	millimeter
<i>ms</i>	millisecond
<i>mW</i>	milliwatt
<i>N</i>	newton
<i>NTP</i>	normal temperature and pressure
<i>P</i>	pressure
<i>Pa</i>	pascal
<i>PCC</i>	Phantom Camera Control
<i>PIV</i>	particle image velocimetry
<i>psig</i>	pound-force per square inch gauge
<i>PTC</i>	push-to-connect
<i>Q</i>	flow rate
<i>R²</i>	coefficient of determination
<i>s</i>	second
<i>SCFH</i>	standard cubic feet per hour
<i>SG</i>	specific gravity
<i>T</i>	temperature
<i>V</i>	volume
<i>W</i>	watt
<i>XCT</i>	x-ray computed tomography

Chapter 1

Introduction

Fluid dynamics research is essential to improve the design and development of aircraft, unmanned aerial vehicles, ground vehicles, sports equipment, and many other engineering applications that are used by people every day. Analyzing air flows, especially with large field of views and large volumes is essential for many engineering applications, such as studying helicopters in ground-effect or the flow around drones near walls. Particle Image Velocimetry (PIV) is now one of the most used measurement techniques for flow diagnostics in aerospace and fluid dynamics research. PIV is used to visualize the velocity field in a 2D plane or 3D volume by measuring the displacement of small tracers that follow the motion of the fluid being analyzed. However, one of the limitations to using PIV is the size of the analyzed measurement volume is limited when using small tracer particles. One solution to enable large-scale flow visualization is to use helium-filled soap bubbles (HFSBs) as tracer particles due to their larger diameter than traditional tracers.

Even though there have been HFSB designs that generated large bubbles (larger than 1 mm in diameter) that were neutrally buoyant [2–6], most PIV applications need very high quantities of small, neutrally buoyant HFSB tracers. In literature, most HFSBs are less than 1 mm in diameter, as larger bubbles are normally no longer neutrally buoyant. Seeding the measurement flow volume for PIV with sufficient tracer particles is still challenging for large volumes and for experiments conducted with high shear or at high velocities. Gibeau et al.'s solution to this was to use plastic 3D printing to create a modular HFSB nozzle. They characterized their HFSB nozzle by bubble diameters, production rates, seeding density, and the tracing fidelity of the HFSBs [8–10]. However, their solution required the use of syringe needles for the small inner tubes and a cap had to be assembled onto the body of the nozzle. The motivation for this thesis is to design and develop a HFSB nozzle that can be used directly after 3D printing with no modifications, which will reduce the cost and time to print the nozzles.

Commercial HFSB systems are very expensive to purchase. While plastic 3D printing provided one option to make it easier and more cost-effective to produce a multi-nozzle system for a large quantity of HFSBs, post-processing was necessary. Required post processing techniques included adding a syringe needle, metal tubing, and assembling the cap onto the body of the nozzle. Most plastic printers do not have a high printing resolution leading to inconsistent results. The proposed solution to this problem was to use laser-powder bed fusion (L-PBF) on a metal 3D printer which can produce small, intricate parts with a higher dimensional accuracy than plastic printers. The use of metal 3D printers is relatively new, thus several designs and flow characteristics of the nozzle needed to be evaluated to prove that using L-PBF is a viable option to quickly produce working HFSB nozzles. A completely 3D printed HFSB nozzle with almost no post-processing has not been published in literature. Thus, the objective of this thesis is to demonstrate that using metal printing could be the solution.

This thesis describes and characterizes the design and fabrication of a HFSB system for use for time-resolved velocity field measurements. The design of an orifice type nozzle that can be fabricated entirely with a metal 3D printer with sufficient spatial resolution is demonstrated. Metal additive manufacturing enables the HFSB nozzle to be operated immediately after printing with minimal post-processing. Using additive manufacturing is a more cost and time effective technique to manufacture the nozzles. The HFSB nozzle is characterized by recording the bubble diameter and production rate as a function of air, helium, and soap solution flow rates to the nozzle. Using the recorded bubble diameters and production rates, the HFSB nozzles is benchmarked against other working HFSB nozzles reported in literature to validate that it was comparable or better than other working designs. Microcomputed tomography is used to characterize the internal surface roughness and the print consistency between nozzles. The HFSB nozzle performance is correlated to the surface roughness results from the scans to find any existing relations between nozzle performance and surface roughness.

Chapter 2

Background

This chapter covers the fundamentals of Particle Image Velocimetry (PIV) and helium-filled soap bubbles (HFSBs). First, this chapter will discuss the basic concepts of PIV and how it is traditionally applied to study air flows. This section will also discuss the limitations of traditional PIV and how using HFSBs can be used as a solution to these limitations. The next section discusses how HFSBs are produced and how they have been applied to PIV in literature.

2.1 Particle Image Velocimetry

PIV is a flow quantification technique used to measure instantaneous velocity fields. The fluid being analyzed is populated with tracer particles and is illuminated with a laser so the particles are visible to a high-speed camera. These tracer particles are very small, on the order of a couple microns, to assume they follow the flow perfectly. The motion of the particles is then used to calculate the velocity of the flow being studied. Oil and Di-Ethyl-Hexyl-Sebacat (DEHS) droplets are very stable and easy to track, thus they work well for small-scale turbulent flow measurements, whereas fog particles work well for local-seeding applications that need a very high concentration of particles [11].

Planar PIV uses a thin laser sheet to illuminate the tracer particles. The light scattered by the tracer particles is captured on multiple frames by a high-speed camera that has been calibrated and focused on the tracer particles. Figure 1 illustrates a 2D planar PIV setup in a wind tunnel.

Since its recent introduction in the last couple of decades, the application of time-resolved volumetric PIV has increased over time [12]. Volumetric or tomographic PIV is a 3D PIV technique that can analyze the motion of the tracer particles within a 3D measurement volume. This is usually performed by using 4 or more high-speed cameras aimed at the measurement volume. Volumetric PIV has been used to investigate flow fields in several engineering applications [1, 11, 13]. However, one of the primary limitations to this technique is the size of

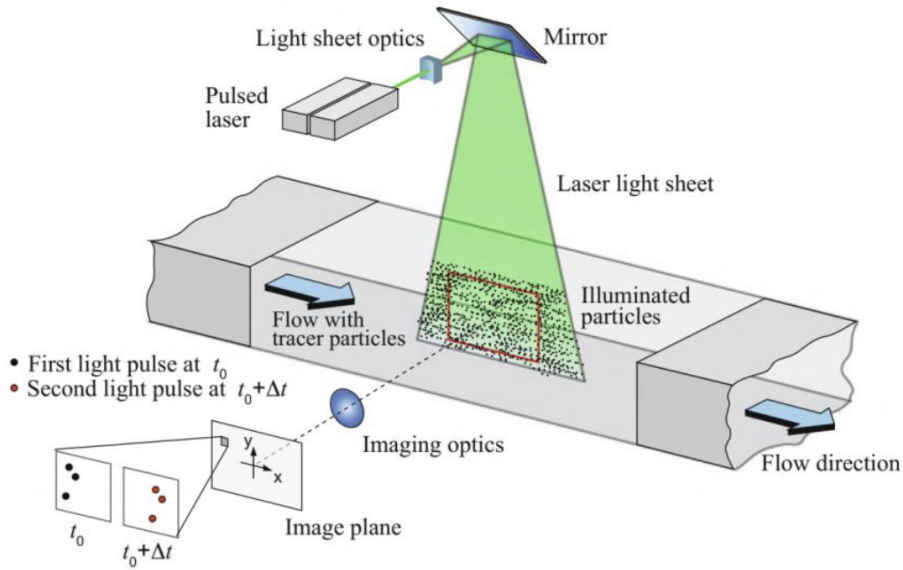


Figure 1: 2D PIV setup in a wind tunnel. Taken from Raffel et al. [1]

the measurement volume that can be analyzed. This is especially true for air flows due to the limitation in available illumination energy by a laser and the finite light scattering efficiency of micron-sized traditional tracer particles [3, 14, 15]. For large-scale and tomographic PIV studies, the laser illumination intensity is a lot less than for planar PIV due to the laser beam sheet expanding through a large cross-sectional area. For tomographic PIV, the high-speed cameras are focused on the tracer particles throughout the entire measurement depth. To achieve a large depth of focus, generally a small optical lens aperture is used, which further reduces the amount of light transmitted to the camera sensor [16].

While these micron-sized tracer particles, such as smoke, work well for small field of view flow measurements, they are not effective for large field of view flow measurements. One potential solution is to increase the light scattering intensity by using larger particles, such as neutrally buoyant helium-filled soap bubbles (HFBSBs). HFBSBs reflect 10^4 more light than traditional tracers due to the bubble's reflectivity and their larger size [17]. This increase in light scattering intensity enables PIV at larger field of views, up to $12.6m^2$ [14, 18].

2.2 Helium-Filled Soap Bubbles

HFSBs are bubbles filled with helium to counteract their weight to enable neutral buoyancy. These bubbles are normally produced by nozzles that combine helium and soap together using concentric tubes. Two types of HFSB nozzles were defined by Okuno et al.: a Pitot and an orifice nozzle [19]. The Pitot type nozzle was developed first and is limited in its bubble production rate to only hundreds of bubbles per second [7, 19]. Inside of the Pitot nozzle there are two concentric tubes, the inner center tube supplies a flow of helium and the outer tube supplies the nozzle with the soap solution. There is a supply of air behind the soap and helium tubes to detach the bubbles formed at the tip of the nozzle. An example of a Pitot style nozzle is shown in Fig. 2.

A high bubble production rate is needed for PIV applications, especially to analyze large measurement volumes. Thus, a new technique using an orifice type nozzle was created by Okuno et al. [19] and developed further by Flögel [3, 20] in the 1990s. The orifice nozzle only slightly differs from the Pitot nozzle in the fact that it has a cap that fits over the top of the nozzle. This creates a

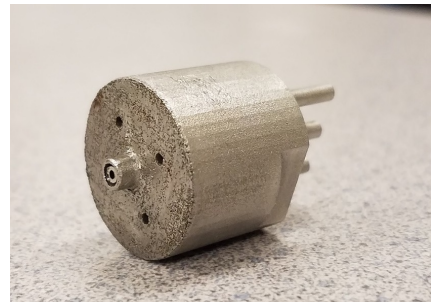


Figure 2: Example of a HFSB Pitot style nozzle

hollow chamber above the helium and soap tubes where the air is supplied. At the tip of these concentric tubes the bubbles are formed. Due to the supplied air in the chamber, the bubbles detach from the tubes and are forced through a small exit hole in the center of the orifice cap. The orifice type nozzle is capable of producing HFSBs at a higher production rate than the Pitot nozzle. In addition, controlling the bubble diameter is easier due to the orifice cap [7, 19]. For accurate PIV experiments, it is generally desired to have a minimum seeding density of 10 bubbles per interrogation window and the HFSBs to be larger than 1 pixel in diameter in the camera space [21]. Several different variations to the internal geometry of orifice nozzles have been designed and tested, with researchers testing the effects that air cavities within the cap and filleted cap edges have on the performance of the HFSB nozzle [10, 22, 23].

The HFSB orifice nozzle was first used by Okuno et al. to analyze air conditioning flow inside a passenger vehicle, but the first nozzle only produced 3,000 bubbles per second [19]. The orifice nozzle was then successfully used by Müller et al. who performed PIV measurements on air conditioning flow in a large-body aircraft, depicted in Fig. 3 [2, 24]. Since then, many researchers studying fluids have applied HFSBs as tracer particles to record velocity field measurements of large volume air flows [15, 25] in wall-bounded turbulence [26], through pipes and around objects [22, 23, 27, 28], in jet flows [29–31], and in aircraft cabins [2, 4, 7, 14]. Bodstein et al., Caridi, and Politz et al. proved that HFSBs can be applied to high-shear flow applications by studying vortices [32–34].

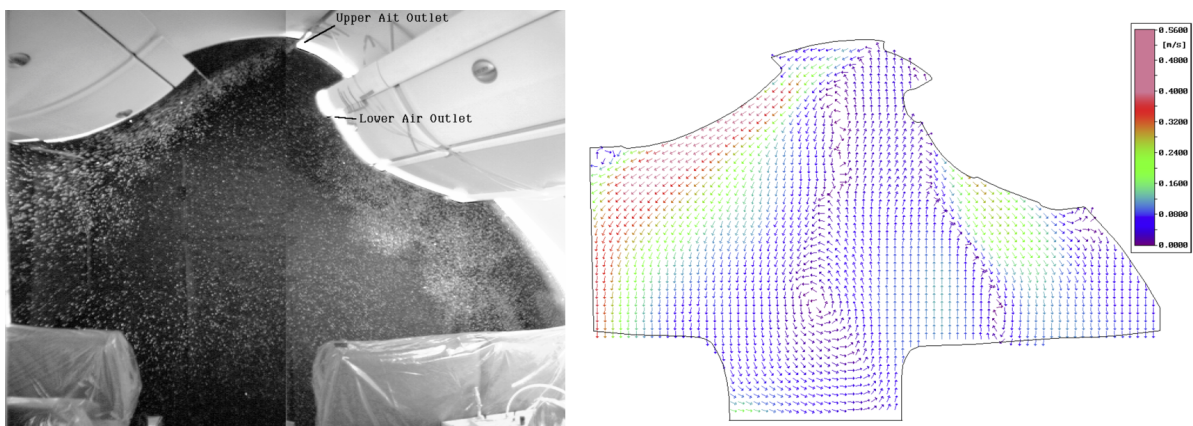


Figure 3: Large body aircraft cabin seeded with HFSB tracers (left) and the average flow velocities of airflow within the cabin using PIV (right). Taken from Müller et al. [2]

With the goal of applying HFSBs to fast moving fluids in large volumes, such as in a wind tunnel [3, 12, 17, 35, 36], several researchers have worked on increasing the HFSB production rate and improving the visibility of the bubbles. HFSBs can be used for a variety of applications outside the lab and in real-life scenarios. Herrero et al. applied HFSBs to visualize the flow on an untethered, free-flying, flapping-wing micro air vehicle when flying in a wind-tunnel [37]. Due to the increase in research with HFSBs, more real-life fluid applications can be studied. Some other real-life applications are to measure the aerodynamics of ground vehicles [16, 38], how athletes perform while playing sports [39], and even in medical research [40].

Several research papers have analyzed how well HFSBs follow the flow being studied and have concluded they work well as tracer particles as long as they are neutrally buoyant [12, 22, 41]. If the bubbles are too light or too heavy, they will not accurately follow the same

trajectory as the air particles in the measurement volume. Faleiros et al. [22] did experiments measuring the bubble slip velocity along the stagnation streamline ahead of a cylinder to explain how heavier-than-air bubbles decelerate slower from the pressure gradient due to their inertia, and lighter-than-air bubbles respond faster than air due to their smaller inertia force.

Chapter 3

Methods

3.1 Additive Manufacturing

Additive manufacturing, or 3D printing, is the construction of objects using a 3D CAD drawing and a 3D printer that can take the CAD model and form the object. 3D printers can use a variety of materials to print objects, such as plastics, resins, rubbers, and metals. A variety of 3D printing techniques exist, including selective laser sintering, selective laser melting, stereolithography, fused deposition modeling, and laser-powder bed fusion. One of the leading additive manufacturing (AM) technologies is laser-powder bed fusion (L-PBF), due to its ability to process various materials with high accuracy and good surface finish [42,43]. L-PBF forms parts by spreading thin layers of metal powder and fusing it with a laser. L-PBF has the ability to print highly complex parts with internal features, which was taken advantage of when designing the HFSB nozzle [43,44].

Using a Concept Laser Mlab cusing R, shown in Fig. 4, ten HFSB nozzles were printed using 316L stainless steel powder. The printing process parameters used on the 3D printer were 90 W laser power, 600 mm/s scan velocity, 80 μm hatch spacing, and 25 μm layer thickness. All nozzles, excluding nozzle 2, were printed with the exposure strategy set to continuous, and for nozzle 2 the island exposure strategy was employed. During the island scan strategy, each layer of the printed part is divided into squares, or “islands”, creating a checkerboard pattern. Each of these “islands” is then selectively melted by the laser in a random order. The laser direction in neighboring “islands” are perpendicular to each other [45]. For the continuous scan strategy, the laser uses a simple back-and-forth scan pattern across the print bed. A schematic depicting these scan strategies by the 3D printer can be seen in Fig. 4. Each line in the schematic represents the laser path that the printer takes to melt the powder to build the layers of the HFSB nozzles on the printer bed.

The nozzles were printed with different exposure strategies as there was a software issue that caused the internal tubes in the nozzle to sometimes be obstructed with metal powder when

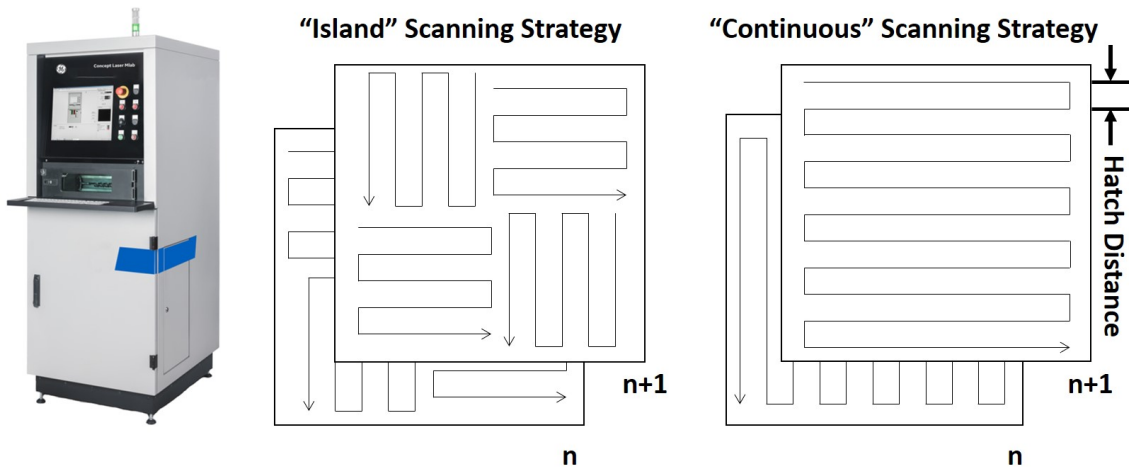


Figure 4: GE Concept Laser Mlab cusing R metal 3D printer used to print HFSB nozzles (left) and 3D printer scanning strategies that were implemented to print the HFSB nozzles (right)

the nozzle was printed with the island strategy. Nozzles 3-10 were all printed at the same time, while nozzle 1 and 2 were printed by themselves. The print file was generated using Materialise Magics version 20.04. The nozzles' orientation was set to print the tip of the nozzle (where the bubbles exit) facing in the positive Z-direction and the air, helium, and soap inlets were resting on the print bed with printed supports. For the current experiments, the print strategy was not altered to account for the overhanging regions of the nozzle.

3.2 Nozzle Designs

The 3D printed HFSB nozzle discussed in this thesis was designed to be an orifice nozzle to take advantage of the higher bubble production rates. Due to the recent advances in metal additive manufacturing (AM), allowing a higher dimensional accuracy than plastic additive manufacturing, the nozzle was designed to be printed out of stainless steel. Several iterations of the nozzle design were printed and tested before finalizing the 3D printed design. Several changes were made to reduce the amount of metal powder and time needed to print the nozzle as well as to reduce the size of unsupported regions within the nozzle. The nozzles utilized design elements unique to the 3D printing process, such as small internal tubes, that would not be possible if the nozzle was being machined as one part using traditional machining techniques.

3.2.1 Preliminary 3D Printed Nozzles

The preliminary nozzle design had two concentric tubes that ran through the center of the nozzle. The inner tube supplies helium and the outer tube supplies soap to the nozzle, as shown in Fig. 5. The helium enters the nozzle through a 1 mm diameter inlet tube, and the soap enters through a 1.5 mm diameter inlet tube at the bottom of the nozzle. Air enters the nozzle through a 1.5 mm diameter inlet tube that is then diverged to four air outlet holes by using an internal torus inside the nozzle to split the air flow. In order to be an orifice nozzle, the nozzle had a cap placed over it with a 1 mm diameter hole in the center. This hole lined up with the helium tube that ran through the center of the nozzle. This exit hole in the nozzle's cap was one of the parameters that controlled the diameter of the HFSBs. Nozzle caps with a 1.5 and a 2 mm diameter exit hole were also tested, but produced bubbles that were too large with bubble diameters over 1 mm. The cap was machined on a lathe out of aluminum, and had a set screw on the top of the cap that was used to set the distance between the nozzle and the inside of the cap. Two set screws on the sides of the cap were used to hold the nozzle in position within the cap.

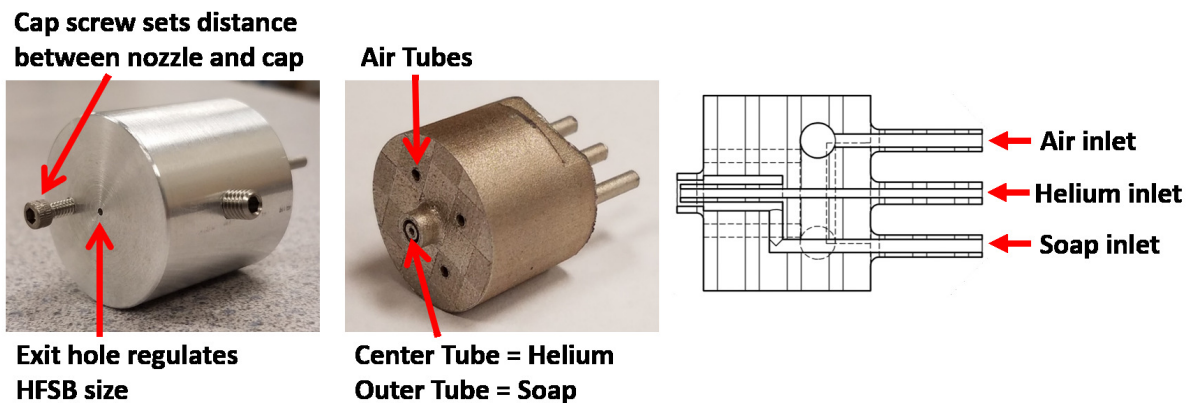


Figure 5: 3D printed stainless steel orifice nozzle with machined cap (left), 3D printed nozzle without the orifice cap (center), and wireframe drawing of 3D printed nozzle showing internal design (right)

After the first HFSB nozzle was 3D printed, the nozzle was cut open to ensure none of the internal tubes were clogged, as depicted in Fig. 6. It was found that some of the small internal soap tubes were clogged with stainless steel powder. To allow the nozzle to be printed on a

metal 3D printer, the design had to be modified to meet the minimum printing specifications for a GE Concept Laser 100 R. All internal tubes were increased to a minimum 1 mm diameter, and a minimum distance of 0.5 mm between tubes to ensure that excess metal powder after printing could be removed and the tubes would not be blocked.

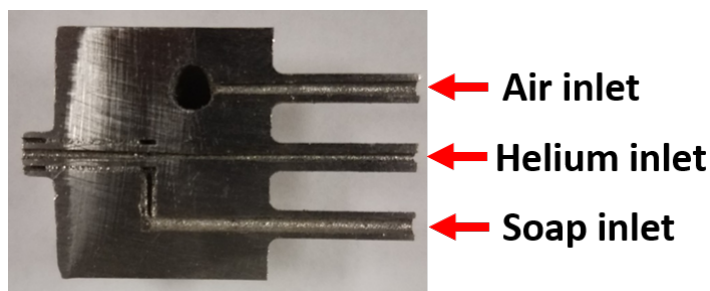


Figure 6: 3D printed nozzle cutout showing internal design

When preliminary experiments with the nozzle were performed, there was a considerable amount of soap leakage that occurred where some of the soap solution being supplied to the nozzle was wasted instead of being used to make HFBSBs. Reducing the soap flow rate to the nozzle was attempted, but failed because it caused the nozzle to sputter. During experiments, it was found when the nozzle was positioned where the bubbles exited vertically in either direction instead of at an angle, it performed best and most consistent, which agrees with Gibeau's et al.'s paper [10]. If the nozzle was operated at an angle with respect to the nozzle's exit, the nozzle frequently became blocked with excess soap and would result in the nozzle sputtering.

To reduce the amount of soap leakage around the nozzle's exit, the design was altered to have the helium tube shorter in height than the soap tube, as depicted in Fig. 7. The optimal height difference between the helium and soap tube was approximated based on prior orifice nozzle designs in literature. Several helium tube heights were tested to determine the best design for the metal 3D printed nozzle. Nozzles that had the helium tube 0.1, 0.37, and 0.4 mm shorter than the soap tube were printed and tested. Among the tested helium tube heights, the nozzles that had a 0.37 mm shorter helium tube improved the consistency of HFBSB production and reduced the most amount of soap leakage.

To ensure the nozzles were producing HFBSBs that were close to the desired diameter of approximately 0.5 mm, the size of the HFBSBs was investigated by using a Cannon 80D with

a Sigma 18-300 mm f3.5-6.3 Contemporary DC Macro OS HSM lens. Using this camera, shadowgraph images of the bubbles, such as the one shown in Fig. 8 were captured. A Canon hot-shoe flash was used to illuminate the bubbles from behind the nozzle. The diameter of the bubbles was approximated to be 0.45 mm from the captured images. This confirmed the nozzle was capable of producing HFSBs that could be used for PIV experiments if the production rate and consistency of the bubbles was improved.

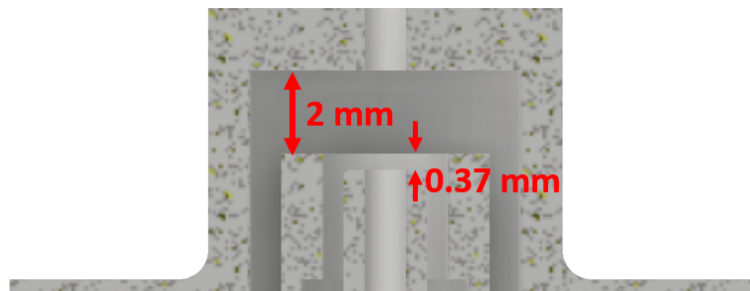


Figure 7: CAD drawing cutaway depicting gap distance between cap and nozzle and the height difference between the soap and helium tube

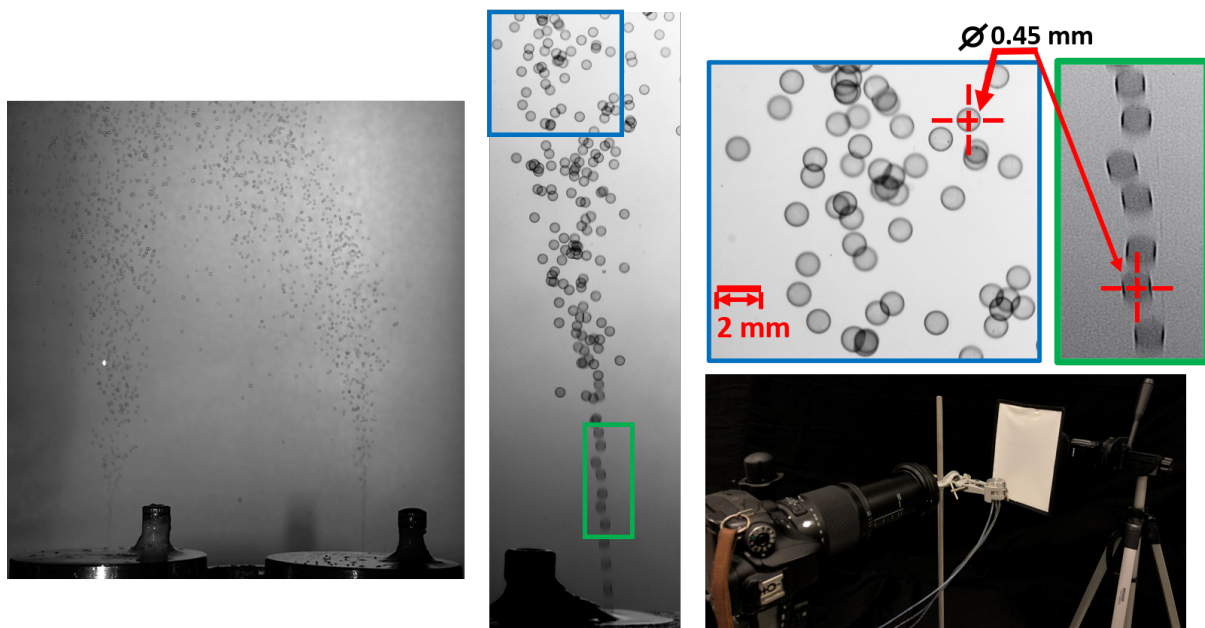


Figure 8: Shadowgraph images depicting the bubble diameters for the HFSB nozzle with a machined cap. The left image depicts two HFSB nozzles operating. The right top images depict one HFSB nozzle operating with its corresponding HFSB diameter while the right bottom image shows the shadowgraph setup.

Before an integrated nozzle and cap design could be printed as one part, the optimal gap distance between the nozzle exit and the cap had to be determined. When the cap is printed on

the nozzle, the gap distance is fixed, so testing at various gap distances was done to determine the best distance. Gap distances from 0.5 to 3 mm were tested using the preliminary nozzle design. Figure 7 depicts the optimal gap distance between the nozzle and the cap to be 2.0 mm. This distance produced the most consistent bubble production and smallest variation in HFSB diameters. Smaller gap distances reduced the HFSB production rate and increased bubble diameter variation, while larger gap distances produced larger diameter HFSBs where the bubbles were no longer neutrally buoyant.

To design and test a completely 3D printed nozzle made out of metal, the previous nozzle design that included a machined cap needed to be modified. Due to 3D printing limitations, the cap was too large of an unsupported structure to be printed on the nozzle without support structures. Figure 9 and Fig. 10 depict two different combined nozzle and cap designs that were drawn in Autodesk Inventor with internal supports inside the cap. The first design placed rhombus-shaped support structures inside the cap, leaving space around the air, helium, and soap tubes, shown in the CAD drawings in Fig. 9b and Fig. 9c.

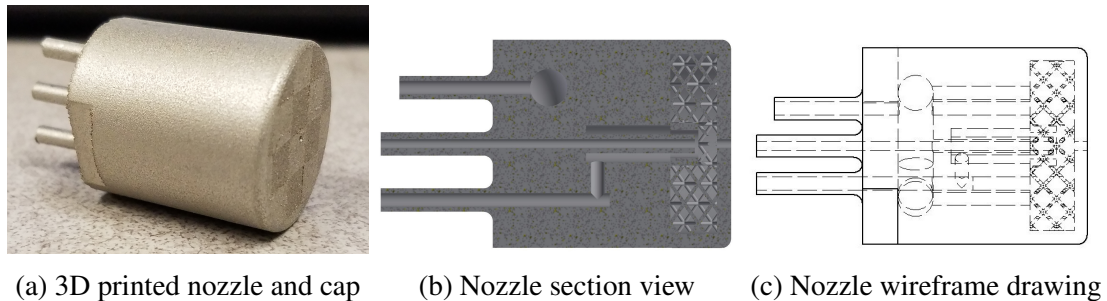


Figure 9: 3D printed nozzle and cap with four air exits

There was concern that these support structures would have interfered with the air flow between the cap and the nozzle, as Gibeau et al.'s paper depicted how changes in air circulation alter the nozzle's performance [10]. The air outlets' purpose was to supply air to the orifice chamber, thus it was hypothesized that changing the design from having four air outlets to having a concentric ring around the helium and soap tubes to supply the air into the cap would not prevent the nozzle from working. This design change only altered where the air exited the nozzle and entered the orifice chamber, in turn moving the air outlet closer to the center of the nozzle. There were three concentric tubes, a helium tube in the center, a soap tube, and then

an air tube on the outermost circle, which can be seen in Fig. 10b and Fig. 10c. This allowed for the cap to be filled with rhombus-like support structures with a 6 mm diameter center circle area without support structures. These nozzle designs looked better aesthetically than printing the nozzle and placing a machined cap over the top of it, as well as eliminating the need to manually machine a cap for each nozzle. The helium tube within the nozzle and the bubble exit hole in the printed cap were lined up and all internal tubes inside the nozzle were clear from obstructions. This validated that the 3D printer had the necessary spatial resolution to print the design. Figure 11 depicts this nozzle design printed without the cap. The nozzle was printed without the cap to allow this design to be tested with the machined caps to ensure the air ring did not negatively affect the nozzle's performance. After testing, there was no noticeable difference in bubble diameter or production consistency when using the nozzle with the air ring design.

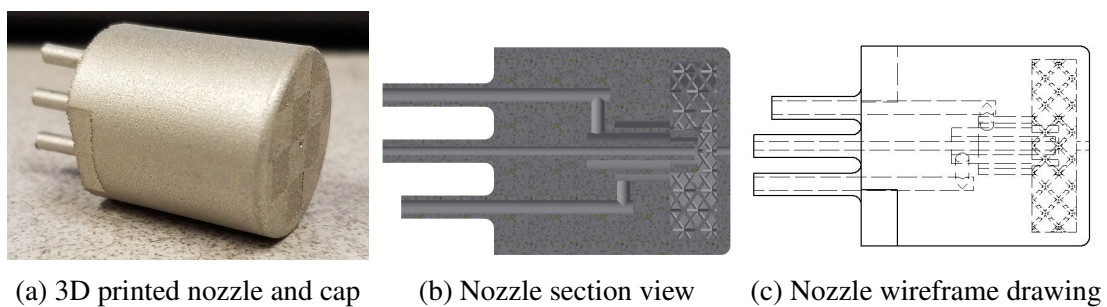


Figure 10: 3D printed nozzle and cap with air ring

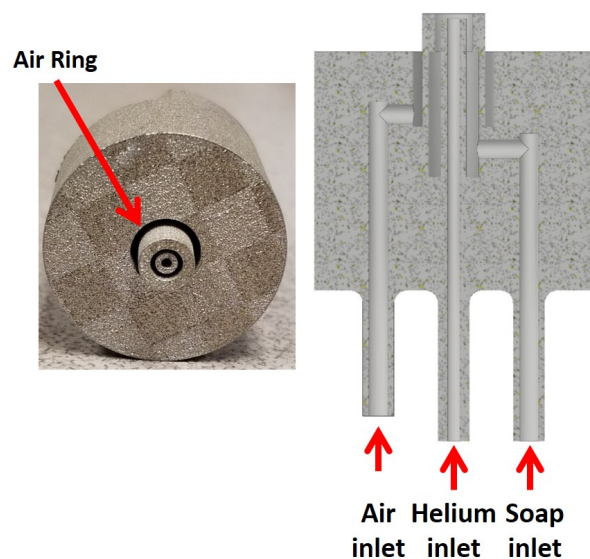


Figure 11: 3D printed nozzle with air ring without cap

3.2.2 3D Printed Nozzle Design

The objective of the final design was to print the cap and nozzle as one integrated design which could be used directly after printing with no post processing. To achieve this, the preliminary nozzle was optimized to reduce the size of the cap. Reducing the cap size allowed it to be printed on top of the nozzle without internal support structures, which could have interfered with the air flow between the cap and nozzle. Changing the four air outlet holes in the nozzle to an air ring that was concentric to the soap and helium tubes allowed the internal torus to be removed from the design. This permitted the diameter of the nozzle to be reduced due to no internal features being near the outside of the nozzle. The nozzle reduced in size from a 31.75 mm diameter cylinder to a 10 × 18 mm rectangular prism as depicted in Fig. 12. The air inlet tube was designed to be slightly shorter in length to differentiate between the air and soap inlet tubes when installing the nozzle to the HFSB system. Sharp edges on the outside of the nozzle where metal was joined at a 90-degree angle had a fillet added to reduce stress concentrations and better join the surfaces during 3D printing.

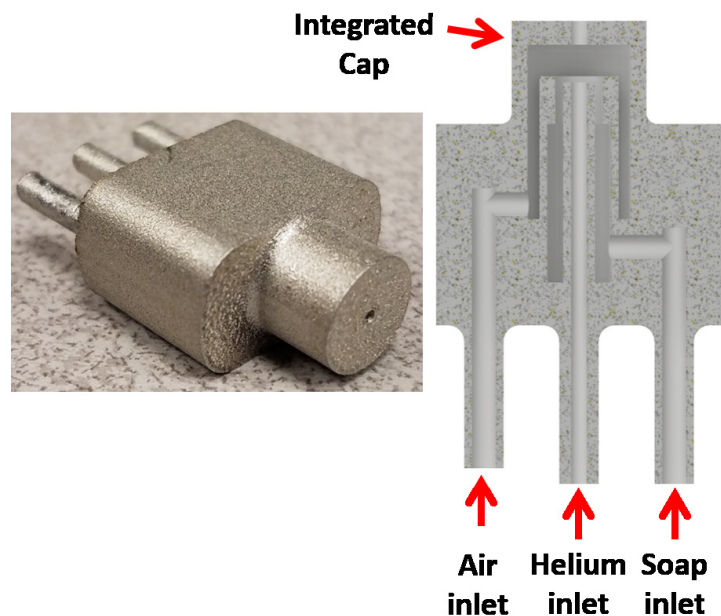


Figure 12: HFSB integrated cap and nozzle design picture (left) and shaded section drawing of the nozzle (right)

The cap and nozzle were successfully printed, as one part as shown on the left side of Fig. 12. This final integrated design was produced faster and cheaper than traditional machining

methods, and was more cost-effective than purchasing a commercially available system. The only post-processing required was to remove the nozzle from the external supports that were printed on the side of the air, helium, and soap inlets and to place the nozzle in an ultrasonic bath to remove any residual stainless steel powder left inside the nozzle. When compared to the first preliminary nozzle, this design used 66.5% less stainless steel powder and reduced the print time by 35%, from 5.25 to 3.5 hours.

Another advantage of the smaller nozzle design was more nozzles could be printed at once on the 3D printer bed, improving the overall printing efficiency. Multiple HFSB nozzles need to be operating at once for most PIV applications to achieve a high enough seeding density of tracers. The smaller nozzle design enabled multiple nozzles to be placed side-by-side during bubble production to reduce the size of the setup. Experiments were performed with the final design to verify that the smaller integrated cap did not cause any adverse changes to the bubble diameters or production consistency of the nozzles. A drawing of the final orifice nozzle is provided in Fig. 37 in the appendix.

3.3 Fluid Supply Unit

When using HFSBs for PIV experiments, the nozzle needs to be producing bubbles continuously as bubbles have a life of approximately 1-2 minutes. The fluid supply unit uses two Dwyer flow meters (RMA-1-BV and RMA-4-BV) to regulate the air and helium flow rate to the nozzle. Air is used to separate the HFSBs from the tip of the nozzle after they have formed and then forces the bubbles through the exit hole in the orifice cap. Helium is inserted inside of the bubbles to offset the weight of soap so they are neutrally buoyant. The helium also pressurizes the soap tank to cause soap to flow to the nozzle. A low-flow metering valve (SS-SS2-VH) from Swagelok regulated the flow of soap to the nozzle.

The fluid supply unit setup, shown in Fig. 13, had the flow meters and valves mounted to sheet metal attached to a 6" diameter aluminum pipe. The pipe was made to fit behind the sheet metal to contain the soap container and tubing. The pipe had holes drilled in it to allow the tubing to go from inside the pipe to the valves on the back of the sheet metal, while still

concealing the plastic tubing. The vessel that holds the pressurized soap solution, shown in the far-right image in Fig. 13, was placed inside the 6” diameter aluminum pipe.

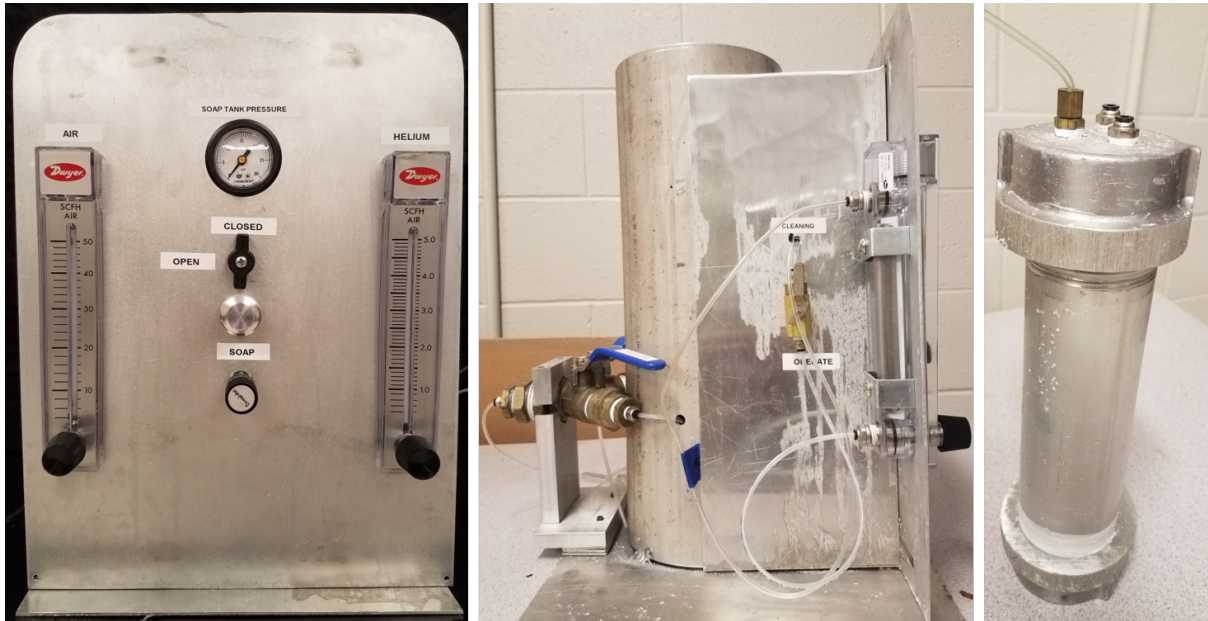


Figure 13: Fluid supply unit setup controls the flow rates of air, helium, and soap solution. The soap pressure vessel in the far-right image was placed inside the large aluminum pipe behind the flow meters and valves.

The Dwyer flow meters were factory calibrated for air at standard atmosphere (1 atm). The indicated flow rates on the flow meters were adjusted for the back pressure of the system by using equation 3.1. A 0.05-0.4 standard cubic feet per hour (SCFH) and a 0.5-5 SCFH flow meter that had 2” scales were used to measure the air and helium flow rate, respectively. The flow meters had an accuracy of 4% of full scale or ± 0.016 SCFH. The fluid supply unit design used 1/8” outer diameter (OD) plastic tubing and push-to-connect (PTC) fittings to transport air, helium, and soap solution to the nozzle.

$$Q_2 = Q_1 \sqrt{\frac{(P_g + P_s)T_s}{P_s T_a}} \quad (3.1)$$

Q_1 is the observed flow meter reading in SCFH, Q_2 is the standard flow after pressure correction in mL/h, P_g is the gauge pressure, P_s represents standard atmospheric pressure, T_a represents the room temperature at the time of testing, and T_s represents standard temperature. An air flow meter was used to regulate the flow of helium. Thus, it had to be calibrated since

the density of helium is less than air, by using equation 3.2. SG_{He} is the specific gravity of helium used in the flow meters.

$$Q_2 = Q_1 \sqrt{\frac{1}{SG_{He}}} \quad (3.2)$$

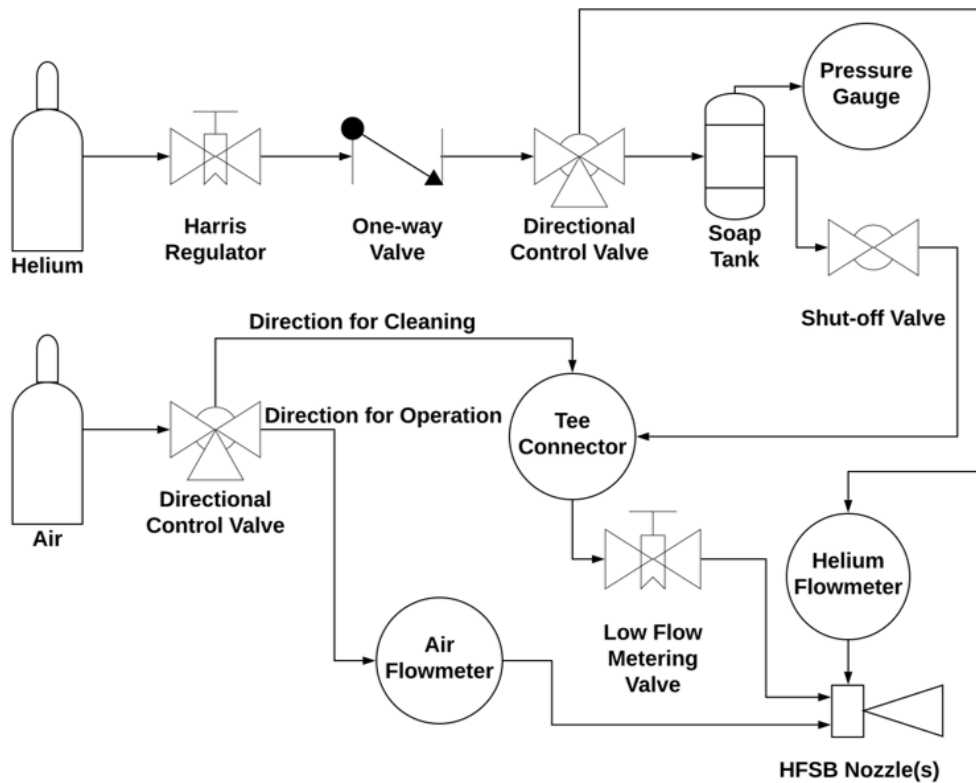


Figure 14: HFSB fluid supply unit schematic diagram showing the main components. All components are connected with 1/8" OD plastic tubing with push-to-connect fittings.

A schematic of the fluid supply setup which supplies the HFSB nozzles with air, helium, and soap is depicted in Fig. 14. A directional-control valve on the air line controls whether the air goes directly to the nozzle or to the soap line. Air was used to clean out soap in the soap valve and tube before storing the unit. This prevented soap from drying in the soap valve and in the nozzle, which would have caused a blockage. The directional control valve on the helium line was a dual shutoff control valve that could be opened and closed to allow helium to go to the nozzle and/or the soap tank.

The soap solution used to generate HFSBs was SAI 1035 Bubble Film Solution from Sage Action, specifically made for flow visualization experiments. The solution was a combination

of distilled water, glycerin, and a mild surfactant. The glycerin in the soap prolongs the lifespan of the bubbles to enable seeding large volumes for PIV. The soap solution was critical to produce a consistent supply of HFSSBs that are the correct diameter. If the incorrect ratios of soap and glycerin were used, it resulted in the nozzles not producing consistently and the HFSSBs not having a long enough lifespan to perform PIV experiments. The soap solution was held in an aluminum pressure vessel rated for 150 psig, which was higher than the operating pressure of 18 - 20 psig. The cap on the top of the pressurized container had 2 PTC fittings and a compression fitting, which is depicted in the far-right image in Fig. 13. One of the PTC fittings was used to connect the helium supplied to the soap container, whereas the other PTC was connected to a pressure gauge to monitor pressure in the container. The compression fitting allowed the soap tube to pass through the top of the soap container all the way to the bottom to allow the soap to exit and go to the nozzle.

Since the soap flow rate was critical to achieve neutrally buoyant and consistent HFSSBs, the Swagelok valve was tested to calculate the soap flow rate through the valve in mL/h. The soap solution was run through the valve at 20 psig at various increments on the Vernier valve to record the volume of soap flowing through it. The flow rate of soap solution was measured using graduated cylinders and was used to formulate an experimental volume flow rate graph. This experimental data was compared to the theoretical graphs that Swagelok provided, and it matched well. The valve follows a fourth-order polynomial well with an R^2 value of 0.992, as depicted in Fig. 15. The flow rate equation displayed in the figure was used to determine the volume of soap solution flowing to the nozzle based on the setting of the Swagelok valve. The Sage Action soap solution's density was calculated from the volume and mass of the soap solution and was determined to be 1.1333 g/mL. By using the fourth-order polynomial, the volume of soap passing through the valve could be determined, and the ratio of helium to soap (Q_{He}/Q_{soap}) being used by the nozzle could be recorded.

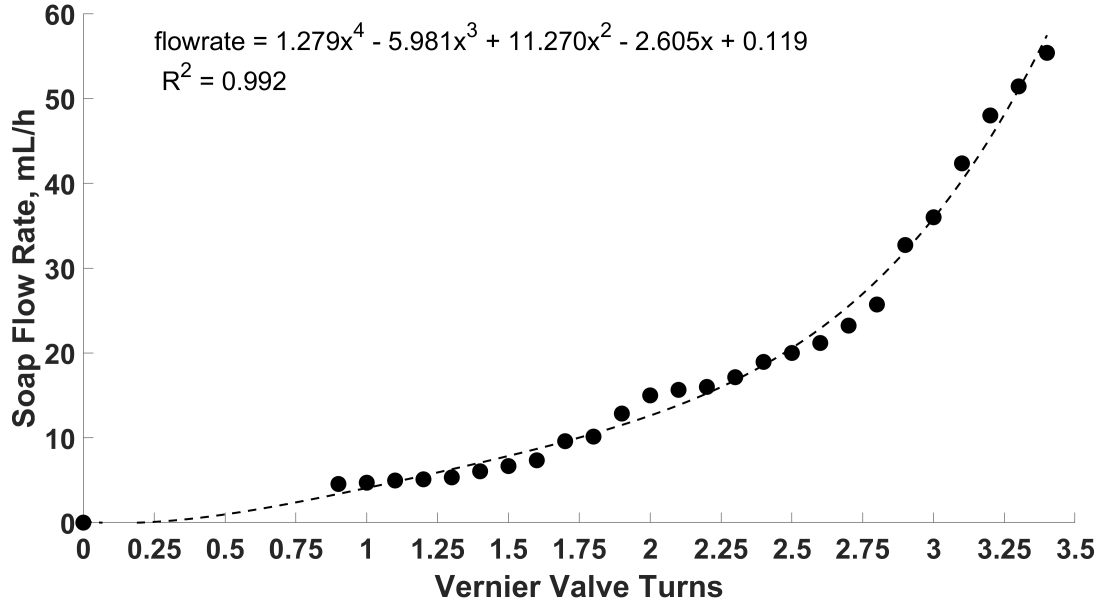


Figure 15: Soap valve calibration with Sage Action soap depicting the flow rate through the valve for different Vernier valve settings

According to Faleiros et al. [22], in their setup, $Q_{He}/Q_{soap} = 900 \pm 50$ was the best experimental ratio to achieve neutral buoyancy. To produce neutrally buoyant bubbles, they needed to have a density equivalent to that of air, which is 1.204 kg/m^3 at normal temperature and pressure (NTP). Helium has a density of 0.1664 g/L at NTP. Using equation 3.5 and the calculated Sage Action soap density of 1133.3 g/L , it was determined that the calculated theoretical ratio for neutral buoyancy occurs at $Q_{He}/Q_{soap} = 1092.2$. This ratio is assuming no helium or soap leakage when the bubbles are being formed, a consistent flow rate of helium and soap, and neglecting the soap film thickness. These factors cause the experimental and theoretical value of neutral buoyancy to be slightly different. The experimental value is slightly lower than the theoretical neutral buoyancy value due to soap leakage.

The volume of a bubble can be approximated by dividing the helium flow rate by the bubble production rate frequency. The bubble production frequency, f , is the number of bubbles exiting the HFSB nozzle per second.

$$V_b = \frac{Q_{He}}{f} \quad (3.3)$$

$$fV_b\rho_b = Q_{He}\rho_{He} + Q_{soap}\rho_{soap} \quad (3.4)$$

Substituting 3.3 into 3.4 yields:

$$\rho_b = \rho_{He} + \rho_{soap} \frac{Q_{soap}}{Q_{He}} \quad (3.5)$$

$$\frac{Q_{He}}{Q_{soap}} = \frac{1133.3g/L}{1.204kg/m^3 - 0.1664g/L} = 1092.2 \quad (3.6)$$

The pressure inside a soap bubble was approximated using the Young–Laplace equation, which states that the pressure inside an elastic container with a curved surface is inversely proportional to the radius as long as the surface tension is assumed to be constant. Using equation 3.7, a surface tension (γ) of 0.0275 N/m for a soap bubble [22], and an average bubble radius (r) of 0.0002 m, the pressure inside of an HFSB (P_b) was determined to be approximately 550 Pa.

$$P_b = \frac{4\gamma}{r} \quad (3.7)$$

$$P_b = \frac{4(0.0275N/m)}{0.0002m} = 550Pa \quad (3.8)$$

To produce a higher quantity of HFSBs, which is required for large field of view PIV, multiple nozzles can be operated simultaneously from the same fluid supply unit. Larger flow meters need to be used to operate more than one nozzle. Pipe tee fittings can be used at the exit of the air, helium, and soap lines to evenly divide the flow to each nozzle. To operate between two and approximately ten nozzles, a 0.5-5 SCFH flow meter and a 5-50 SCFH 5” Dwyer flow meter can be used. Each of the air, helium, and soap lines after the tee adapter to the nozzle had to be the exact same length so the pressure in each line was identical. If the lines were not the same length, there would be an uneven distribution of air, helium, or soap to the nozzles resulting in an uneven distribution of flow to the nozzles.

Using common off-the-shelf parts and 3D printing allowed the cost of the fluid supply unit and the printed nozzles to be less than a thousand dollars, whereas a commercial HFSB system is thousands of dollars. Once this HFSB system is set up, the only additional price is the cost

of 316L stainless steel powder to make additional nozzles. A parts list for the fluid supply unit used in this study is provided in Table 5 in the appendix.

3.4 Characterization of HFSB Diameter and Production Rate

Once the final integrated design of the nozzle was printed, a systematic approach was taken to test the range of flow rates to the nozzle. Flow rate parameters were independently varied to determine the influence they had on the HFSB diameter and production rate. The flow rate of air to the nozzle was varied from 43.5 to 217.5 L/h, helium was varied from 8.53 to 28.42 L/h, and soap was varied from 5.54 to 22.89 mL/h. The increments of these flow rates are listed in Table 1. The diameter of the HFSBs and the consistency of HFSB production was recorded for many air, helium, and soap flow rate combinations. These flow rate ranges were chosen based on the flow rates that operated best with the preliminary designs, and modified based on how the final nozzle design was performing. The flow rate ranges were focused around the flow rates where Q_{He}/Q_{soap} was between 901 and 1083. This range of helium to soap flow rate ratios was the approximate range to produce neutrally buoyant bubbles. These flow rates were close to the operating regimes that Faleiros et al. determined worked well with the nozzles from Netherlands Aerospace Centre and Delft University of Technology [22].

Table 1: Tested flow rate values of air, helium, and soap to the nozzle

Air (L/h)	Helium (L/h)	Soap (mL/h)
43.5	8.53	5.54
65.3	11.37	8.69
87.0	17.05	10.50
108.8	22.74	12.62
130.5	28.42	15.23
152.3		18.56
174.0		22.89
195.8		
217.5		

The diameter of HFSBs published in literature are normally between 0.2 and 0.6 mm in diameter to be neutrally buoyant, but there have been papers that reported neutrally buoyant bubbles up to approximately 4 mm in diameter [3, 5]. To demonstrate that using metal additive manufacturing to print HFSB nozzles is a viable option, the diameter of the bubbles,

the production rate, and the consistency of production between ten 3D printed nozzles was investigated.

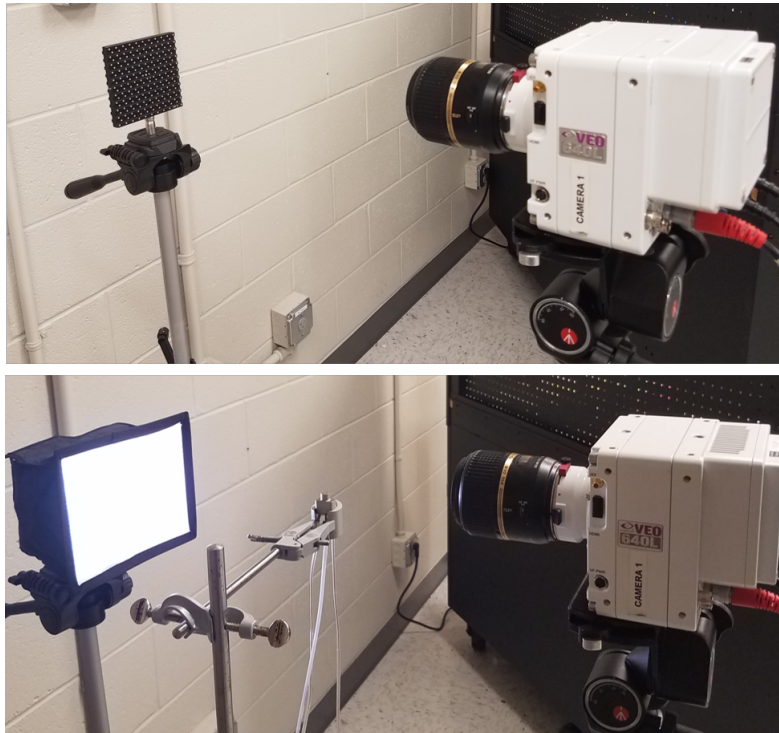


Figure 16: Setup of the 3D calibration plate used to calibrate the camera from the image space in pixels to the physical space in millimeters (top), and shadowgraph setup to record illuminated images of HFSBs (bottom)

A Phantom VEO 640L high-speed camera, which has a maximum frame rate of 1,400 fps at 2560×1600 , with a Tamron SP 60 mm f/2 Di II 1:1 macro lens was used to visualize the HFSBs. The high-speed camera was focused on a calibration board, depicted in the top image in Fig. 16. The calibration board was placed in the same plane where the HFSBs would be exiting the nozzle. This allowed the camera to be calibrated from the image space in pixels to the physical space in millimeters. Using a shadowgraph setup, the HFSBs were illuminated with a 15W, 1400 Lumen LED light with a diffuser. The light was placed behind the bubbles facing towards the camera, depicted in the bottom image of Fig. 16. The center of the nozzle had to be placed in the exact plane as the front of the calibration board to ensure the calibration from pixels to millimeters was correct and the bubble diameters being recorded were accurate. A small 50 mW laser with a 60-degree fan angle to split the laser beam into a sheet was used to verify that the nozzle was placed in the calibrated plane. The laser sheet was aligned with the

calibration board and then the calibration plate was removed and the HFSB nozzle was placed in the same plane.

Images were captured of the bubbles exiting the nozzle using the high-speed camera and the Phantom Camera Control (PCC) 3.4 software. The resolution of the high-speed camera was set to 68×256 in order to set a sample rate of 105,356 fps. The exposure time of the camera was set to $1.000 \mu s$. Within PCC, the gain, toe, and sensitivity settings were set to 1.000, and gamma was set to 0.750 with a sharpen filter applied. The edges of the HFSBs were clearly defined in the illuminated shadowgraph images, as shown in Fig. 17.

Using the edges of the bubbles, the number of pixels in diameter was counted using a MATLAB code that utilized the function “`imfindcircles`.” This MATLAB code, provided in the appendix in Fig. 50, used a circular Hough transform to identify the radius of the bubbles in

pixels. This code introduced a small amount of error in the bubble diameter, due to limitations in the code perfectly identifying the edge of the bubbles. The camera calibration that was performed at the focal plane where the bubbles exited the nozzle allowed the bubbles’ radii in pixels to be converted to millimeters.

A large concentration of HFSBs in the flow volume being analyzed is required for large-scale PIV. This requires the HFSB nozzles to produce a large quantity of bubbles every second. The HFSB production rate of each 3D printed nozzle was determined and then compared with other working nozzles published in literature. The MATLAB program that was used to determine the HFSB diameters was modified to include a bubble counter and a control volume that dynamically changed based off of the diameter of the bubbles in each data set to determine the production rate. Whenever a bubble passed through the control volume, the code would count the bubble. However, when the HFSBs velocity was high, the HFSBs would not always be completely within the control volume resulting in the counter not counting every bubble that passed through. Increasing the size of the control volume improved the accuracy of the program for data sets where the nozzle was producing at a fast production rate. However, the

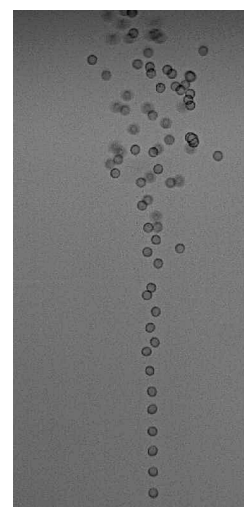


Figure 17: Shadowgraph image of HFSBs using the integrated nozzle and Sage Action soap solution

code would then allow multiple bubbles within the control volume at a time for data sets that contained slower production rates. This would result in bubbles passing through the control volume without being counted.

Instead of using this program, a fast Fourier transform (FFT) using MATLAB was performed on each neutrally buoyant data set of 10,000 recorded images. The code, provided in Fig. 51 in the appendix, prompts the user to select a point on one of the images in the data set to be used to determine the intensity of the bubbles. A point in the center of the bubble closest to the nozzle was selected for each data set. As the bubbles move past the point on subsequent recorded images, the intensity of the images change. The code also prompts the user to select a background point in the image to perform a background subtraction to remove image noise and improve the FFT results. The FFT program plots this intensity change for each recorded data set. The frame rate of the high-speed camera was set at 105,356 fps, which was more than twice the Nyquist frequency to avoid any aliasing. Using the capture speed of the camera and the dominate frequency that was found from the FFT plots, the overall production rate of each nozzle at the tested air, helium, and soap flow rates was determined. Using MATLAB, a Gaussian normal curve was fitted over the FFT data to approximate the mean and standard deviation of the production rate at each flow rate setting. Each of the FFT plots contained noise in the data. This noise was truncated to improve how well the normal curve fit the data.

A small source of error was introduced by using the MATLAB programs to determine the diameter and production rate of the bubbles. The code that determined bubble diameter would occasionally miss or count a bubble twice. This could have slightly altered the average bubble diameter and standard deviations. In the FFT production rate code, the noise from the FFT had to be truncated, which could have introduced a small amount of error in the production rate values. There was a small variation in production rates due to the point location that was selected in MATLAB to compare the image intensities. Since the FFT error occurred for every air, helium, and soap flow rate tested, this error should not have significantly changed any of the results presented in this study.

3.5 Computed Tomography Methods

One of the best non-destructive methods for characterizing the defects and internal features of AM parts is by using X-ray computed tomography (XCT) [46]. A XCT cabinet works by emitting x-rays from a source through a tube which is focused on the object being scanned. A detector collects the x-rays exiting the scanned object and records the attenuation values, which is then sent to a computer to reconstruct a 3D representation of the scanned object.

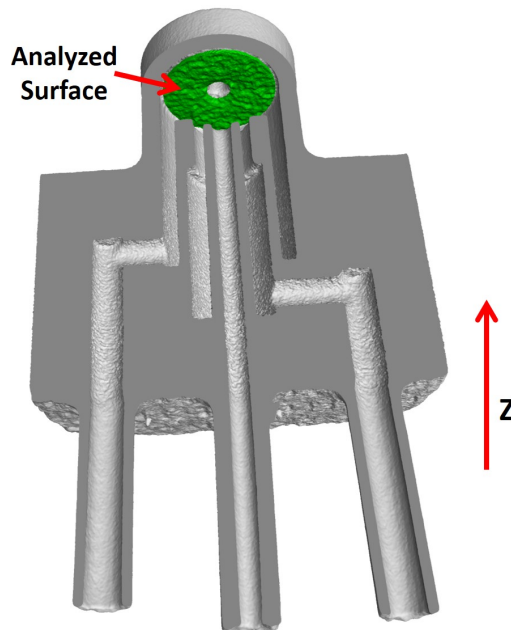


Figure 18: Location on HFSB nozzle where the surface roughness was analyzed from CT scans

The unsupported overhanging region of the nozzle's cap was the most critical aspect of the print, as shown in Fig. 18. This is the location where the HFSBs exit the nozzle and cap. In Laser-Powder Bed Fusion additive manufacturing, overhanging regions normally have a high surface roughness due to having lower thermal conductivity than the surrounding part [47, 48]. Therefore, X-ray CT was utilized to assess the surface roughness of this overhanging region of the nozzle's cap and its potential effect on the HFSB nozzle's performance. In addition, X-ray CT was used to confirm that the internal tubes within the nozzles were clear and had no obstructions. A Pinnacle X-ray Solutions 500/90 XLW XCT equipped with a Micro Focus X-ray Tube operated at 225 kV and 950 μA was used to evaluate the nozzles. The HFSB nozzles were each individually scanned in the XCT cabinet. Each nozzle was placed on a carbon rod

to hold it in position and was rotated on the rotation stage within the XCT cabinet while x-rays were being emitted to scan the entire nozzle. The reconstructed image depicting the scanned HFSB nozzle and how it is rotated within the XCT is shown in Fig. 19, and a picture of the XCT cabinet used in this study is displayed in Fig. 20.

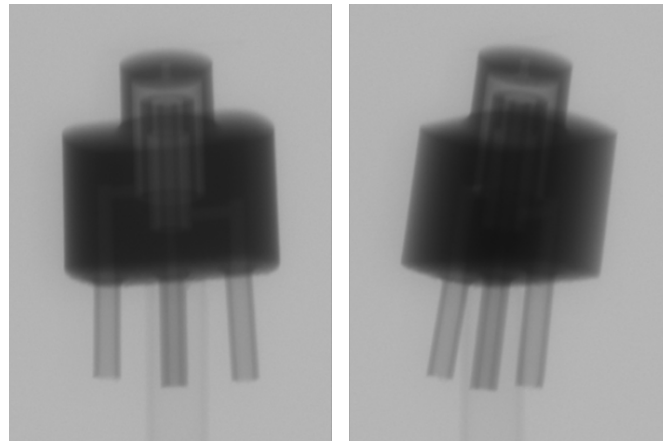


Figure 19: XCT scan of the HFSB nozzle showing how it is rotated while being scanned

The XCT captured a total of 1440 images with an integration time of 1150 ms for a complete 360-degree rotation. The data was then reconstructed and analyzed in Volume Graphics VGStudioMax 3.2. The analyzed surface was evaluated by applying the automatic surface determination and defining the region of interest, as described in [49]. The surface of the analyzed area was evaluated against a best-fit plane. The nominal-actual deviation was calculated using the deviation between the nominal and actual surface, which provided the surface roughness of the nozzles. The roughness deviation is a more qualitative measurement at this time, and was employed to provide a comparative analysis of the internal roughness of this overhanging region.

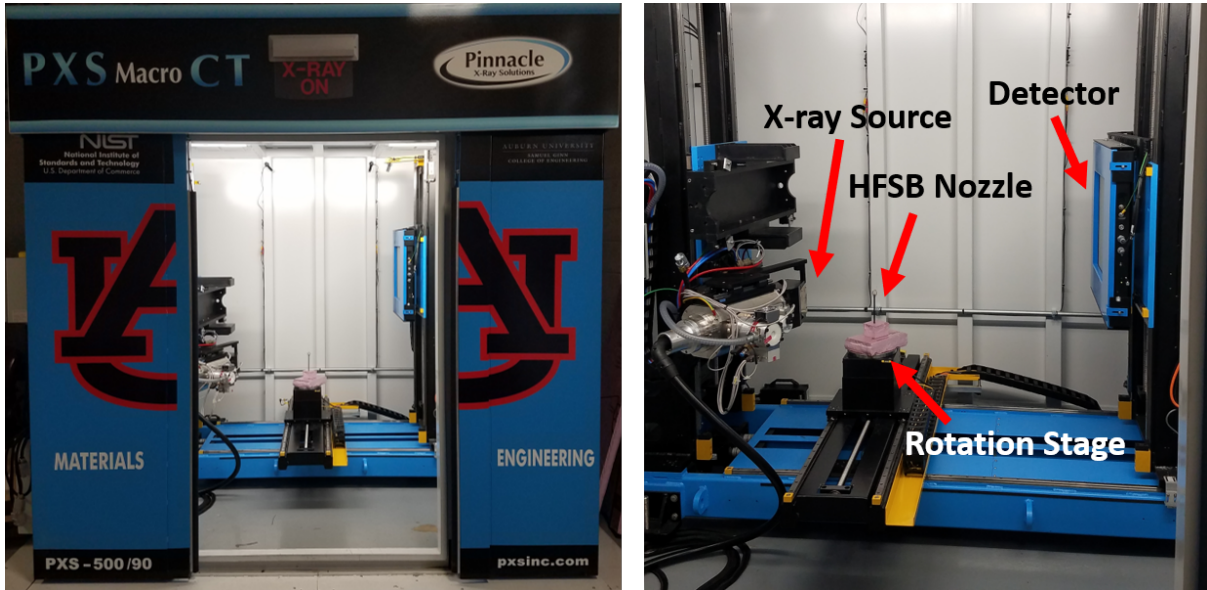


Figure 20: Pinnacle X-ray Solutions 500/90 XLW XCT cabinet used to evaluate HFSB nozzles

3.6 Statistical Methods

To determine if the bubble diameters being produced by all ten nozzles could be represented only by the nozzles' flow rates, a linear regression was performed using the statistical analysis software SAS 9.4. SAS is a statistical software that allows large data sets to be analyzed. The influence of the air, helium, and soap flow rates individually and collectively on the HFSB diameter for each nozzle was determined. The interaction effects between explanatory variables was also investigated. Interaction effects occur when the effect of one explanatory variable depends on the value of another variable in the model. Including interaction terms in the model can improve the accuracy of the model's fit to the data. Regression equations were formed using SAS to represent the HFSB diameter with respect to the flow rates. Although it was apparent that the air flow rate to the nozzle was most influential to the bubble diameter, a statistical linear regression was performed to analyze the influence that each flow rate had on the overall bubble diameter. Having an accurate regression equation that represents the bubble diameter, would allow the bubble diameter being produced by the nozzle to be approximated by only knowing the flow rates of air, helium, and soap to the nozzle.

Nozzle 1 was evaluated at the largest number of flow rate conditions, thus the linear regression model was created using the data from this nozzle. Two linear regression models were

formed using the recorded data from nozzle 1. The first linear regression model was based on all of the neutrally buoyant optimal flow rates. The second model contained both the neutrally buoyant and non-neutrally buoyant data. In theory, the neutrally buoyant cases would be the only data that would need to be analyzed in SAS since the objective is to always operate the HFSB nozzle within neutrally buoyant flow conditions. However, there was a small range of air, helium, and soap flow rates that produced neutrally buoyant bubbles, which resulted in the data set being a small range of flow conditions. This caused the linear regression to be based off less data points, resulting in a model that might not represent the bubble diameters accurately. To report a regression model that best represented the HFSB diameters produced from nozzle 1 with regard to flow rates, both of these models were evaluated.

Chapter 4

Results

4.1 Effect of operating parameters on nozzle performance

In addition to the design of the HFSB nozzle, the air, helium, and soap flow rates determine how the nozzle operates and what HFSB diameter and production rate is produced. To use HFSBs as a measurement technique in PIV, the nozzles need to be steadily producing consistent neutrally buoyant HFSBs. Without the nozzles producing constantly with the correct HFSB diameter, the seeding density of the particles will be too low or they will not follow the flow of air precisely for accurate PIV measurements.

4.1.1 Influence of Air Flow Rate

To understand how the HFSB nozzle operated with different flow conditions, each of the flow rates were varied independently to document how the diameter and production rate were affected. As observed in other publications, such as [10, 22], as the air flow rate to the nozzle was increased, the HFSB diameter decreased. The experimental results, depicted in Fig. 21, Fig. 22, and Fig. 23 confirm this observation for the majority of helium and soap flow rate tested. The HFSBs are smaller in diameter with higher air flow rates because the bubbles are pushed through the orifice nozzle faster and have less time to form before the bubbles separate, therefore reducing the amount of helium inside each bubble.

In Fig. 21, the HFSB diameter is shown for nozzle 1 at approximately neutrally buoyant He:Soap ratios. The diameter of the bubbles decreased as the flow rate of air increased. The standard deviation is smaller for a He:Soap ratio of 981, but there is no conclusive trend that the standard deviation follows when the air flow rate was between 108 L/h and 174 L/h for neutrally buoyant bubbles. Nozzle 1 was chosen to be plotted as it had the most flow conditions and He:Soap ratios tested. The other nine nozzles performed in a similar way as nozzle 1, with regard to diameter and production rate changes when air flow rate was varied.

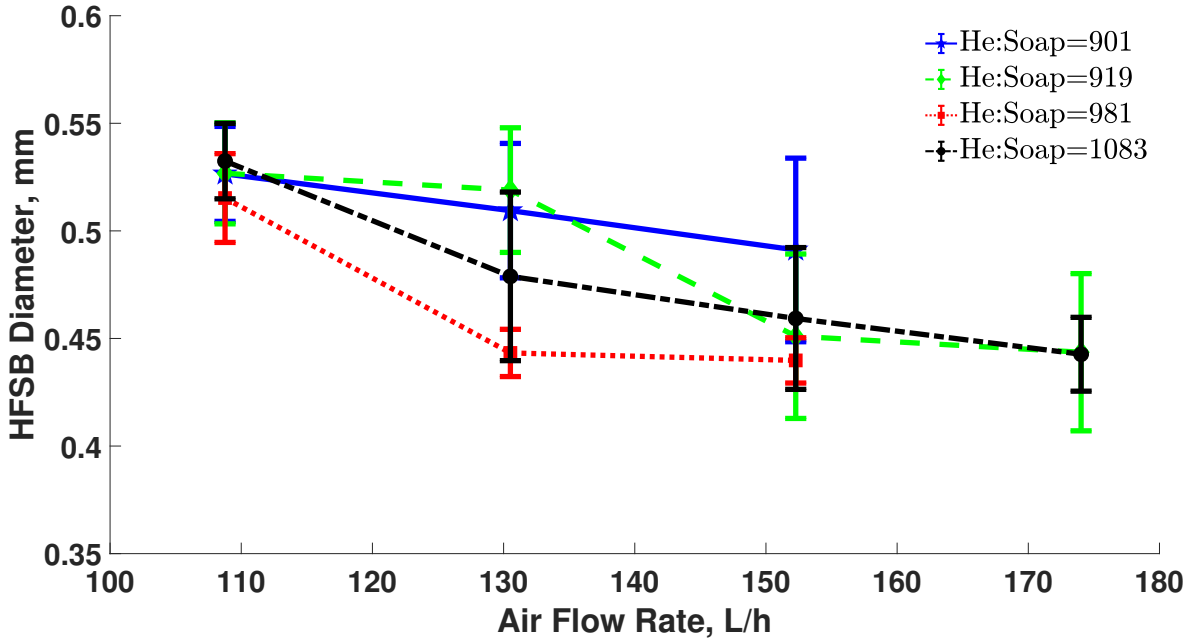


Figure 21: Average diameter and standard deviations of HFSBs (mm) for varying air flow rates (L/h). These bubble diameters were recorded for approximately neutrally buoyant flow conditions at optimal air flow rates for nozzle 1.

According to Morias et al., the nozzle can operate in two regimes, either “bubbling” or “jetting” [35]. Jetting is characterized by the soap extending past the nozzle and the bubbles do not separate until farther away from the nozzle. This can result in the bubbles being irregular and inconsistent in size and buoyancy. Normally, high air or helium flow rates caused jetting in the nozzles, which agreed with what Gibeau et al. reported [10]. In the bubbling regime, bubbles are separated immediately after exiting the nozzle and are more consistent in size and neutral buoyancy. The HFSB system needs to be operated within the bubbling regime as less variation in bubble diameters will result in more accurate PIV data. Examples of the bubbling and jetting regimes in the nozzles can be observed in Fig. 22.

Figure 22 is shaded to represent the different operating production regimes. The shaded regions are used to visualize which regime the majority of bubbles are being produced within for the corresponding air flow rate, and does not represent which regime all bubbles were produced within for a specific air flow rate. For example, higher helium flow rates can cause the nozzle to begin jetting before an air flow rate of 174 L/h. For the metal 3D printed nozzles, the air flow rate had to be between 108 and 174 L/h for optimal neutral buoyant HFSBs. This bubbling regime is depicted in the green (a) shaded region in Fig. 22. In the purple (b) region,

the nozzle was producing in the bubbling regime with a low air flow rate. This resulted in large diameter bubbles and occasionally soap mist. Soap mist exiting the nozzle with the bubbles occurred when the soap flow rate was too high for the amount of air supplied to the nozzle. In the red (c) region, the nozzle just transitioned into the jetting regime and the air flow rate was slightly high, which caused the bubbles to be irregular in shape. Lastly, in the red (d) region the air flow rate was very high which resulted in the nozzle producing in the jetting regime. This was evident because the soap extended out from the nozzle and the bubbles did not separate immediately after exiting.

Even though a lot of the data in Fig. 22 occurs at less than optimal flow conditions, it shows how at the majority of flow conditions the overall bubble diameter trend decreased as the air flow to the nozzle increased. This trend was affected by the He:Soap ratio, but the air flow rate was the primary parameter that determined the bubble diameter. Additional sample images of the HFBSBs being produced at different air and He:Soap ratios is provided in Table 4 in the appendix.

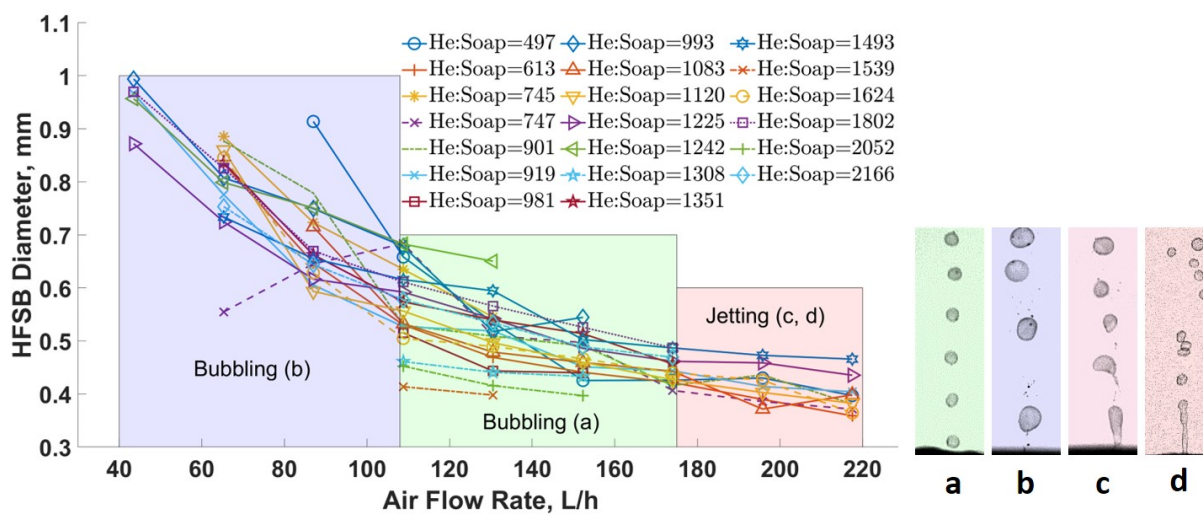


Figure 22: Diameter of HFBSBs (mm) for varying air flow rates (L/h) for all flow conditions for nozzle 1. The shaded regions depict the different flow regimes corresponding to the HFBSB images at the right side. The optimal air flow rate for the 3D printed nozzles is depicted in the center green shaded region which had the best and most consistent bubble diameter and production rate. (a) Bubbling regime with optimal air flow rate, (b) bubbling regime with a low air flow rate, (c) transitioning to jetting regime, (d) jetting regime with a high air flow rate.

When the nozzle was operated in the jetting regime (normally above 174 L/h) or in the low air flow bubbling regime (normally below 108 L/h), the standard deviations for the bubble

diameters were larger than when the nozzle was operating at optimal conditions. This can be observed in Fig. 23, which depicts the standard deviations for the bubble diameters for nozzle 1 operating in the range of He:Soap ratios of 901 to 1083.

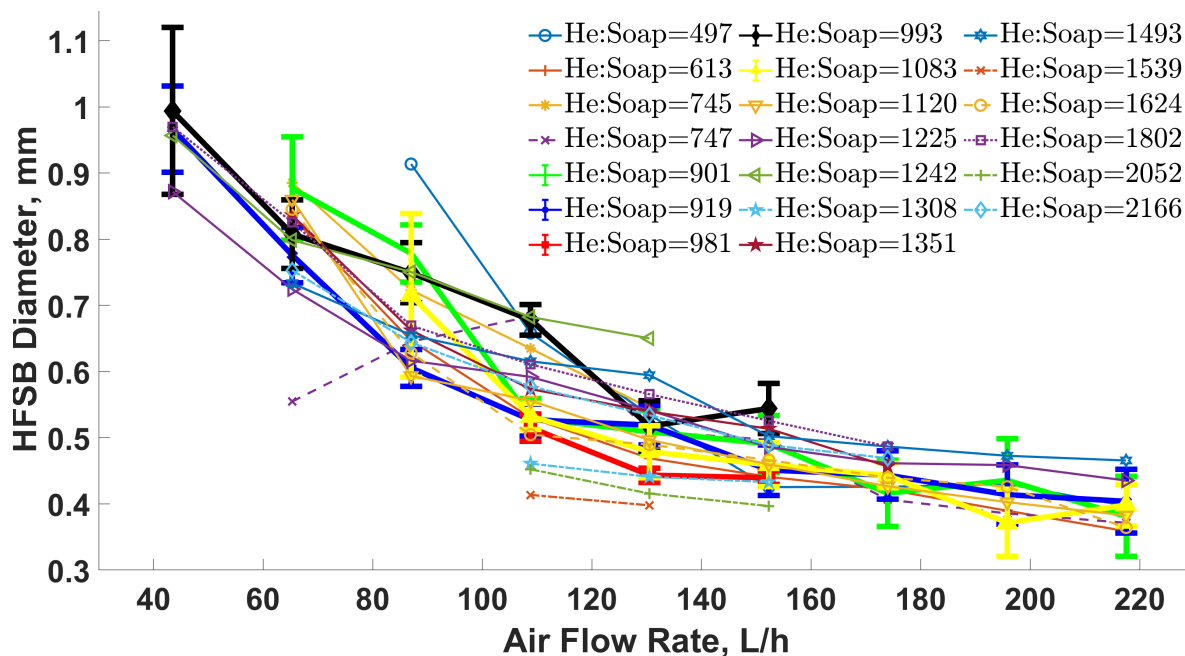


Figure 23: Diameter of HFSBs (mm) for varying air flow rates (L/h) for all flow conditions for nozzle 1. Each plotted line represents a different He:Soap ratio. The range of He:Soap ratios from 901 to 1083 have standard deviations shown.

In Fig. 24, the HFSB production rate is shown for an average of the ten tested nozzles at approximately neutrally buoyant He:Soap ratios of 901, 981, and 1083. At these He:Soap conditions, the production rate always increased as the air flow rate to the nozzle increased. As long as there is a sufficient soap supply to the nozzle, the increase in production rate trend should continue until the air flow rate or helium flow rate is high enough to cause the nozzle to begin jetting. The nozzles began to transition into the jetting regime when the air flow rate was higher than 174 L/h at neutrally buoyant He:Soap ratios; however, a few cases transitioned as early as 152 L/h. The highest production rate where the HFSB nozzle performed consistently occurred at an air flow rate of 152.27 L/h. These findings are consistent with other research papers [10, 22].

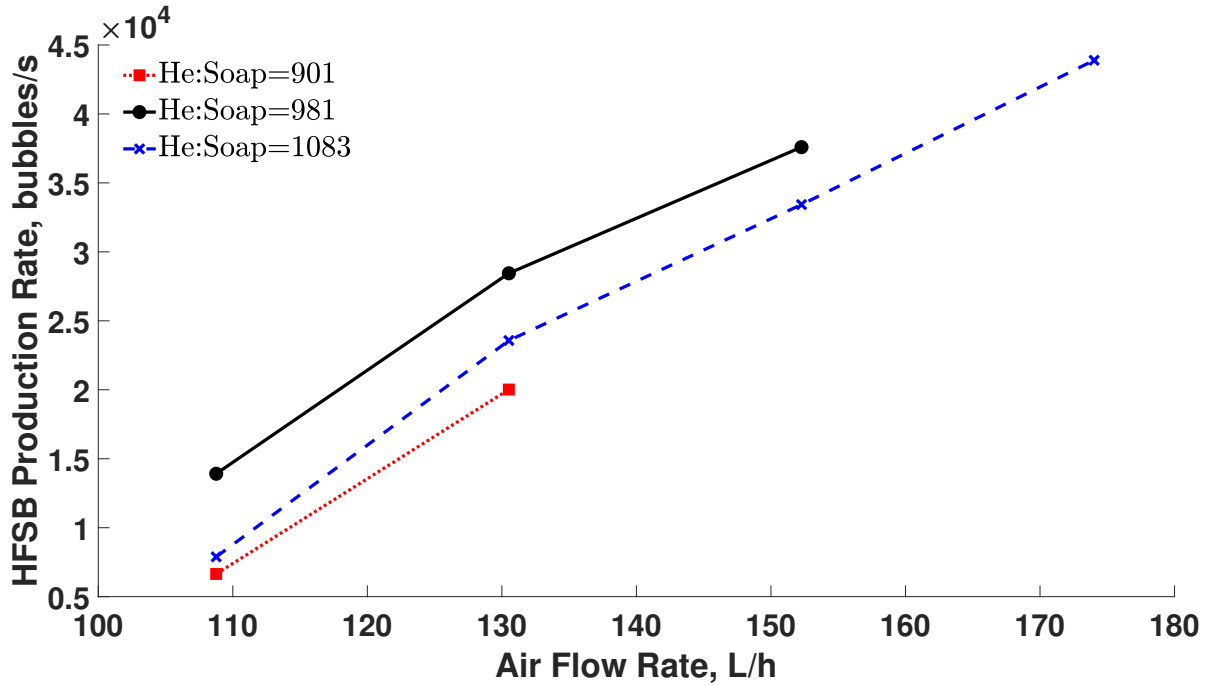


Figure 24: Production rate of HFSBs (bubbles/s) for varying air flow rates (L/h) averaged for ten metal 3D printed nozzles at neutrally buoyant He:Soap flow conditions

4.1.2 Influence of Helium Flow Rate

The HFSB diameter at three different soap flow rates was plotted as the helium flow rate varied in Fig. 25. While increasing the air flow rate resulted in smaller HFSBs, an increase in the helium flow rate resulted in a larger HFSB diameter trend when air was held constant in the majority of the cases. This holds true as long as the nozzle was not operating with a low air flow rate. When the air flow rate was too low, at or below 87 L/h, the nozzle operated within the bubbling (b) regime for all of the soap flow rates plotted in Fig. 25. The nozzle was also operating within this non-optimal bubbling (b) regime at an air flow rate of 108.8 L/h when the soap flow rate was 15.23 mL/h. When the air flow rate was too low for the amount of soap being supplied to the nozzle, an increase in helium caused the bubble diameter to temporarily decrease and go against the general trend.

It was observed in each of the plots that when the air flow rate was between 108 and 195 L/h, the HFSB diameter had a positive trend as the helium flow rate increased from 11.37 L/h to 22.74 L/h. The exception to this observation was at an air flow rate of 108 L/h and a soap flow rate of 15.23 mL/h. As the soap flow rate increased, the amount of air to the nozzle also

had to increase to keep the nozzle producing in the optimal bubbling regime. The air flow rate for optimal HFSB production occurred between 108 - 174 L/h and 130.5 - 174 L/h when the soap flow rate was between 10.50 - 12.62 mL/h and at 15.23 mL/h, respectively. Air flow rates below 108 L/h were normally not neutrally buoyant and resulted in large bubbles. Air flow rates above 174 L/h usually resulted in the nozzle operating within the jetting regime. If the helium flow rate was high enough to cause the bubbles to be buoyant, the nozzle would transition to jetting at lower air flow rates.

The helium flow rate does not largely influence the bubble diameter or production rate unlike air flow rate, but is a contributing factor to the diameter of the bubbles. Additionally, the helium flow rate is important because it affects the buoyancy of the bubbles being produced. The helium flow rate has to be closely monitored so the HFSBs remain neutrally buoyant.

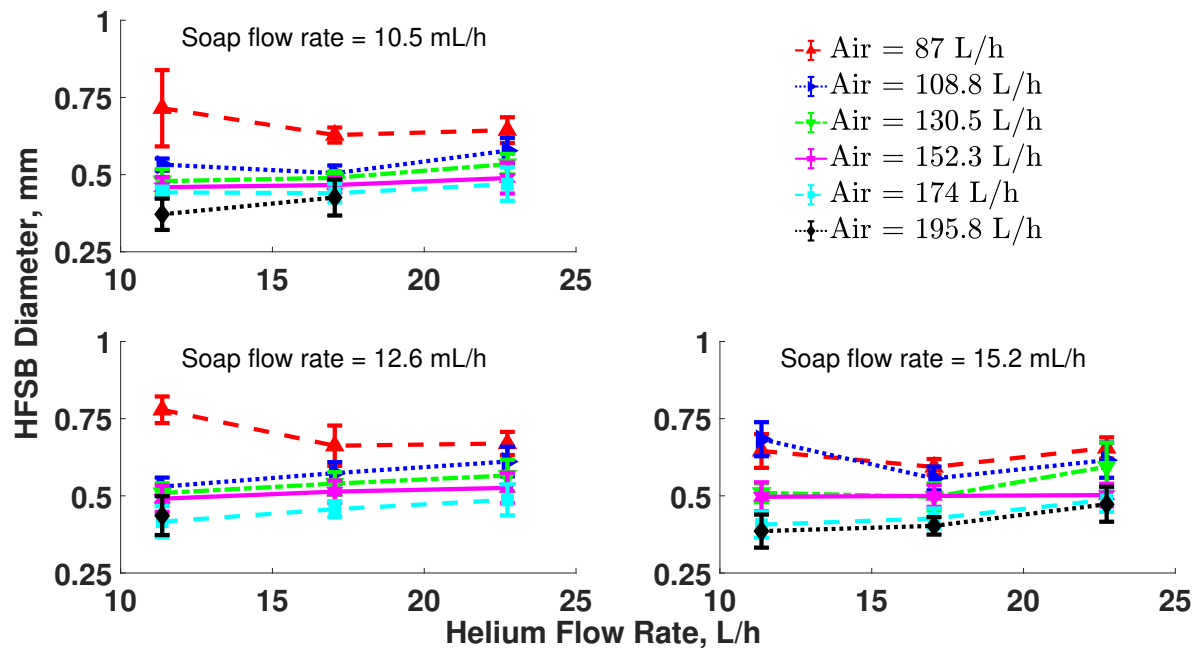


Figure 25: Diameter of HFSBs (mm) for varying helium flow rates (L/h) while the soap flow rate was held constant at 10.50 mL/h, 12.62 mL/h, and 15.23 mL/h

4.1.3 Influence of Soap Flow Rate

The HFSB diameter at three different helium flow rates was plotted as the soap flow rate varied. As observed in Fig. 26, there was no conclusive overall bubble diameter trend as the soap flow rate increased. There are more instances where the HFSB diameter tends to increase as

soap flow rate increases, but does not happen consistently for every soap or air flow rate. The soap flow rate tends to not have a large effect on bubble diameter or production rate when all flow conditions are considered. However, the soap flow rate is very important as it affects the production consistency of the bubbles being produced. When the soap flow rate was set too low, the nozzle would sputter and not produce a steady production of HFSBs. When the soap flow rate was too high, soap accumulated around the nozzle which caused no bubble production. When the air flow rate to the nozzle was increased, the production rate increased, thus the soap flow rate to the nozzle had to be increased to keep the nozzle operating consistently.

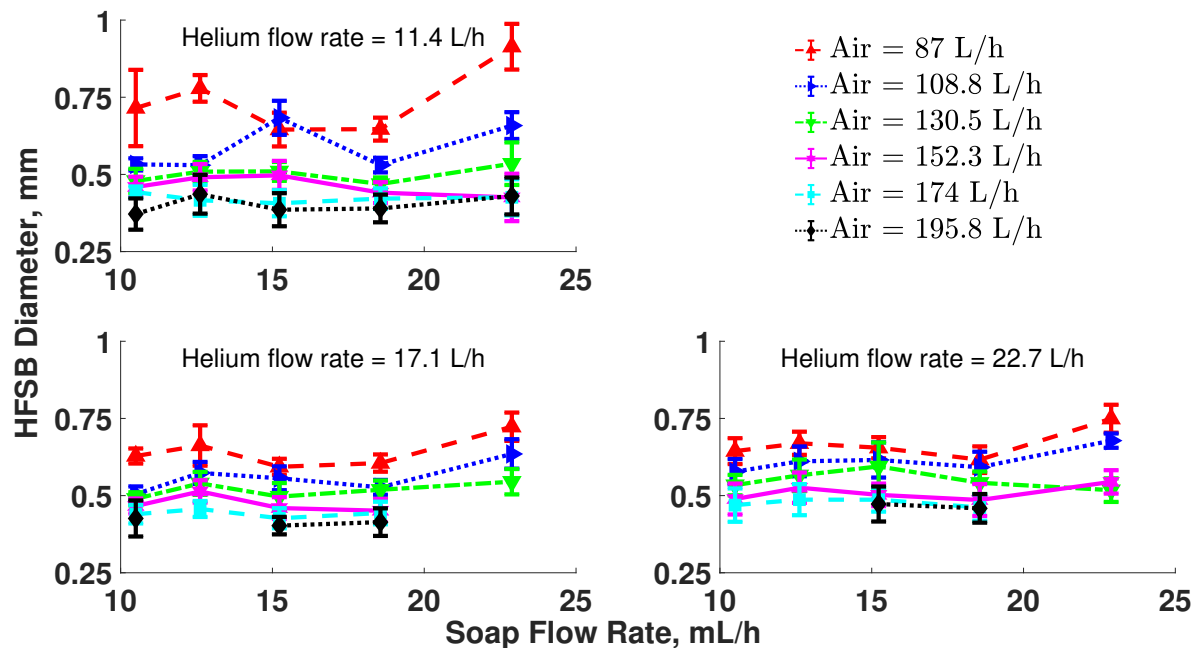


Figure 26: Diameter of HFSBs (mm) for varying soap flow rates (mL/h) while the helium flow rate was held constant at 11.37 L/h, 17.05 L/h, and 22.74 L/h

The helium to soap ratio is also important for controlling the buoyancy of the bubbles, which is critical for use in PIV experiments. The helium to soap ratio, Q_{He}/Q_{soap} , needs to be approximately between 850 and 1092 in order for the bubbles to be neutrally buoyant, depending on the amount of soap leakage around the nozzle. The majority of experiments with the 3D printed nozzles were conducted at either a He:Soap ratio of 981 or 1083. These two He:Soap ratios were chosen as they were close to the calculated neutral buoyancy value, but a little lower to account for soap leakage. This resulted in the real neutral buoyancy value being

slightly less than the theoretical value. These values also resulted in the least amount of bubble diameter variation, and the best production rate consistency from the He:Soap ratios that were tested with the nozzles.

4.1.4 Linear regression model for HFSB diameter

Faleiros et al. determined that the bubble diameter scales proportionally to the ratio of helium to air flow rates within the bubbling regime. For the NLR nozzle, equation 4.1 was found to represent the bubble diameter (d_b) using the nozzle's orifice diameter (d_0), the helium flow rate (Q_{He}), and the air flow rate (Q_{air}) to the nozzle [22]. The bubble diameters produced by the experiments, presented in this thesis, at neutrally buoyant flow rates followed equation 4.1 well until $(d_0 Q_{HE}/Q_{Air})^{1/3} = 0.5$, which can be observed in Fig. 27. This agrees with Faleiros et al.'s paper, as they found that there was a lot larger diameter variation when the ratio was above 0.5, especially for the DLR nozzles with larger orifice diameters. The bubble diameters that are larger and do not follow equation 4.1 well are generally caused by a low air flow rate. The trend line for the metal 3D printed nozzle is thus skewed slightly high due to these large bubble diameters.

$$d_b \sim \left(\frac{d_0 Q_{He}}{Q_{air}} \right)^{1/3} \quad (4.1)$$

A linear regression was performed on all data to further analyze the trend between bubble diameter and flow rates to the 3D printed nozzles. The first goal was to formulate a more precise equation than equation 4.1 that represented the metal 3D printed nozzles. The second objective was to determine the influence that each flow rate had on the bubble diameter. The non-neutrally buoyant cases were evaluated as the bubble diameter trend does not depend on neutral buoyancy of the bubbles as long as the nozzle is not jetting. The bubble diameter is mostly dependent on the flow rates of air, helium, and soap to the nozzle. After inspection of the air residual plots, a natural logarithm transformation on the air flow rate was performed to achieve a normal distribution in the residual plots and to remove the slightly skewed log-normal distribution. This increased the R^2 value for both the neutrally buoyant and non-neutrally

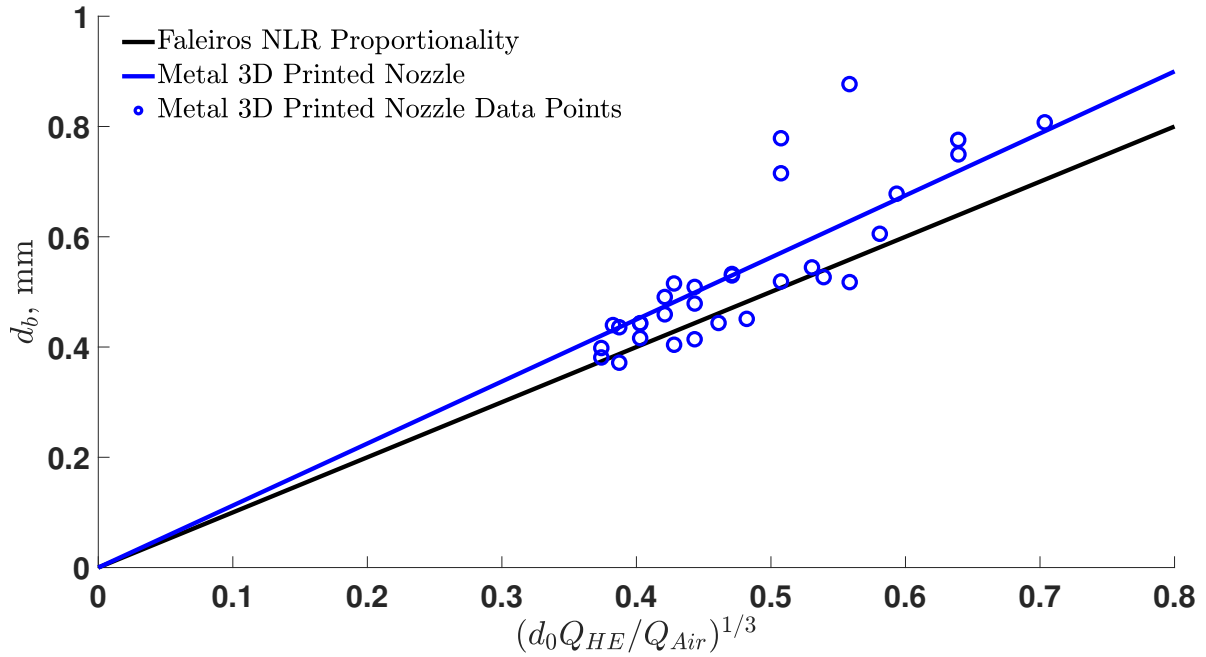


Figure 27: HFSB diameter is linearly proportional to the ratio of helium to air flow rates. The bubble diameter data for the metal HFSB nozzle was compared to the proportionality equation published in Faleiros et al.'s paper.

buoyant data. The air flow rate has the largest influence on the bubble diameter compared to the helium or soap flow rate, as depicted in Fig. 40 and Fig. 45 in the appendix.

For the neutrally buoyant cases, a linear regression model with air, helium, and soap flow rates as explanatory variables had an R^2 of 0.4868. Interaction terms between explanatory variables were investigated and were found to improve the model significantly to justify including them into the model. All terms in the model, including interaction terms, are significant with a p-value of less than 0.0001, excluding helium which had a p-value of 0.0021. With the addition of a logarithmic transformation on the air flow rate term and interaction terms, the linear regression model accounted for 56.14% of the data, as depicted in Fig. 41. Even though the R^2 value for this model is low, the neutrally buoyant data has little bubble diameter variation. Using this model, the root mean square error was 0.03122 mm for the neutral buoyant data. The resulting model that represents the bubble diameter for the neutrally buoyant cases is depicted in equation 4.2.

$$\begin{aligned}
Diameter \approx & 2.240 - 2.650 \times 10^{-1} \times \text{Log}(Q_{Air}) - 4.680 \times 10^{-3} \times Q_{Air} - \\
& 8.940 \times 10^{-3} \times Q_{He} - 8.863 \times 10^{-2} \times Q_{Soap} + \\
& 1.412 \times 10^{-4} \times (Q_{Air} \times Q_{He}) + 7.522 \times 10^{-4} \times (Q_{Air} \times Q_{Soap}) + \\
& 4.070 \times 10^{-3} \times (Q_{He} \times Q_{Soap}) - 3.498 \times 10^{-5} \times (Q_{Air} \times Q_{He} \times Q_{Soap})
\end{aligned} \tag{4.2}$$

Performing a linear regression on all data at once, both neutrally buoyant and non-neutrally buoyant cases, resulted in an R^2 value of 0.6094. This only contained air, helium, and soap in the model. A logarithmic transformation on the air flow rate term was performed on this regression model and the interaction terms between flow rates were included to improve the model to have an R^2 of 0.7216, as depicted in Fig. 46. Equation 4.3 is a good representation of how the air, helium, and soap flow rates influence the bubble diameter since it represents over 72% of the data, which includes both optimal and non-optimal data. Using equation 4.3 and the flow rates to the nozzle, the approximate bubble diameter can be estimated. The use of digital flow meters to ensure consistent flow rates to the nozzle and recording the bubble diameters at a larger range of air, helium, and soap flow rates likely would have improved how well the model represented the data. The results of the linear regression analysis can be found in Appendix E.

$$\begin{aligned}
Diameter \approx & 2.185 - 5.319 \times 10^{-1} \times \text{Log}(Q_{Air}) + 4.940 \times 10^{-3} \times Q_{Air} + \\
& 1.826 \times 10^{-2} \times Q_{He} + 4.731 \times 10^{-2} \times Q_{Soap} - \\
& 5.031 \times 10^{-5} \times (Q_{Air} \times Q_{He}) - 2.213 \times 10^{-4} \times (Q_{Air} \times Q_{Soap}) - \\
& 1.430 \times 10^{-3} \times (Q_{He} \times Q_{Soap}) + 5.130 \times 10^{-6} \times (Q_{Air} \times Q_{He} \times Q_{Soap})
\end{aligned} \tag{4.3}$$

4.2 Performance consistency of 3D printed nozzles

The following results section discusses the various nozzle performance parameters that were used to validate that additive manufacturing is a viable option to print HFSB nozzles. The

performance consistency between nozzles, the nozzles' internal surface roughness, and the nozzles' performance parameters compared to existing HFSB nozzle designs were investigated.

4.2.1 Consistency of nozzle performance parameters across 3D printed nozzles

The diameter of the HFSBs was fairly consistent across all ten 3D printed nozzles, which can be observed in Fig. 28. The range of the mean bubble diameter among the ten 3D printed nozzles was between 0.376 and 0.460 mm for a He:Soap ratio of 981, and between 0.388 and 0.505 mm for a He:Soap ratio of 1083, as depicted in Fig. 28. The average bubble diameter was 0.419 and 0.452 mm for a He:Soap of 981 and 1083, respectively. The standard deviation of each of the ten nozzles was between 0.0091 and 0.0452 mm, with the average standard deviation of the ten 3D printed nozzles with a He:Soap ratio of 981 being 0.0329 mm and 0.0524 mm for a He:Soap ratio of 1083. The He:Soap ratio of 981 had a smaller mean diameter, range, and standard deviation than the He:Soap ratio of 1083 at an air flow rate of 152.27 L/h.

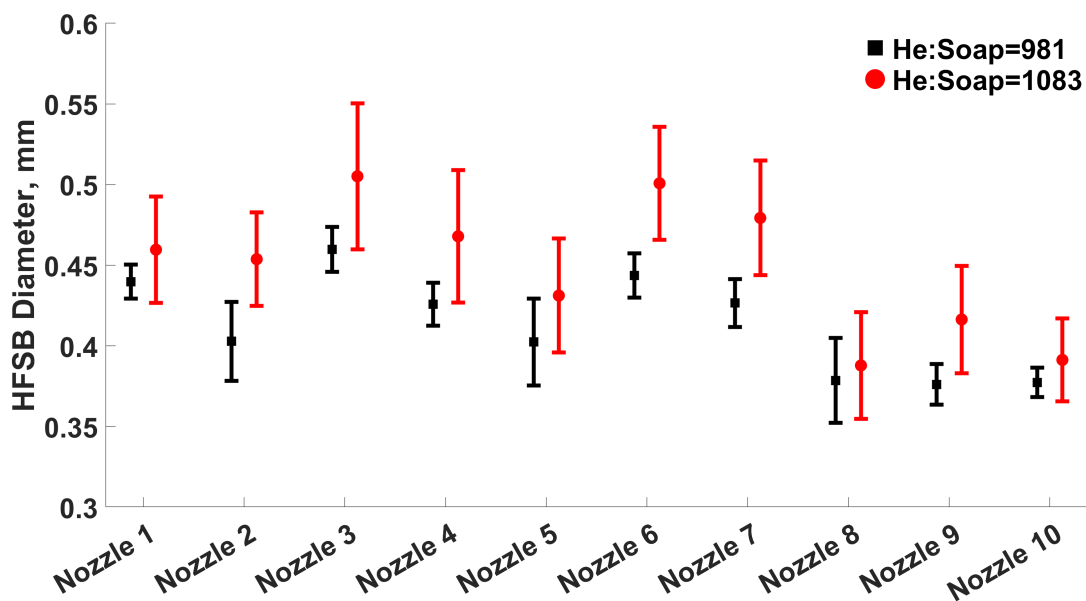


Figure 28: HFSB diameter and standard deviation for each metal 3D printed nozzle for He:Soap = 981 and 1083 at an air flow rate of 152.27 L/h

It was observed in all ten nozzles that smaller bubbles were produced at lower He:Soap ratios, and the bubbles were larger at higher He:Soap ratios. None of the HFSB nozzles produced

a bimodal distribution of bubble diameters at neutral buoyant flow rates. Bimodal distributions of bubble sizes normally occur in undesirable production regimes such as polydisperse bubbling and jetting regimes, which is discussed more in Gibeau et al.'s paper [10].

Many of the FFT plots had multiple production rate peaks, as depicted in Fig. 29 and Fig. 38, where it appeared that multiple production rates were being produced by the nozzle at one flow rate. One reason for this occurring was occasionally a nozzle would stop producing for a couple of milliseconds which resulted in lower frequencies on the FFT plots. Due to this, only the production rate frequency that occurred the most often on the FFT plots was used to determine the production rate and standard deviation. The rest of the data was truncated, and the Gaussian normal curve was only fitted to the data when the nozzle was producing and not pulsing on and off. The production rates obtained using the truncated FFT plots were verified by manually counting the bubbles being produced for a small sample of data within each data set.

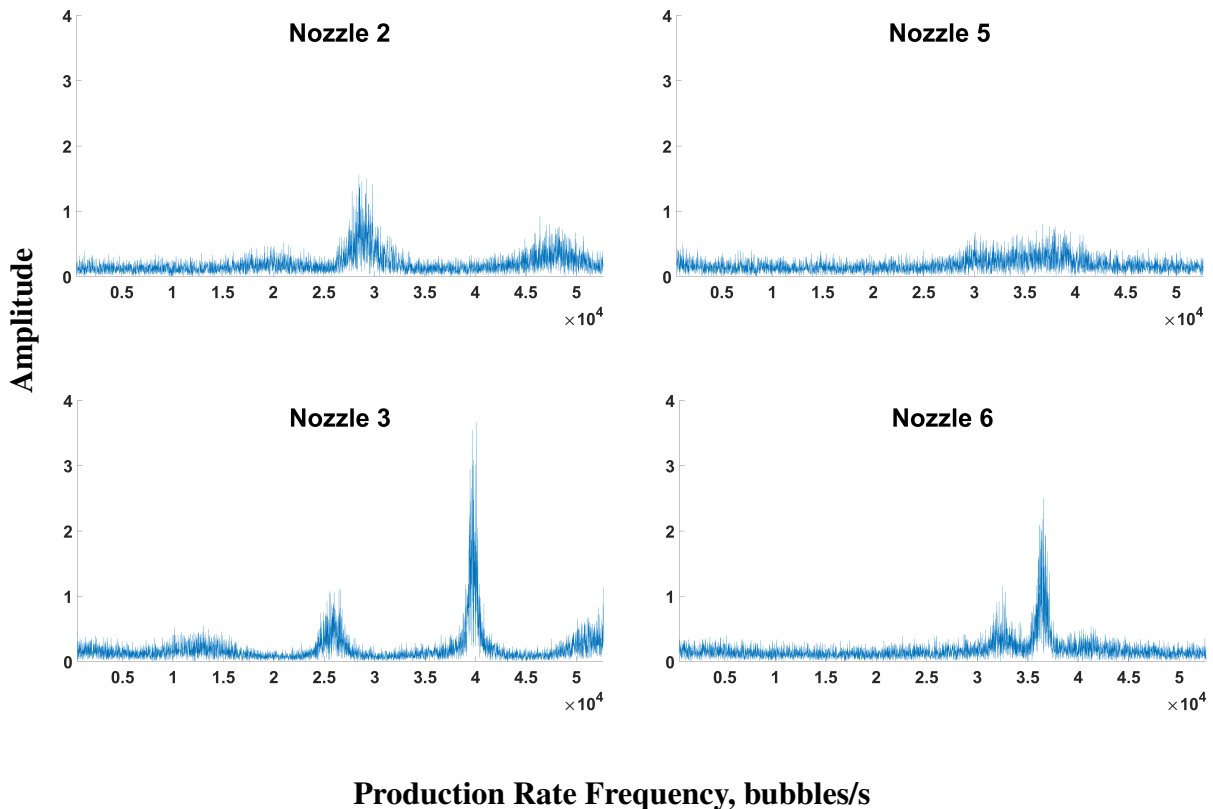


Figure 29: FFT production rate plots of two HFSB nozzles that had the worst internal surface roughness (top) and two nozzles that had the best surface roughness (bottom)

The production rate of the bubbles varied more than the bubble diameters between the nozzles. The average production rate ranged from 26510 to 43850 bubbles/s with an average of 37594 bubbles/s and 33428 bubbles/s for a He:Soap of 981 and 1083, respectively. This range was based on neutral buoyant flow conditions to the nozzles. The range is large due to some nozzles not producing consistently, which resulted in a lower production rate. Nozzles 5 and 8 had the largest deviation, while nozzle 2 had the lowest average production rate for both a He:Soap ratio of 981 and 1083, as depicted in Fig. 30.

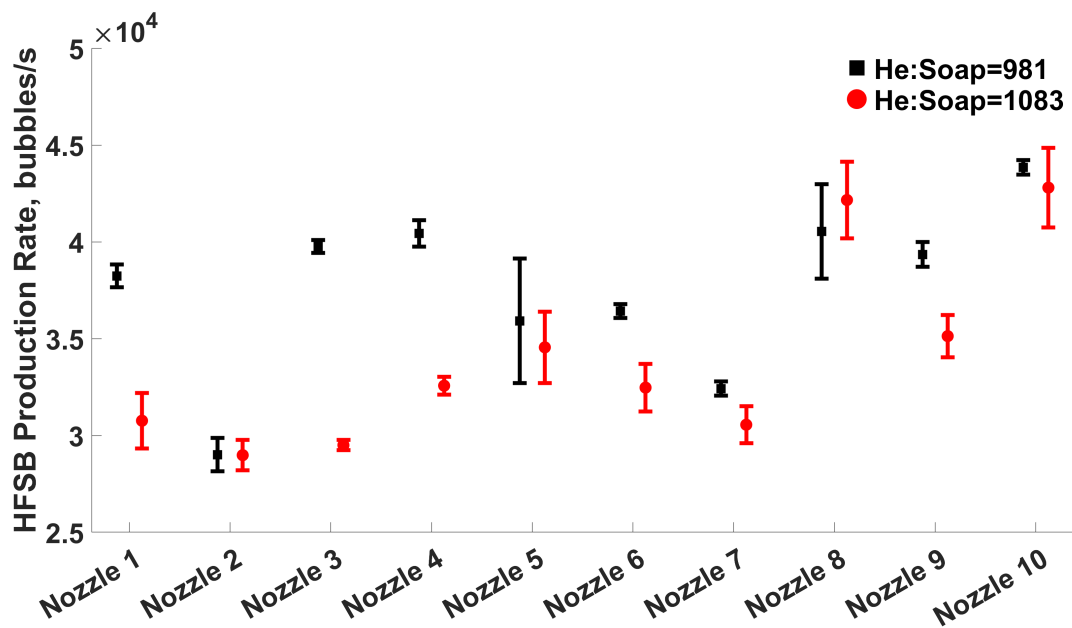


Figure 30: HFSB production rate and standard deviation for each metal 3D printed nozzle for He:Soap = 981 and 1083 at an air flow rate of 152.27 L/h

The production rate's standard deviation ranged from 267 to 3211 bubbles/s for the ten tested nozzles. The production rate's average standard deviation between the nozzles for a He:Soap ratio of 981 was 1017 bubbles/s and 1210 bubbles/s for a He:Soap ratio of 1083, which can be observed in Table 3 and Fig. 30. The average production rate and standard deviation was very similar for both the 981 and 1083 He:Soap ratios with the He:Soap ratio of 981 having a slightly higher average production rate and slightly lower standard deviation at an air flow rate of 152.27 L/h.

This deviation in production rate was most likely due to variations of the surface roughness of the inside of the 3D printed nozzle where the bubble exit, and the flow rates of air, helium,

and soap to the nozzle. The 3D printed nozzles were very close to being the exact same physical dimensions on the outside of the nozzle, but any type of variation within the nozzle could affect the productivity and consistency of the nozzle. The small internal tubes inside the nozzle and the unsupported overhanging region under the cap inside the nozzle needed to be investigated to ensure no large variations between printed nozzles existed.

After further inspection of the FFT plots, depicted in Fig. 29 and Fig. 38, some of the HFSB nozzles had FFT plots with less noise and production rate variation. This indicated less HFSB production frequency variation and more consistent production rates. To determine what caused some of the nozzles to perform better in terms of production rate and consistency, the CT scans of the ten nozzles were investigated to see if any of the inconsistencies with the surface roughness from 3D printing corresponded to a worse performing nozzle.

4.2.2 Relationship between internal surface roughness and nozzle performance

To determine if the internal surface roughness of the nozzle at the point of where the bubbles exit had any effect on how the nozzle performed, the surface roughness of each nozzle was compared to each nozzle's production rate and bubble diameter it produced. Using the data obtained from the CT-scans, Fig. 31 depicts the accumulated area at a deviation from the nominal surface of the internal surface of the HFSB nozzle cap. Here, the surface roughness was defined to be equivalent to the distance from the normal plane, where a percentage of the surface was included. The normalized surface roughness in relation to its deviation was plotted for each nozzle in Fig. 31, and the 90th, 95th, and 98th percentiles are summarized in Table 2.

Nozzles 1, 3, 4, 6, 7, and 8 had the lowest surface roughness in a range from 69 μm to 84 μm . A representative CT reconstruction of these surfaces can be found in Fig. 32 (left) and in Fig. 39 in the appendix. Whereas, the surface roughness of nozzles 2, 5, and 9 was considerably higher at 190 μm , 161 μm , and 126 μm , respectively. This can be visualized in Fig. 32 (right) and in Fig. 39 in the appendix. These inconsistencies may be attributed to overheating of the melt pool, due to unsupported features in the nozzle. DebRoy et al.'s paper states that parts with overhanging features that do not have support structures may result in part distortion of the overhanging region induced either thermally or under its own weight [43].

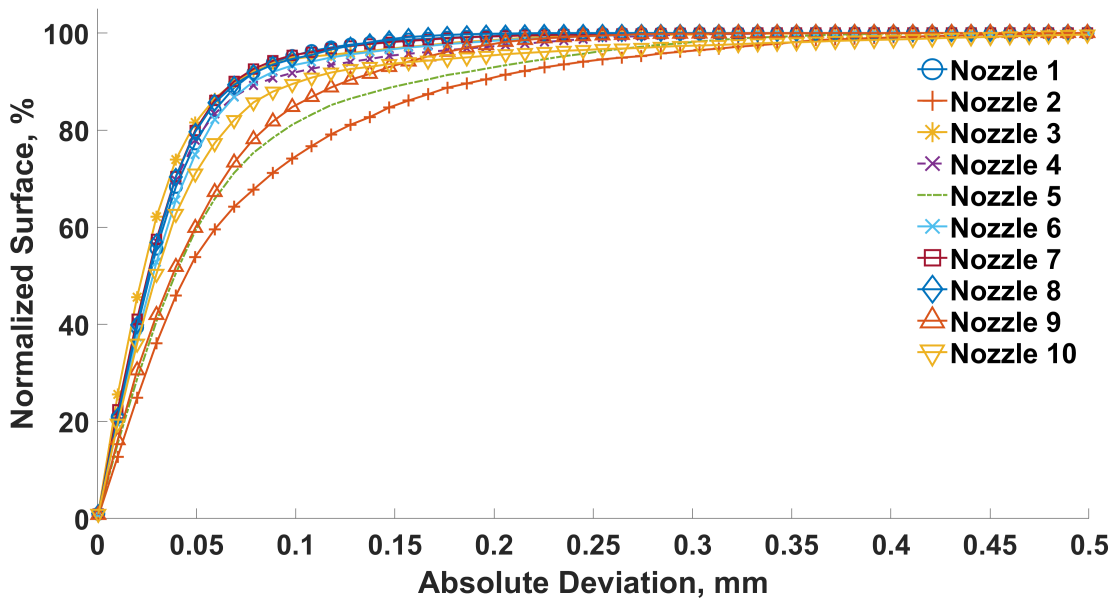


Figure 31: Normalized surface area of each 3D printed nozzle in relation to its deviation from the nominal surface of the inside of the HFSB nozzle

Table 2: 3D printed nozzles' surface roughness deviations for the inside of the HFSB nozzle at the 90th, 95th, and 98th percentiles

Nozzle Label	90 th percentile, mm	95 th percentile, mm	98 th percentile, mm
Nozzle 1	0.072	0.096	0.138
Nozzle 2	0.190	0.266	0.347
Nozzle 3	0.069	0.105	0.180
Nozzle 4	0.084	0.142	0.220
Nozzle 5	0.161	0.233	0.296
Nozzle 6	0.079	0.118	0.186
Nozzle 7	0.069	0.094	0.144
Nozzle 8	0.071	0.103	0.136
Nozzle 9	0.126	0.165	0.203
Nozzle 10	0.102	0.187	0.343

Figure 33 shows the HFSB diameter in relation to the surface roughness of the nozzle. While the HFSB diameter of the nozzles with a low surface roughness are within the same range, there was a drop in the HFSB diameter at 100 μm which then increased with increasing surface roughness for both a He:Soap ratio of 981 and 1083. Figure 34 compares the HFSB production rate to the surface roughness of each nozzle. The production rate increases until about 100 μm surface roughness, after which it declines with an increase in surface roughness. However, more data is needed to verify a trend between surface roughness and average production rate and bubble diameter.

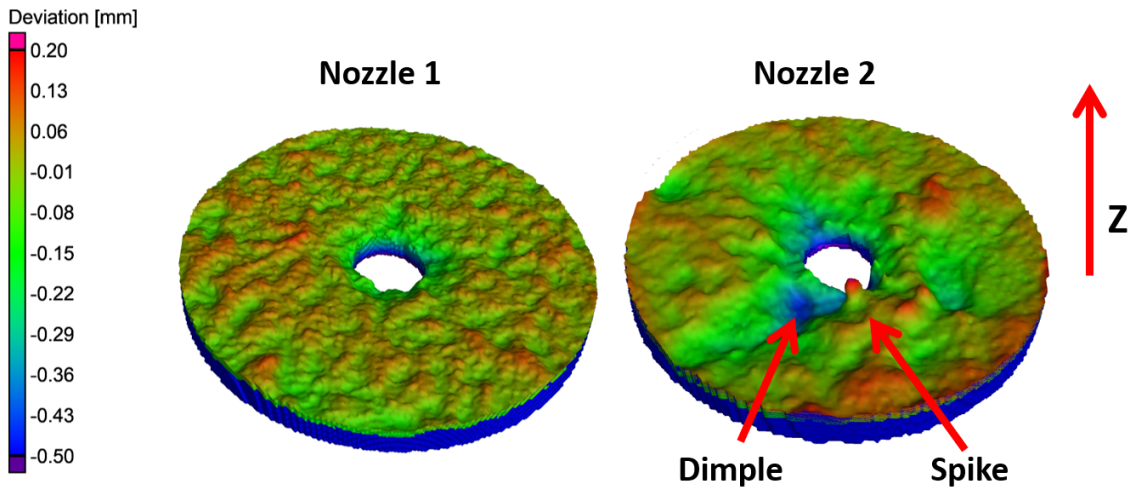


Figure 32: CT scan of the analyzed region of nozzle 1 depicting a rather smooth overhanging cap surface (left), and the CT scan of nozzle 2 depicting a large dimple and a spike on the surface of the cap (right)

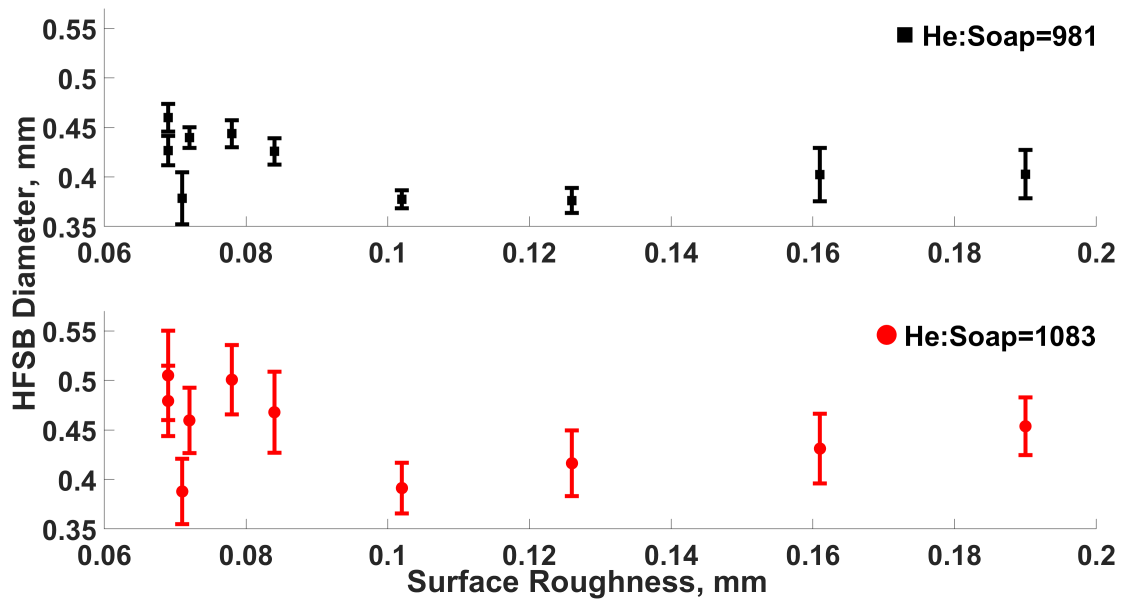


Figure 33: HFSB diameter for each metal 3D printed nozzle at He:Soap = 981 (top) and He:Soap = 1083 (bottom) versus the internal surface roughness deviation at the 90th percentile

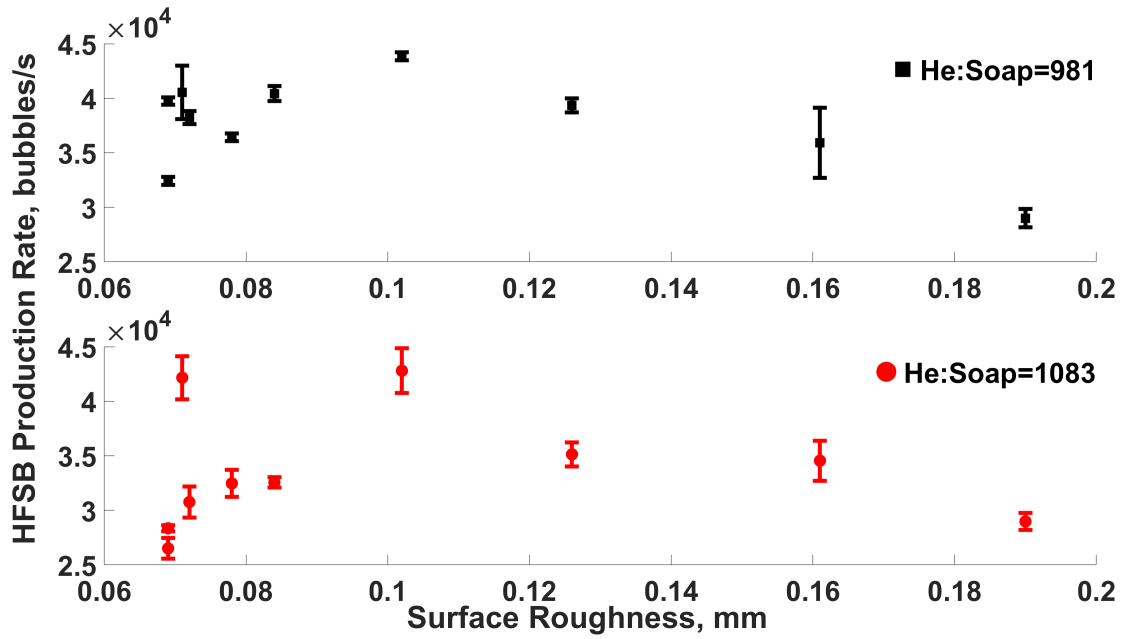


Figure 34: HFSB production rate for each metal 3D printed nozzle at He:Soap = 981 (top) and He:Soap = 1083 (bottom) versus the internal surface roughness deviation at the 90th percentile

While the production of HFSBs was consistent and relatively smooth throughout all nozzles, nozzle 2 operated inconsistently with pulsing behavior between HFSB production and sputtering. With the obtained CT reconstructions, this was attributed to two key differences between the nozzles. First, the surface roughness of nozzle 2 was significantly higher than all the other nozzles except for nozzle 5 and nozzle 9. Secondly, unlike the other nozzles, nozzle 2 showed a large depression, or dimple, as well as a spike in the surface of the overhanging region. These features are highlighted in Fig. 32 (right). The difference in the surface roughness of the nozzles may be attributed to the utilized scan strategies, but a further investigation into this is still necessary. Large overhangs like this are commonly avoided in additive manufacturing as they may lead to distortions and larger variations of the surface roughness [50, 51]. The CT scan results of the analyzed region for all ten nozzles is shown in Fig. 39 in the appendix.

Another notable observation is that nozzles with the lowest production rate variation were the ones with the lowest surface roughness, which indicates that a more consistent HFSB production may be achieved by a better surface finish at the nozzle cap. The four HFSB nozzles with the smallest production rate standard deviations, in order of smallest to largest, were nozzles 3, 6, 7, and 1 at a He:Soap ratio of 981, as depicted in Fig. 29 and Table 3. These

Table 3: 3D printed HFSB nozzle's average bubble diameters, production rates, standard deviations, and internal surface roughness deviations at two He:Soap ratios

Nozzle Label	He:Soap Ratio	Diameter (mm)	Production Rate (bubbles/s)	Surface Roughness Deviation (mm)
Nozzle 1	981	0.440 ± 0.011	38240 ± 594	0.072
	1083	0.460 ± 0.033	30760 ± 1431	0.072
Nozzle 2	981	0.403 ± 0.024	29010 ± 855	0.190
	1083	0.454 ± 0.029	28981 ± 784	0.190
Nozzle 3	981	0.460 ± 0.014	39760 ± 335	0.069
	1083	0.505 ± 0.045	28350 ± 267	0.069
Nozzle 4	981	0.426 ± 0.013	40430 ± 681	0.084
	1083	0.470 ± 0.041	32570 ± 465	0.084
Nozzle 5	981	0.402 ± 0.027	35920 ± 3212	0.161
	1083	0.431 ± 0.035	34550 ± 1839	0.161
Nozzle 6	981	0.444 ± 0.014	36420 ± 362	0.078
	1083	0.501 ± 0.035	32470 ± 1233	0.078
Nozzle 7	981	0.427 ± 0.015	32420 ± 363	0.069
	1083	0.479 ± 0.036	26510 ± 957	0.069
Nozzle 8	981	0.379 ± 0.026	40540 ± 2443	0.071
	1083	0.388 ± 0.033	42160 ± 1974	0.071
Nozzle 9	981	0.376 ± 0.013	39350 ± 647	0.126
	1083	0.416 ± 0.033	35130 ± 1095	0.126
Nozzle 10	981	0.377 ± 0.009	43850 ± 678	0.102
	1083	0.391 ± 0.026	42800 ± 2051	0.102

corresponded to four of the best nozzles in term of internal surface roughness, which can be observed at the 90th, 95th, and 98th percentiles in Table 2. It was also noted that nozzle 5 began to transition to the jetting regime at lower air flow rates than the other nozzles, which may have been attributed to nozzle 5's high surface roughness. This would have to be investigated further to conclude that surface roughness was the cause. Even though the internal surface roughness did not have a direct correlation to the HFSB diameter or to the average production rate, it did appear to directly affect the consistency of the HFSB production rate variation.

4.3 Benchmarking nozzle performance

To validate that the use of metal additive manufacturing is a viable manufacturing technique to produce HFSB nozzles, ten 3D printed nozzles were compared to other working HFSB nozzles in literature. Fig. 35 depicts the HFSB diameters for the majority of nozzles that were published

in literature. The average bubble diameter and standard deviation of the ten metal 3D printed nozzles are shown as the last 2 data points on the right side of Fig. 35. The average bubble diameters for the metal 3D printed nozzles are depicted on the plot with a He:Soap ratio of 981 and 1083. It can be observed that at He:Soap = 981, the bubble diameter and standard deviation was smaller than at He:Soap = 1083, 0.419 ± 0.0329 mm versus 0.452 ± 0.0524 mm. It can be seen that the diameter and standard deviation was similar to other published working HFSB nozzles and to a commercially sold HFSB generator from LaVision Inc. Even though a few nozzles were reported to have a lower bubble diameter than the metal printed nozzles, as long as the bubbles are small enough to be neutrally buoyant then they will work for PIV applications. If the bubbles become too large, then they will contain too much helium and become buoyant. Other papers that published a bubble diameter over 1 mm are mentioned in the caption below Fig. 35.

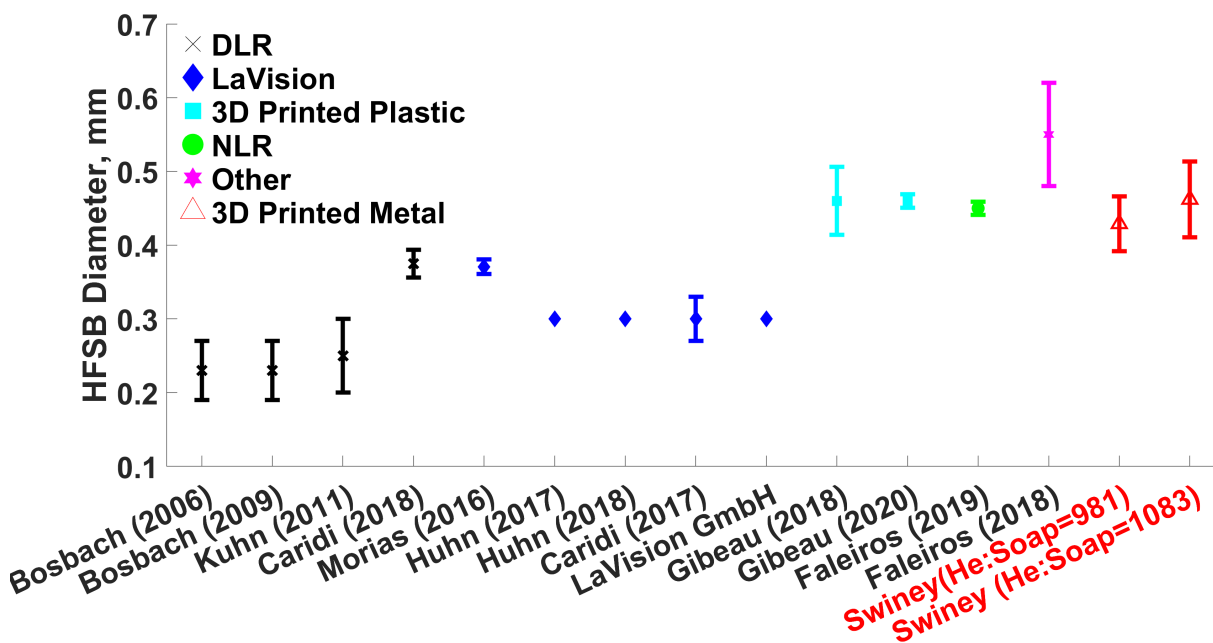


Figure 35: The average diameters and standard deviations for various HFSB produced from different nozzles published in literature are depicted. The x-axis has the last name of the primary author and year of the paper that the data was obtained from, and the y-axis is the HFSB diameter in millimeters. Papers that published a HFSB diameter above 1 mm are not shown in this plot (Müller [2] - 2 mm, Macháček [3] - 2-4.5 mm, Sun [4] - 1.3-3 mm, Lobutova [5] - 4 mm, Borer [6] - 2-3 mm, Sage Action Inc. - 1-4 mm).

Figure 36 depicts the HFSB production rates for papers found in literature. The error bars in this plot indicate the range of production rates that the nozzles were reported to operate

within. Some researchers only reported an approximate average production rate and no standard deviation or range of production rates, which is why some data points in the Fig. 36 do not have error bars. The metal 3D printed HFSB nozzle had a production rate that was comparable to the other nozzles, including the commercially available LaVision HFSB generator. Most HFSB nozzles that have been proven to work well for PIV operate at a production rate between 40,000 and 50,000 bubbles/s per nozzle. The ten metal 3D printed nozzles produced neutrally buoyant bubbles at an average production rate of 37594 ± 1017 and 33428 ± 1210 bubbles/s for the He:Soap ratio of 981 and 1083, respectively. At the optimal flow rate settings, the metal 3D printed nozzles were able to produce over 40,000 bubbles/s. Papers that published production rates below 1,000 bubbles/s or above 120,000 bubbles/s were mentioned in the caption below Fig. 36.

Most researchers that did not design their own HFSB nozzle performed research experiments with the German Aerospace Center's (DLR), LaVision Inc.'s, or the Netherlands Aerospace Centre's (NLR) HFSB nozzles. Gibeau et al. designed their own plastic 3D printed nozzle, and Faleiros et al. designed a HFSB nozzle which is listed under "other" in the legend. Comparing the HFSB nozzles' operating conditions to other nozzles in literature was one of the last steps in validating that the use of metal additive manufacturing is a viable option for manufacturing an HFSB nozzle to produce neutrally buoyant helium-filled soap bubbles.

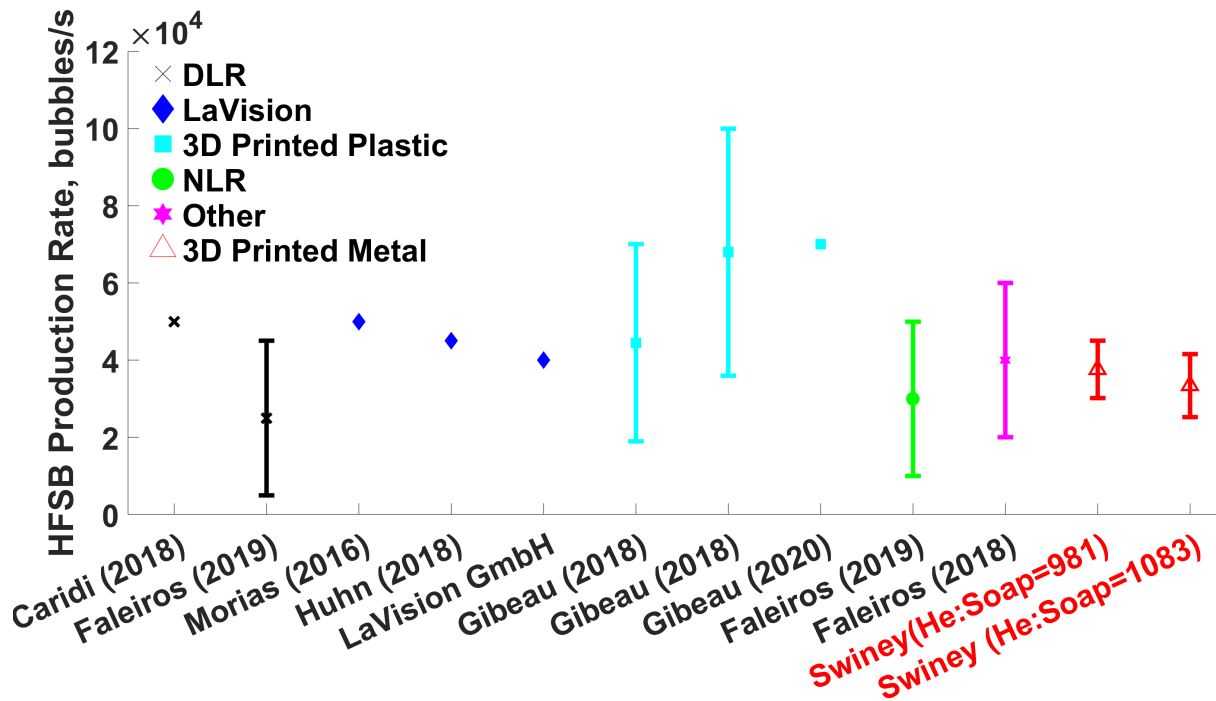


Figure 36: The ranges of production rates from different nozzles published in literature are depicted. The x-axis has the last name of the primary author and year of the paper that the data was obtained from, and the y-axis has the production rate in bubbles/s. An average of the ten metal 3D printed nozzles used in this study is shown by the far-right data points and the ranges that were observed at neutrally buoyant flow conditions is shown by error bars. Other papers that published a HFSB production rate below 1,000 bubbles/s or above 120,000 bubbles/s are not shown in this plot (Bosbach [7] - 200,000 bubbles/s, Macháček [3] - 500-700 bubbles/s, Borer [6] - 5-10 bubbles/s, Sage Action Inc. - 300-400 bubbles/s).

Chapter 5

Conclusion

The present experimental study focused on designing and developing a 3D printed metal nozzle to enable large field of view PIV. Additive manufacturing offers unique capabilities and advantages such as reduced production time and a cost-effective solution to producing these nozzles. Additive manufacturing helped during the design phase by allowing quick design iterations. The final nozzle design required only minimal post-processing, ensuring a smooth transition from printing to application for PIV experiments.

The HFSB system was characterized by measuring the bubble diameter and production rates as a function of air, helium, and soap flow rates to each nozzle. A model representing the bubble diameter was created using these flow rates to the nozzle. The metal 3D-printed nozzle had comparable bubble diameter and production rate to other nozzles that have been proven to work in literature for PIV applications.

X-ray CT was used to evaluate the consistency of the printed nozzles. The nozzles' performance was characterized by comparing its bubble diameter and production rate to each nozzles' internal surface roughness at the location where the bubbles exit. It was determined that the surface roughness of the inside of the nozzle does affect the nozzle's production consistency. However, the 3D printer was capable of producing nozzles with an adequate surface roughness given the correct printing parameters. Metal additive manufacturing was successfully used to print HFSB nozzles that produced bubbles of the correct diameter and production rate for neutral buoyancy for use in PIV experiments.

This study will enable future HFSB nozzles to be printed quicker and cheaper than present manufacturing techniques. The nozzles require almost no post-processing and multiple nozzles can be printed at one time. These HFSB nozzles will enable large field of view PIV experiments to be conducted for a variety of future experiments, such as high-shear and rotorcraft flows which are being studied in the Applied Fluids Research Group lab at Auburn University.

Chapter 6

Future Work

As a continuation of this work, the next step would be to verify the exact He:Soap ratio required for this metal nozzle design to ensure the bubbles being produced are neutrally buoyant. This is verified by calculating the tracing fidelity of the particles by measuring the bubbles' relaxation time and time response, which is detailed in [9, 12, 26]. The variation in production rates that was occurring in the FFT plots should be further investigated to determine if the nozzle was varying in its production rate and could be producing a bimodal distribution or if it was due to another reason.

The HFBSB system can be used to conduct future experiments that involve high-shear and volumetric PIV. Research can be conducted with rotorcraft flows and how they interact in various scenarios such as in ground effect or near a wall using volumetric PIV. Studying how smaller rotorcraft, such as UAVs, interact with obstacles is increasingly important with the rise in popularity of UAVs in everyday life, and HFBSBs would be good seeding particles to conduct experiments with these wall-bounded flows.

In addition to PIV applications, this project could be extended to further correlate various 3D printing parameters to the performance of the HFBSB nozzle. Printer parameters that could be investigated are print speed, hatch distance (distance between the scanning track), part orientation during printing, laser power, and scanning strategies. Modifications to the design could also be made to reduce the size of the overhanging section under the cap to improve the surface roughness of the nozzles. Other 3D printers and printing techniques could also be explored as the technology for metal additive manufacturing is improving. L-PBF was the best additive manufacturing printing method that was available at Auburn University and currently L-PBF provides the best dimensional accuracy for small parts. Other metal 3D printing techniques, such as directed energy deposition (wire DED) and laser engineered net shaping, work well for making large parts due to their higher deposition rates, but have worse dimensional accuracy and higher part surface roughness than powder bed fusion [52].

Improvements to the HFBS system could be made by using digital flow meters to regulate the air and helium flow, and using a multi-syringe pump to regulate the flow rate of soap solution. This would allow the flow measurements to be more accurate and easier to control. Using a multi-syringe pump would make it easier to operate multiple HFBS nozzles at a time, as an identical amount of soap solution would be going to each nozzle. One valve would no longer be controlling the soap solution to all nozzles, which would remove the error caused by splitting the flow of soap solution to multiple nozzles from the soap metering valve.

References

- [1] Markus Raffel, Christian E Willert, Fulvio Scarano, Christian J Kähler, Steve T Wereley, and Jürgen Kompenhans. Particle image velocimetry: a practical guide. Springer, 2018.
- [2] R. H. G. Müller, H. Flögel, Th Scherer, O. Schaumann, and M. Markwart. Investigation of large scale low speed air conditioning flow using piv. In 9th international symposium on flow visualization, 2000.
- [3] Matthias Macháček. A quantitative visualization tool for large wind tunnel experiments. PhD thesis, ETH Zurich, 2002.
- [4] Yigang Sun, Yuanhui Zhang, Aijun Wang, Jennifer L Topmiller, and James S Bennet. Experimental characterization of airflows in aircraft cabins, part i: experimental system and measurement procedure. ASHRAE transactions, 111(2), 2005.
- [5] Elka Lobutova, Christian Resagk, Robert Rank, and Dirk Müller. Extended three dimensional particle tracking velocimetry for large enclosures. In Imaging measurement methods for flow analysis, pages 113–124. Springer, 2009.
- [6] David J Borer. 4D flow visualization with dynamic vision sensors. PhD thesis, ETH Zurich, 2014.
- [7] Johannes Bosbach, Matthias Kühn, and Claus Wagner. Large scale particle image velocimetry with helium filled soap bubbles. Experiments in fluids, 46(3):539–547, 2009.
- [8] Bradley Gibeau, Findlay McCormick, and Sina Ghaemi. Design and characterization of a 3d-printed helium-filled soap bubble generator for large-scale volumetric flow measurements. In 19th International Symposium on the Application of Laser and Imaging Techniques to Fluid Mechanics, Lisbon, Portugal, 2018.
- [9] Bradley Gibeau and Sina Ghaemi. A modular, 3d-printed helium-filled soap bubble generator for large-scale volumetric flow measurements. Experiments in Fluids, 59(12):178, 2018.

- [10] Bradley Gibeau, Drew Gingras, and Sina Ghaemi. Evaluation of a full-scale helium-filled soap bubble generator. Experiments in Fluids, 61(2):1–18, 2020.
- [11] Xiaodong Cao, Junjie Liu, Nan Jiang, and Qingyan Chen. Particle image velocimetry measurement of indoor airflow field: a review of the technologies and applications. Energy and Buildings, 69:367–380, 2014.
- [12] Fulvio Scarano, Sina Ghaemi, Giuseppe Carlo Alp Caridi, Johannes Bosbach, Uwe Dierksheide, and Andrea Sciacchitano. On the use of helium-filled soap bubbles for large-scale tomographic piv in wind tunnel experiments. Experiments in Fluids, 56(2):42, 2015.
- [13] Ian Grant. Particle image velocimetry: a review. Proceedings of the Institution of Mechanical Engineers, Part C: Journal of Mechanical Engineering Science, 211(1):55–76, 1997.
- [14] Johannes Bosbach, Matthias Kühn, Claus Wagner, Markus Raffel, Christian Resagk, Ronald du Puits, and André Theess. Large scale particle image velocimetry of natural and mixed convection. In 13th Int. Symp. on Applications of Laser Techniques to Fluid Mechanics, Lisbon, Portugal, 2006.
- [15] Matthias Kühn, Klaus Ehrenfried, Johannes Bosbach, and Claus Wagner. Large-scale tomographic particle image velocimetry using helium-filled soap bubbles. Experiments in fluids, 50(4):929–948, 2011.
- [16] Giuseppe Carlo Alp Caridi. Development and application of helium-filled soap bubbles: For large-scale PIV experiments in aerodynamics. PhD thesis, Delft University of Technology, 2018.
- [17] Giuseppe Carlo Alp Caridi, Daniele Ragni, Andrea Sciacchitano, and Fulvio Scarano. Hfsb-seeding for large-scale tomographic piv in wind tunnels. Experiments in Fluids, 57(12):190, 2016.

- [18] C Resagk, R du Puits, A Maystrenko, A Thess, J Bosbach, and C Wagner. Large-scale particle image velocimetry in convective airflow. In Proc. 6th int. symposium on particle image velocimetry, 2005.
- [19] Y Okuno, T Fukuda, Y Miwate, and T Kobayashi. Development of three dimensional air flow measuring method using soap bubbles. JSAE Review, 14(4):50–55, 1993.
- [20] HH Flogel, W Sommerer, and K. Kuonath. Blasengenerator, 1997.
- [21] Louise Lu and Volker Sick. High-speed particle image velocimetry near surfaces. JoVE (Journal of Visualized Experiments), page e50559, 2013.
- [22] David Engler Faleiros, Marthijn Tuinstra, Andrea Sciacchitano, and Fulvio Scarano. Generation and control of helium-filled soap bubbles for piv. Experiments in Fluids, 60(3):40, 2019.
- [23] D. Engler Faleiros, Marthijn Tuinstra, A. Sciacchitano, and F. Scarano. Generation and control of helium-filled soap bubbles for large-scale piv. In LXLASER2018: 19th International Symposium on the Application of Laser and Imaging Techniques to Fluid Mechanics, 2018.
- [24] RHG Müller, Th Scherer, Th Rotger, O Schaumann, and M Markwart. Large body aircraft cabin a/c flow measurement by helium bubble tracking. Journal of Flow Visualization and Image Processing, 4(3), 1997.
- [25] Lingying Zhao, Yuanhui Zhang, Xinlei Wang, GL Riskowski, and LL Christianson. Measurement of airflow patterns in ventilated spaces using particle image velocimetry. In An ASAE Meeting Presentation, Paper, 1999.
- [26] David Engler Faleiros, Marthijn Tuinstra, Andrea Sciacchitano, and Fulvio Scarano. Helium-filled soap bubbles tracing fidelity in wall-bounded turbulence. Experiments in Fluids, 59(3):56, 2018.

- [27] Yuji Suzuki and Nobuhide Kasagi. Turbulent air-flow measurement with the aid of 3-d particle tracking velocimetry in a curved square bend. Flow, turbulence and combustion, 63(1-4):415, 2000.
- [28] D Müller, B Müller, and U Renz. Three-dimensional particle-streak tracking (pst) velocity measurements of a heat exchanger inlet flow: A new method to measure all three air-flow velocity components in a plane is applied to a steady-state three-dimensional flow. Experiments in Fluids, 30(6):645–656, 2001.
- [29] Florian Huhn, Daniel Schanz, Sebastian Gesemann, Uwe Dierksheide, Remco van de Meerendonk, and Andreas Schröder. Large-scale volumetric flow measurement in a pure thermal plume by dense tracking of helium-filled soap bubbles. Experiments in Fluids, 58(9):116, 2017.
- [30] F Huhn, D Schanz, P Manovski, S Gesemann, and A Schröder. Time-resolved large-scale volumetric pressure fields of an impinging jet from dense lagrangian particle tracking. Experiments in Fluids, 59(5):81, 2018.
- [31] Jan FG Schneiders, Giuseppe CA Caridi, Andrea Sciacchitano, and Fulvio Scarano. Large-scale volumetric pressure from tomographic ptv with hfsb tracers. Experiments in Fluids, 57(11):164, 2016.
- [32] Gustavo CR Bodstein, Albert R George, and C-Y Hui. The three-dimensional interaction of a streamwise vortex with a large-chord lifting surface: theory and experiment. Journal of Fluid Mechanics, 322:51–79, 1996.
- [33] Giuseppe Carlo Alp Caridi, Andrea Sciacchitano, and Fulvio Scarano. Helium-filled soap bubbles for vortex core velocimetry. Experiments in Fluids, 58(9):130, 2017.
- [34] Christina Politz, Reinhard Geisler, and Sudesh Ranasinghe. Ground based large scale wake vortex investigations by means of particle image velocimetry: a feasibility study. In Advanced In-Flight Measurement Techniques, pages 291–304. Springer, 2013.

- [35] Koen LL Morias, Giuseppe CA Caridi, Andrea Sciacchitano, and Fulvio Scarano. Statistical characterization of helium-filled soap bubbles tracing fidelity for piv. In 18th international symposium on the application of laser and imaging techniques to fluid mechanics, Lisbon, 2016.
- [36] Jan FG Schneiders, Fulvio Scarano, Constantin Jux, and Andrea Sciacchitano. Coaxial volumetric velocimetry. Measurement Science and Technology, 29(6):065201, 2018.
- [37] Alejandro del Estal Herrero, Mustafa Percin, Matej Karasek, and Bas van Oudheusden. Flow visualization around a flapping-wing micro air vehicle in free flight using large-scale piv. Aerospace, 5(4):99, 2018.
- [38] W Terra, A Sciacchitano, and F Scarano. Aerodynamic drag of a transiting sphere by large-scale tomographic-piv. Experiments in Fluids, 58(7):83, 2017.
- [39] Constantin Jux, Andrea Sciacchitano, Jan FG Schneiders, and Fulvio Scarano. Robotic volumetric piv of a full-scale cyclist. Experiments in Fluids, 59(4):74, 2018.
- [40] R Refaie, P Rushton, P McGovern, D Thompson, I Serrano-Pedraza, KS Rankin, and M Reed. The effect of operating lights on laminar flow: an experimental study using neutrally buoyant helium bubbles. The bone & joint journal, 99(8):1061–1066, 2017.
- [41] Michael F Kerho and Michael B Bragg. Neutrally buoyant bubbles used as flow tracers in air. Experiments in Fluids, 16(6):393–400, 1994.
- [42] Wei Gao, Yunbo Zhang, Devarajan Ramanujan, Karthik Ramani, Yong Chen, Christopher B Williams, Charlie CL Wang, Yung C Shin, Song Zhang, and Pablo D Zavattieri. The status, challenges, and future of additive manufacturing in engineering. Computer-Aided Design, 69:65–89, 2015.
- [43] Tarasankar DebRoy, HL Wei, JS Zuback, T Mukherjee, JW Elmer, JO Milewski, Allison Michelle Beese, A Wilson-Heid, A De, and W Zhang. Additive manufacturing of metallic components—process, structure and properties. Progress in Materials Science, 92:112–224, 2018.

- [44] Dongdong Gu, Yves-Christian Hagedorn, Wilhelm Meiners, Guangbin Meng, Rui João Santos Batista, Konrad Wissenbach, and Reinhart Poprawe. Densification behavior, microstructure evolution, and wear performance of selective laser melting processed commercially pure titanium. Acta Materialia, 60(9):3849–3860, 2012.
- [45] Luke N Carter, Christopher Martin, Philip J Withers, and Moataz M Attallah. The influence of the laser scan strategy on grain structure and cracking behaviour in slm powder-bed fabricated nickel superalloy. Journal of Alloys and Compounds, 615:338–347, 2014.
- [46] Aleksis Karme, Aki Kallonen, Ville-Pekka Matilainen, Heidi Piili, and Antti Salminen. Possibilities of ct scanning as analysis method in laser additive manufacturing. Physics Procedia, 78:347–356, 2015.
- [47] C. L. Druzgalski, A. Ashby, G. Guss, W. E. King, T. T. Roehling, and M. J. Matthews. Process optimization of complex geometries using feed forward control for laser powder bed fusion additive manufacturing. Additive Manufacturing, page 101169, 2020.
- [48] Marco Grasso and Bianca Maria Colosimo. Process defects and in situ monitoring methods in metal powder bed fusion: a review. Measurement Science and Technology, 28:044005, 2017.
- [49] Anton Du Plessis, Philip Sperling, Andre Beerlink, Oelof Kruger, Lerato Tshabalala, Shaik Hoosain, and Stephan G Le Roux. Standard method for microct-based additive manufacturing quality control 3: surface roughness. MethodsX, 5:1111–1116, 2018.
- [50] Jason C. Fox, Shawn P. Moylan, and Brandon M. Lane. Effect of process parameters on the surface roughness of overhanging structures in laser powder bed fusion additive manufacturing. Procedia Cirp, 45:131–134, 2016.
- [51] Raya Mertens, Stijn Clijsters, Karolien Kempen, and Jean-Pierre Kruth. Optimization of scan strategies in selective laser melting of aluminum parts with downfacing areas. Journal of Manufacturing Science and Engineering, 136, 2014.

[52] Takeyuki Abe and Hiroyuki Sasahara. Dissimilar metal deposition with a stainless steel and nickel-based alloy using wire and arc-based additive manufacturing. Precision Engineering, 45:387–395, 2016.

Appendices
Appendix A

Drawing of Final Integrated Nozzle Design

Figure 37 is the CAD drawing used to 3D print the integrated HFSB nozzle on the GE Concept Laser Mlab cusing R printer. All drawing dimensions are in mm.

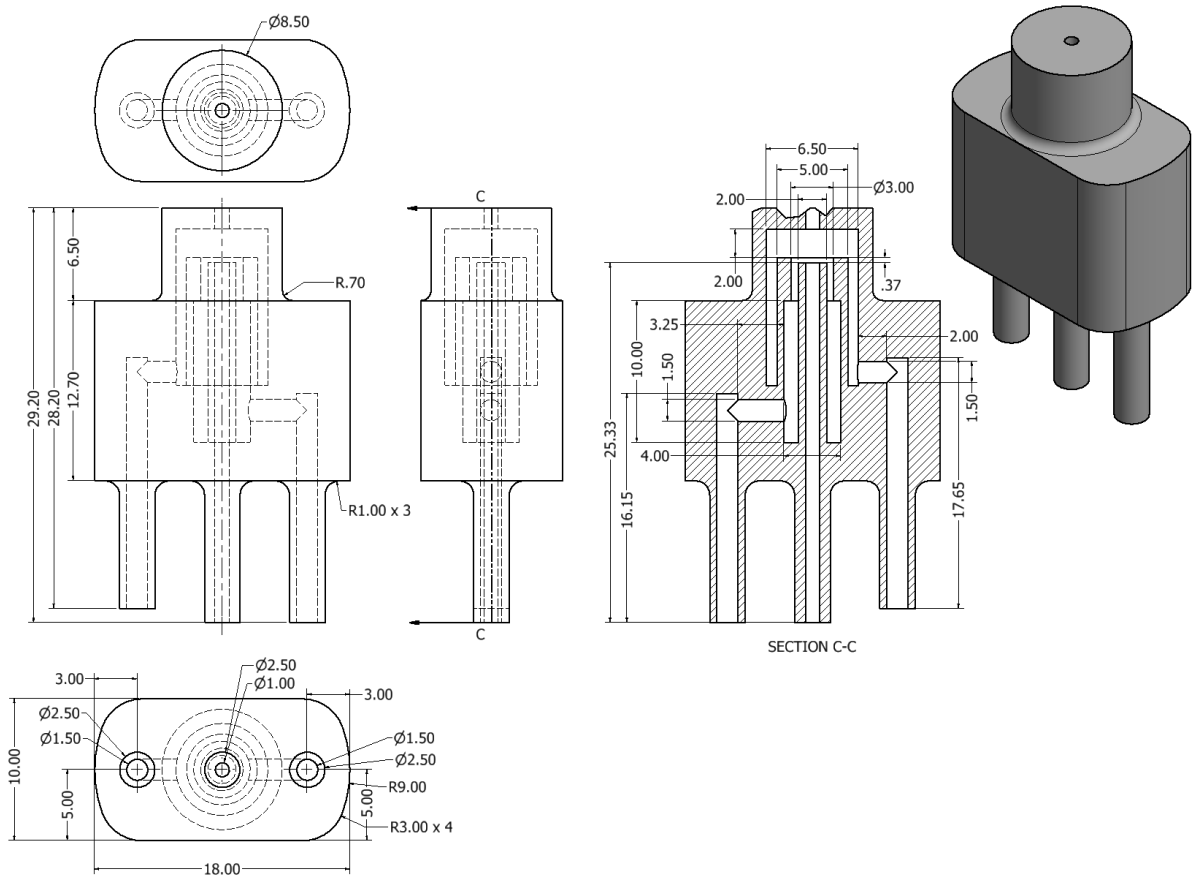


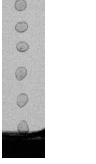
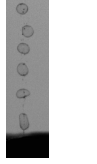
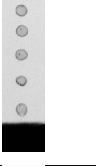
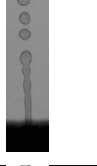





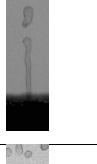

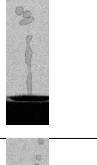

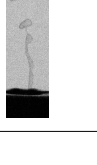

Figure 37: CAD drawing of final HFSB nozzle design

Appendix B

Tested Flow Rates and Bubble Characteristics

Sample HFBSB images are provided for each air flow rate for nozzle 1 below. The approximate regime and corresponding He:Soap ratio, as described in Fig. 22, that the nozzle was operating within is listed in Table 4. Occasionally, the nozzle would begin jetting at a lower or higher He:Soap ratio than listed.

Table 4: Tested flow rate ranges and bubble characteristics with sample HFSB images

Air (L/h)	He:Soap Ratio	Regime	Sample Images	Air (L/h)	He:Soap Ratio	Regime	Sample Images
65.3	1225-2166	Bubbling (a)		87.0	1225-2166	Jetting	
87.0	613-1120	Bubbling (a)		108.8	1225-2166	Jetting	
108.8	613-1120	Bubbling (a)		130.5	1225-2166	Jetting	
130.5	613-1120	Bubbling (a)		152.3	1225-2166	Jetting	
152.3	613-1308	Bubbling (a)		174.0	1225-2166	Jetting	
174.0	613-1120	Bubbling (a)		195.8	497-1624	Jetting	
43.5	919-1802	Bubbling (b)		217.5	497-1624	Jetting	
65.3	613-1120	Bubbling (b)					

Appendix C

FFT Production Rate Plots

Sample FFT production rate frequency plots are depicted below for all ten HFSB nozzles. These frequency plots were for a He:Soap ratio of 981 and an air flow rate of 152.3 L/h.

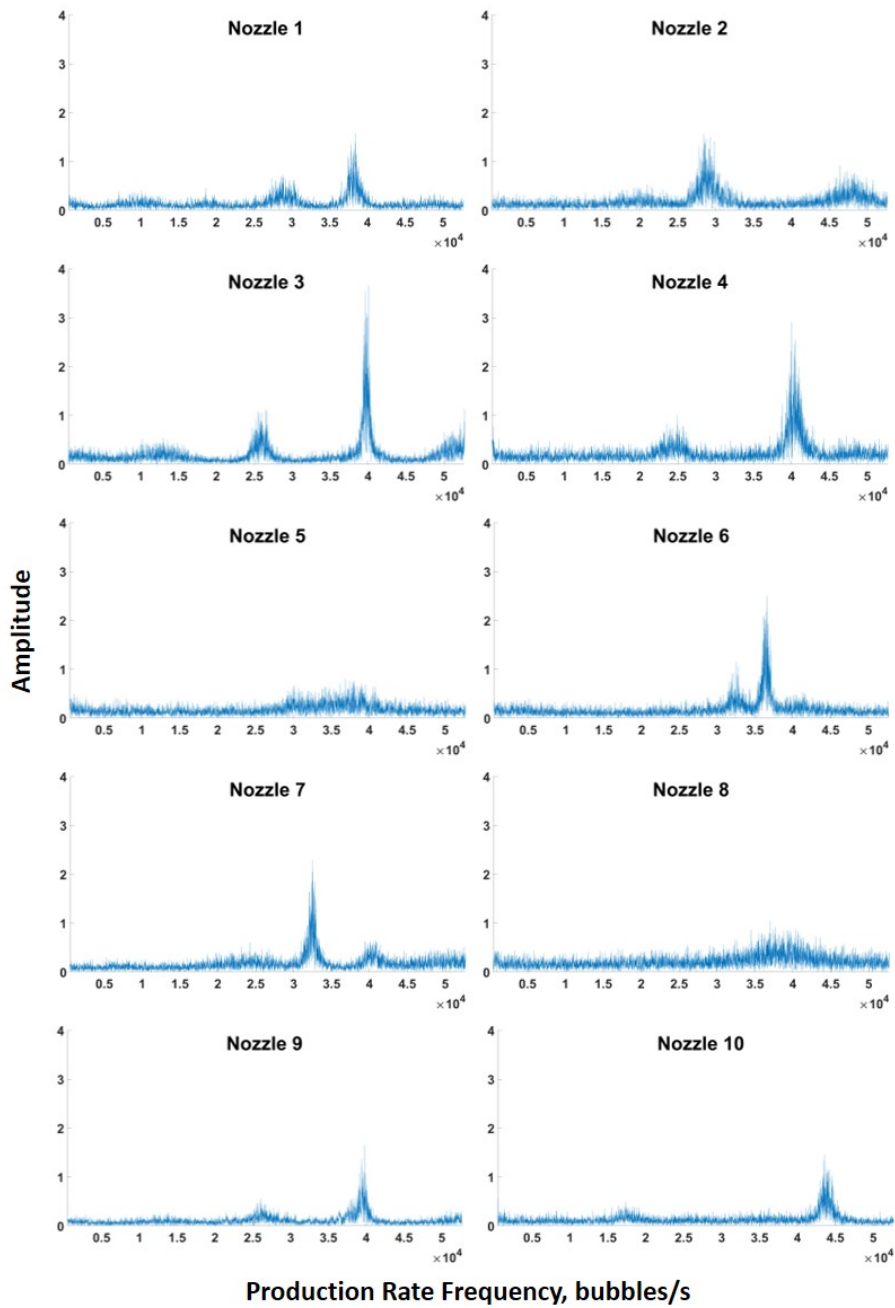


Figure 38: FFT production rate plots for all HFSB nozzles

Appendix D

Computed Tomography Scans

The surface roughness deviation results from the CT scans of each of the HFSB nozzles is depicted below. It can be observed that the surface roughness in all of the nozzles are very similar, other than nozzle 2. It can also be observed that the surface roughness across the analyzed region is consistent and fairly smooth for an internal overhanging 3D printed region. All nozzles, except nozzle 2, were printed with the same print settings, and nozzles 3-10 were printed at the same time. This indicates that the metal 3D printer is consistent and has a sufficient spatial resolution to print HFSB nozzles.

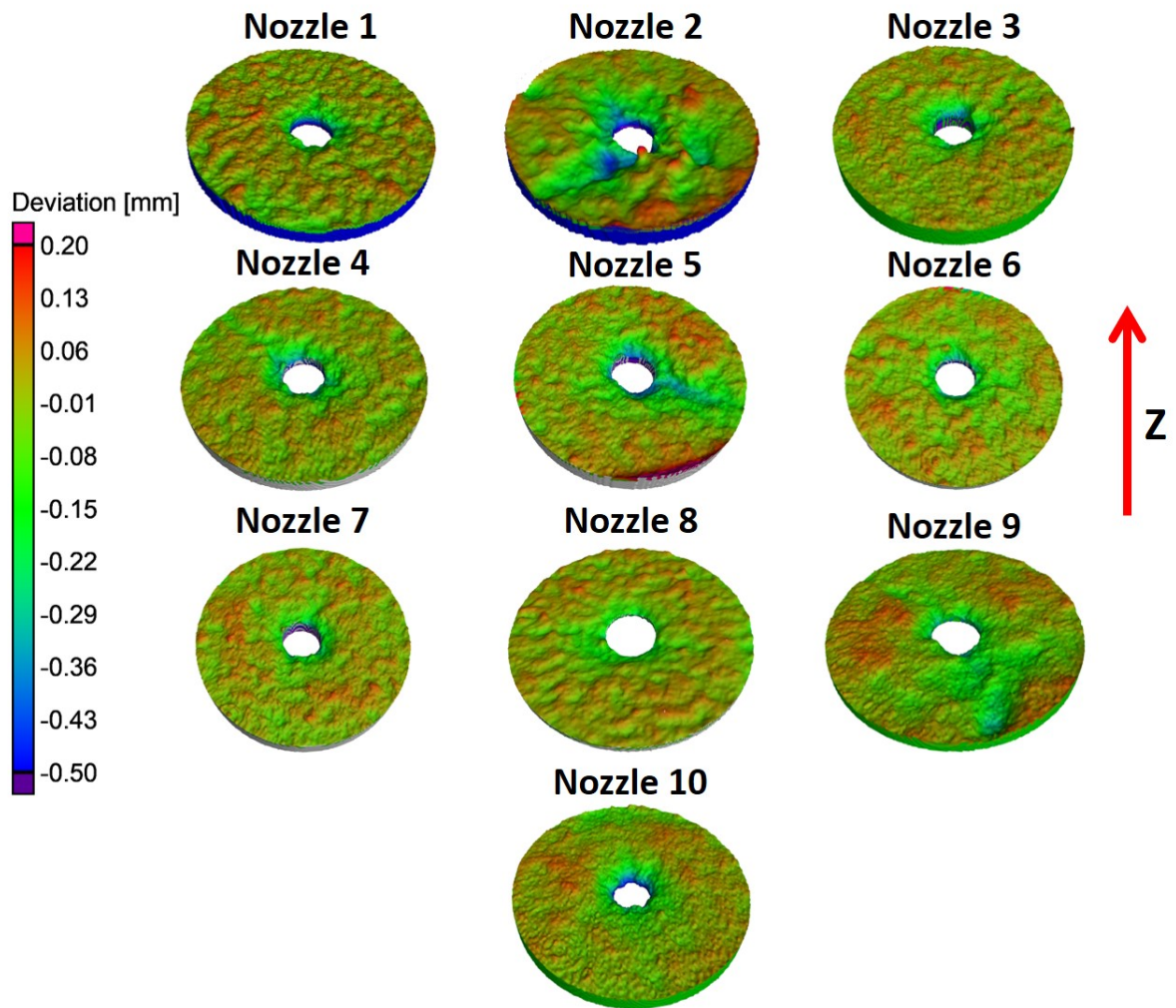


Figure 39: CT scans depicting the surface deviation for the analyzed region of the cap for all ten 3D printed HFSB nozzles

Appendix E

SAS Figures

The results from the regression analysis in SAS for the neutrally and non-neutrally buoyant HFSB data is depicted below. Figures 40 and 45 are fitted plots depicting how air flow rate to the nozzle has a large influence on the HFSB diameter. Figures 41, 42, 43, 44, 46, 47, 48, and 49 show the residuals, p-values, standard errors, R^2 values, and other statistical parameters for each of the explanatory variables that were included in the regression models. The variable listed as “AHS” in the tables represents the interaction effects between the flow rate of air, helium, and soap.

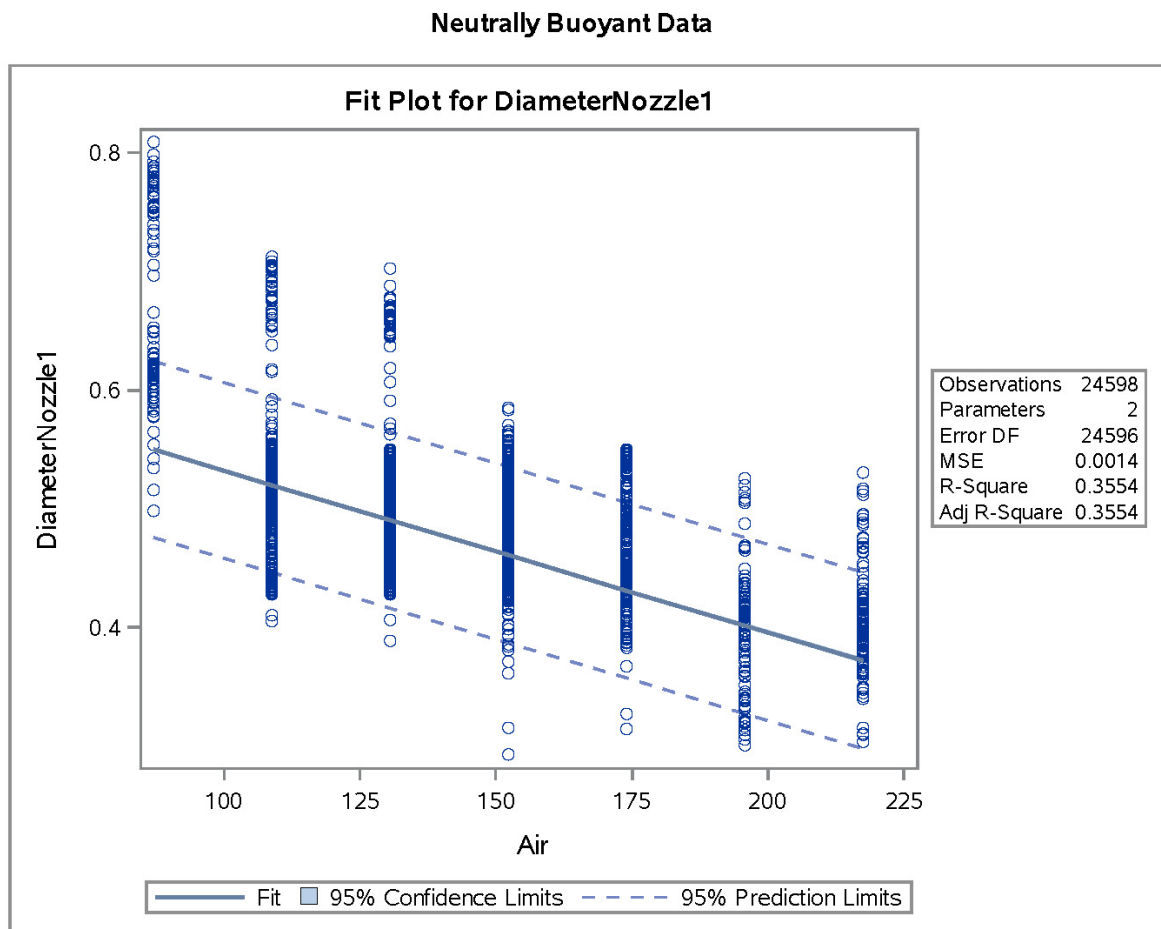


Figure 40: Neutrally buoyant fit plot for air flow rate in SAS

Neutrally Buoyant Data

The REG Procedure
Model: MODEL1
Dependent Variable: DiameterNozzle1

Number of Observations Read	24598
Number of Observations Used	24598

Analysis of Variance					
Source	DF	Sum of Squares	Mean Square	F Value	Pr > F
Model	8	30.68621	3.83578	3934.34	<.0001
Error	24589	23.97300	0.00097495		
Corrected Total	24597	54.65921			

Root MSE	0.03122	R-Square	0.5614
Dependent Mean	0.47980	Adj R-Sq	0.5613
Coeff Var	6.50781		

Parameter Estimates					
Variable	DF	Parameter Estimate	Standard Error	t Value	Pr > t
Intercept	1	2.23959	0.05608	39.94	<.0001
LogAir	1	-0.26502	0.01492	-17.77	<.0001
Air	1	-0.00468	0.00024497	-19.11	<.0001
Helium	1	-0.00894	0.00291	-3.07	0.0021
Soap	1	-0.08863	0.00253	-35.01	<.0001
Air_Helium	1	0.00014117	0.00002067	6.83	<.0001
Air_Soap	1	0.00075220	0.00001911	39.36	<.0001
Helium_Soap	1	0.00407	0.00013230	30.74	<.0001
AHS	1	-0.00003498	9.951314E-7	-35.15	<.0001

Figure 41: Neutrally buoyant SAS data

Neutrally Buoyant Data

The REG Procedure
Model: MODEL1
Dependent Variable: DiameterNozzle1

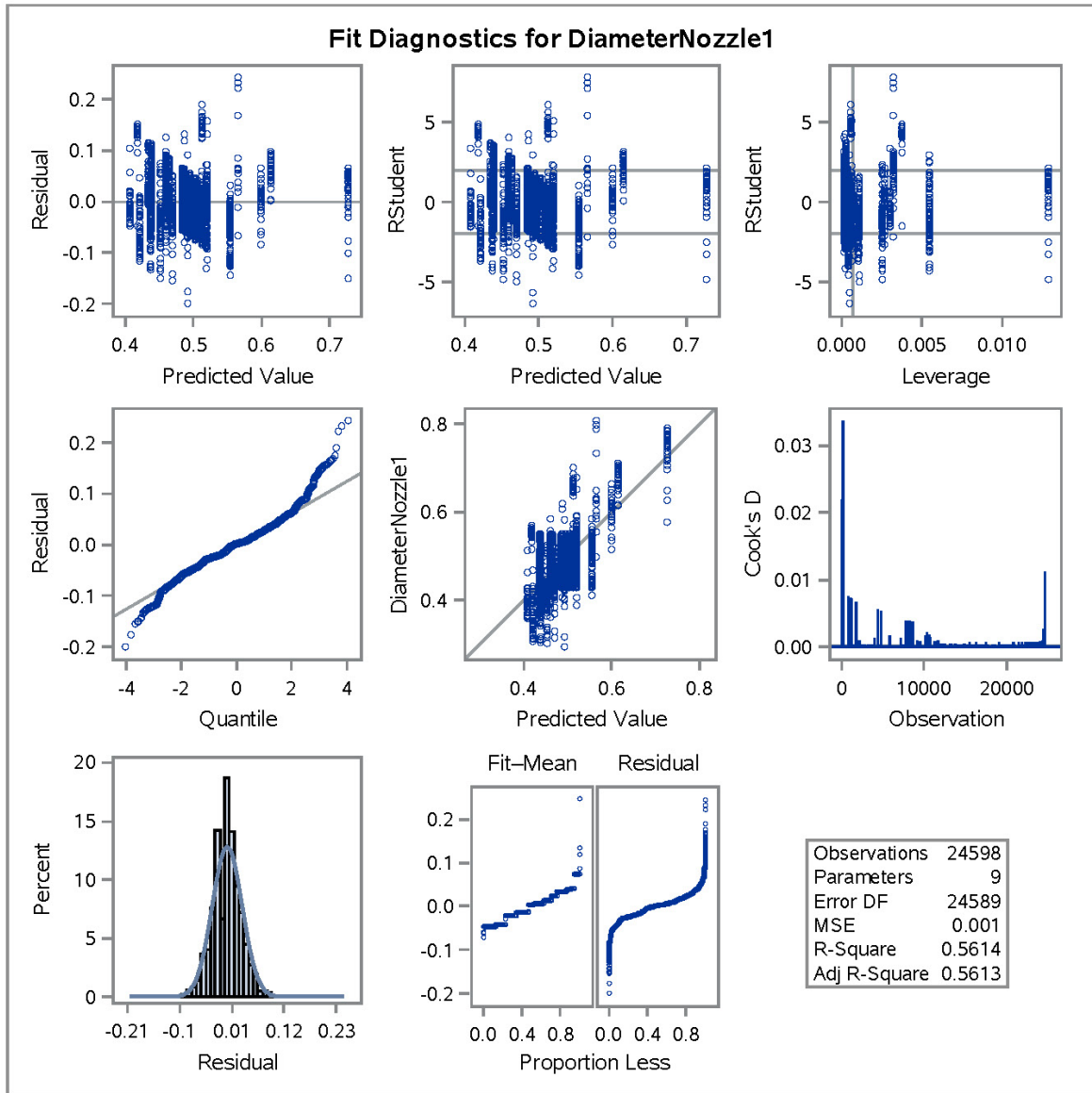


Figure 42: Neutrally buoyant SAS data

Neutrally Buoyant Data
The REG Procedure
Model: MODEL1
Dependent Variable: DiameterNozzle1

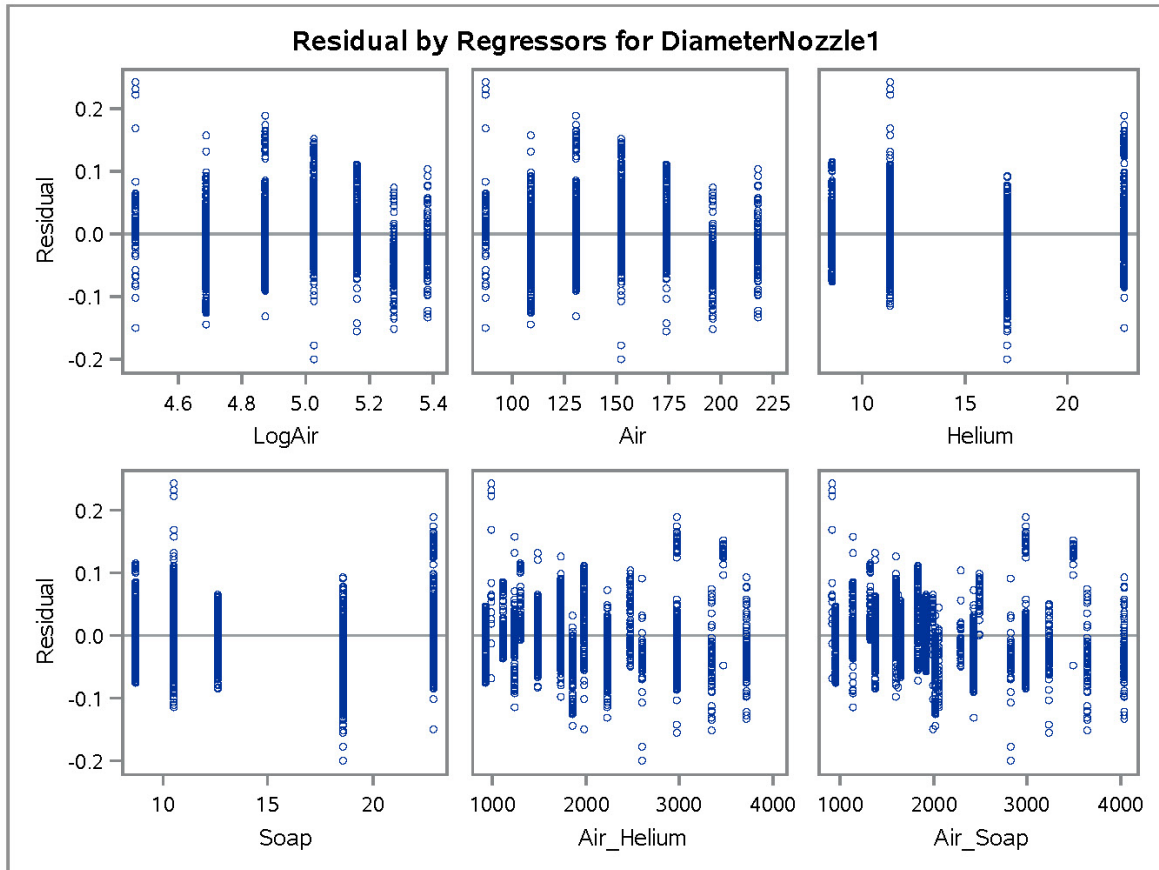


Figure 43: Neutrally buoyant SAS data

Neutrally Buoyant Data
The REG Procedure
Model: MODEL1
Dependent Variable: DiameterNozzle1

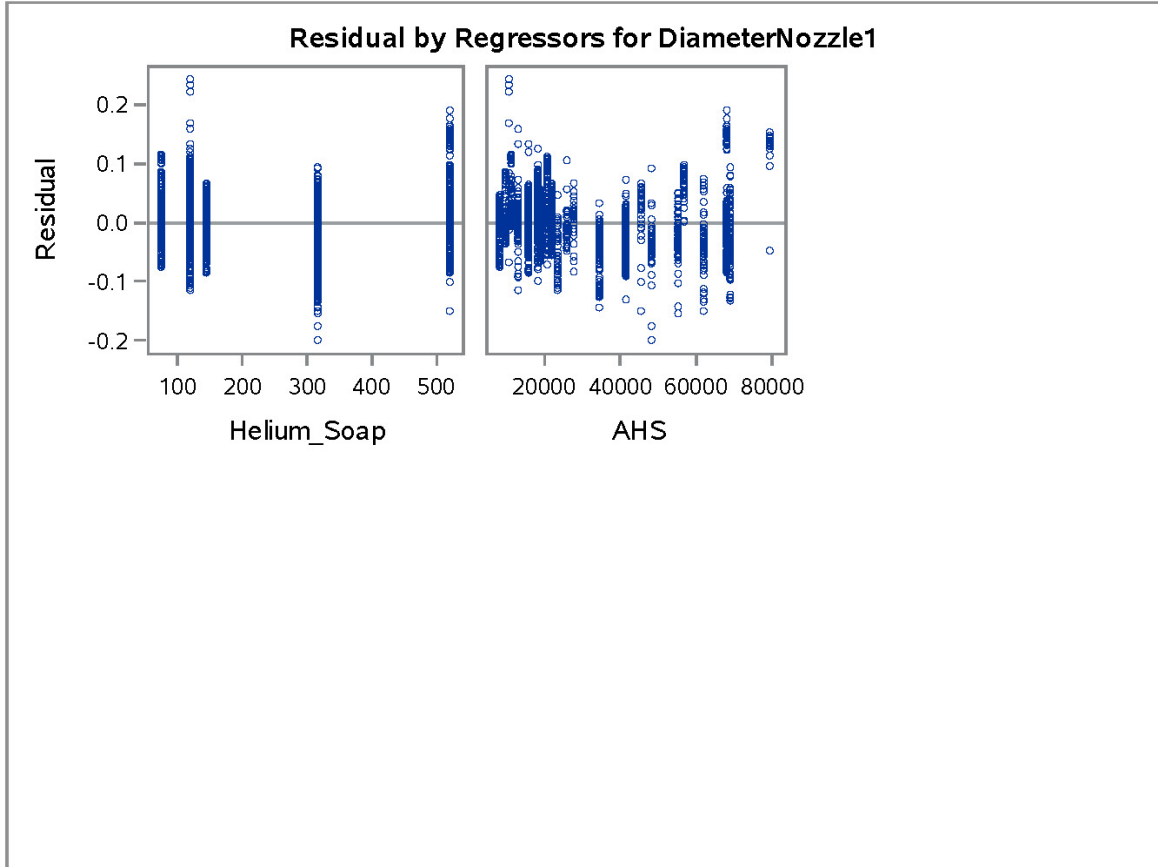


Figure 44: Neutrally buoyant SAS data

All Nozzle 1 Data

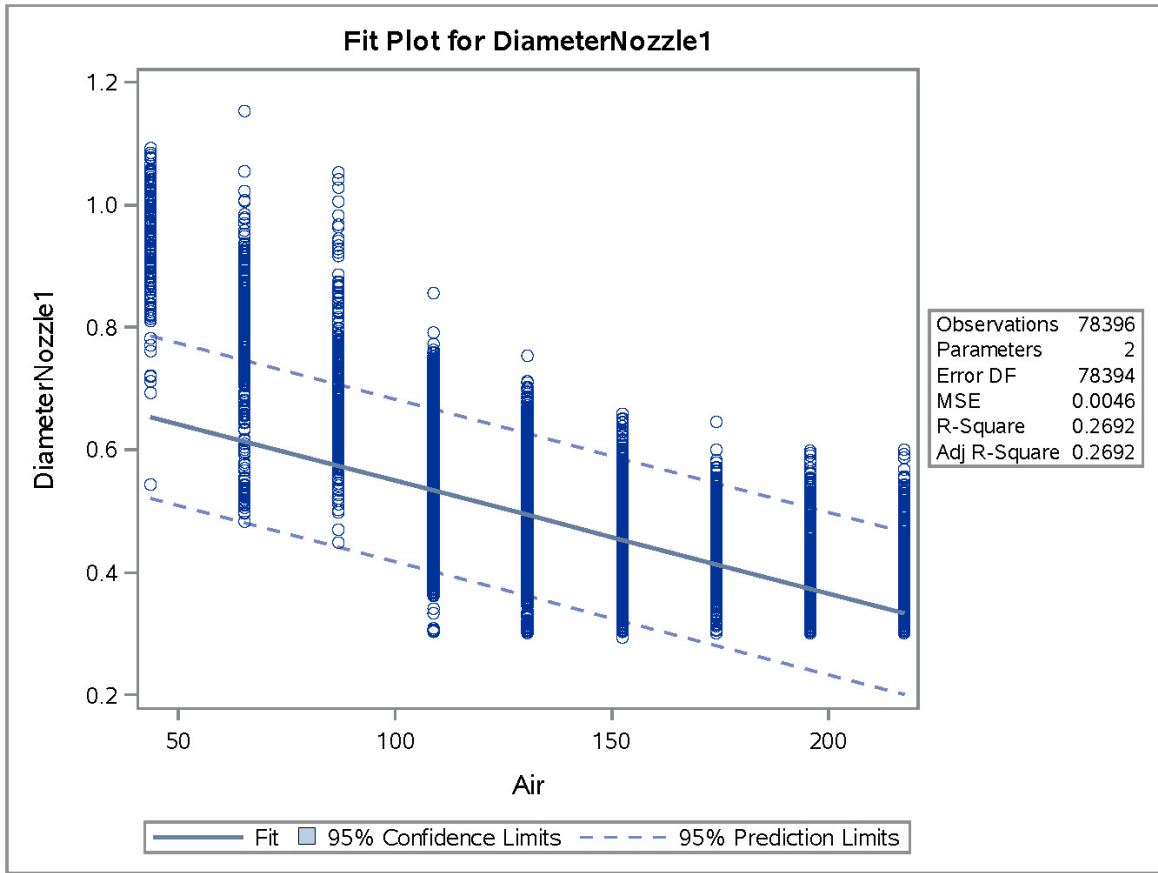


Figure 45: Neutrally and non-neutrally buoyant fit plot for air flow rate in SAS

All Nozzle 1 Data

The REG Procedure
 Model: MODEL1
 Dependent Variable: DiameterNozzle1

Number of Observations Read	78396
Number of Observations Used	78396

Analysis of Variance					
Source	DF	Sum of Squares	Mean Square	F Value	Pr > F
Model	8	353.73330	44.21666	25396.9	<.0001
Error	78387	136.47373	0.00174		
Corrected Total	78395	490.20703			

Root MSE	0.04173	R-Square	0.7216
Dependent Mean	0.49209	Adj R-Sq	0.7216
Coeff Var	8.47929		

Parameter Estimates					
Variable	DF	Parameter Estimate	Standard Error	t Value	Pr > t
Intercept	1	2.18538	0.02077	105.22	<.0001
LogAir	1	-0.53185	0.00533	-99.86	<.0001
Air	1	0.00494	0.00008777	56.24	<.0001
Helium	1	0.01826	0.00068676	26.59	<.0001
Soap	1	0.04731	0.00061394	77.06	<.0001
Air_Helium	1	-0.00005031	0.00000538	-9.36	<.0001
Air_Soap	1	-0.00022128	0.00000478	-46.26	<.0001
Helium_Soap	1	-0.00143	0.00004207	-34.08	<.0001
AHS	1	0.00000513	3.324299E-7	15.42	<.0001

Figure 46: Neutrally and non-neutrally buoyant SAS data

All Nozzle 1 Data
The REG Procedure
Model: MODEL1
Dependent Variable: DiameterNozzle1

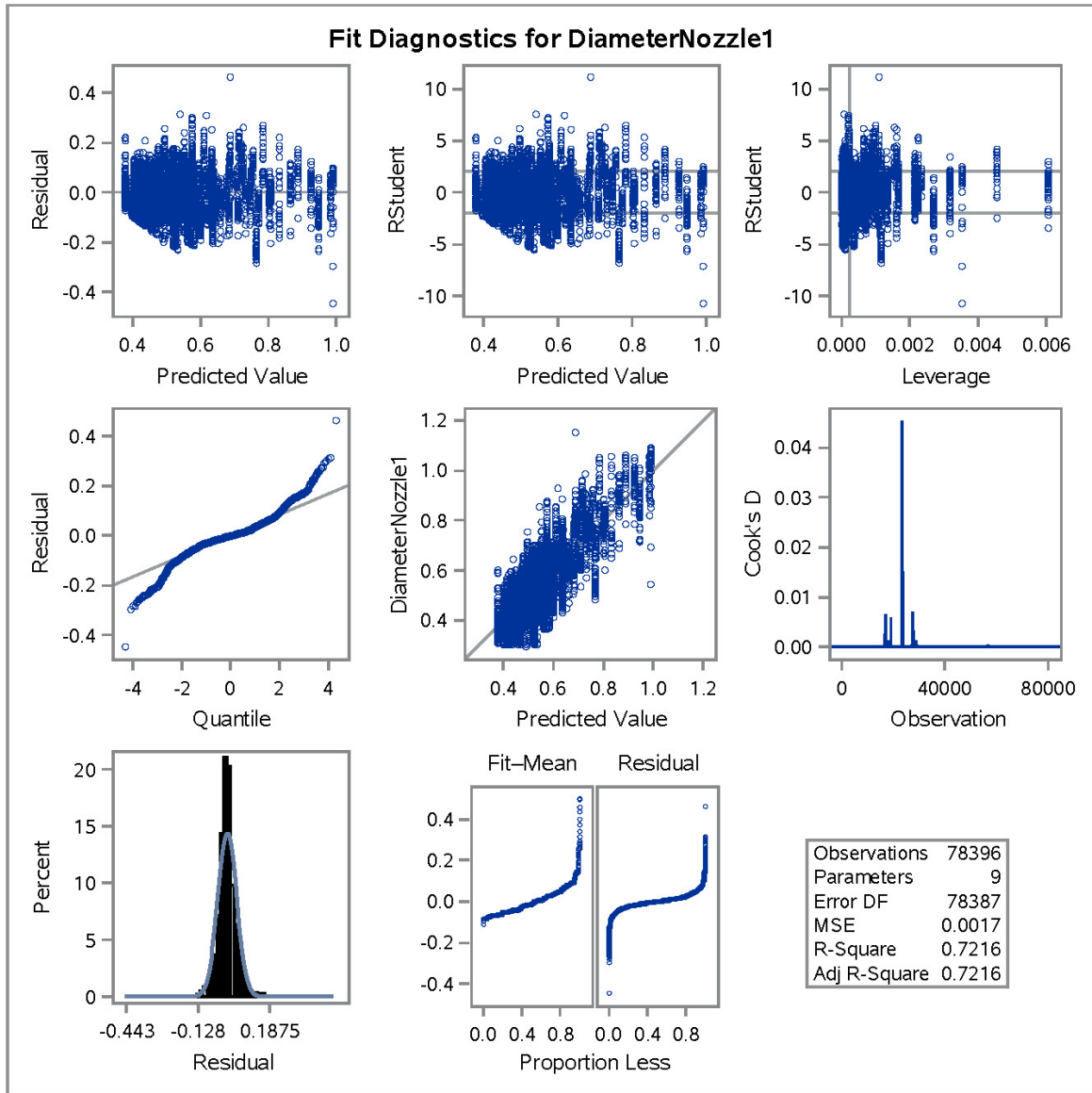


Figure 47: Neutrally and non-neutrally buoyant SAS data

All Nozzle 1 Data
The REG Procedure
Model: MODEL1
Dependent Variable: DiameterNozzle1

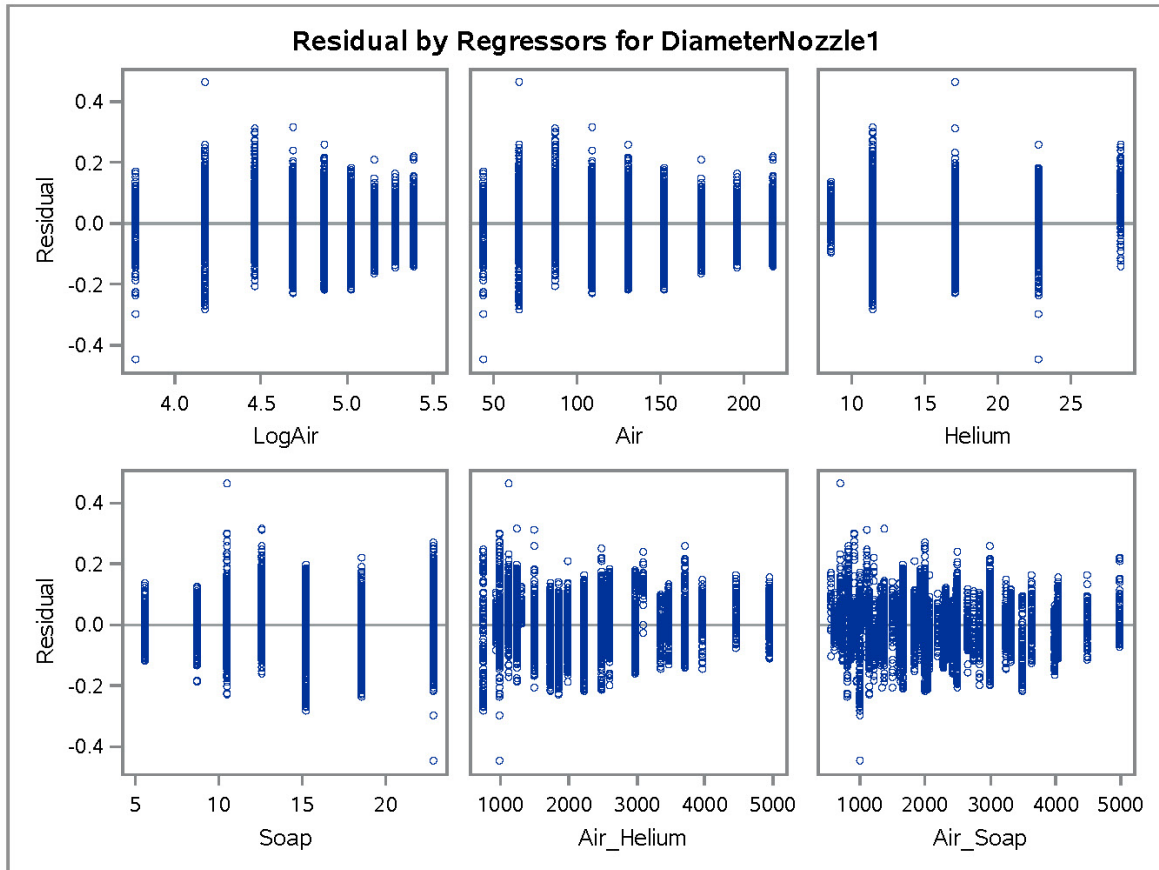


Figure 48: Neutrally and non-neutrally buoyant SAS data

All Nozzle 1 Data
The REG Procedure
Model: MODEL1
Dependent Variable: DiameterNozzle1

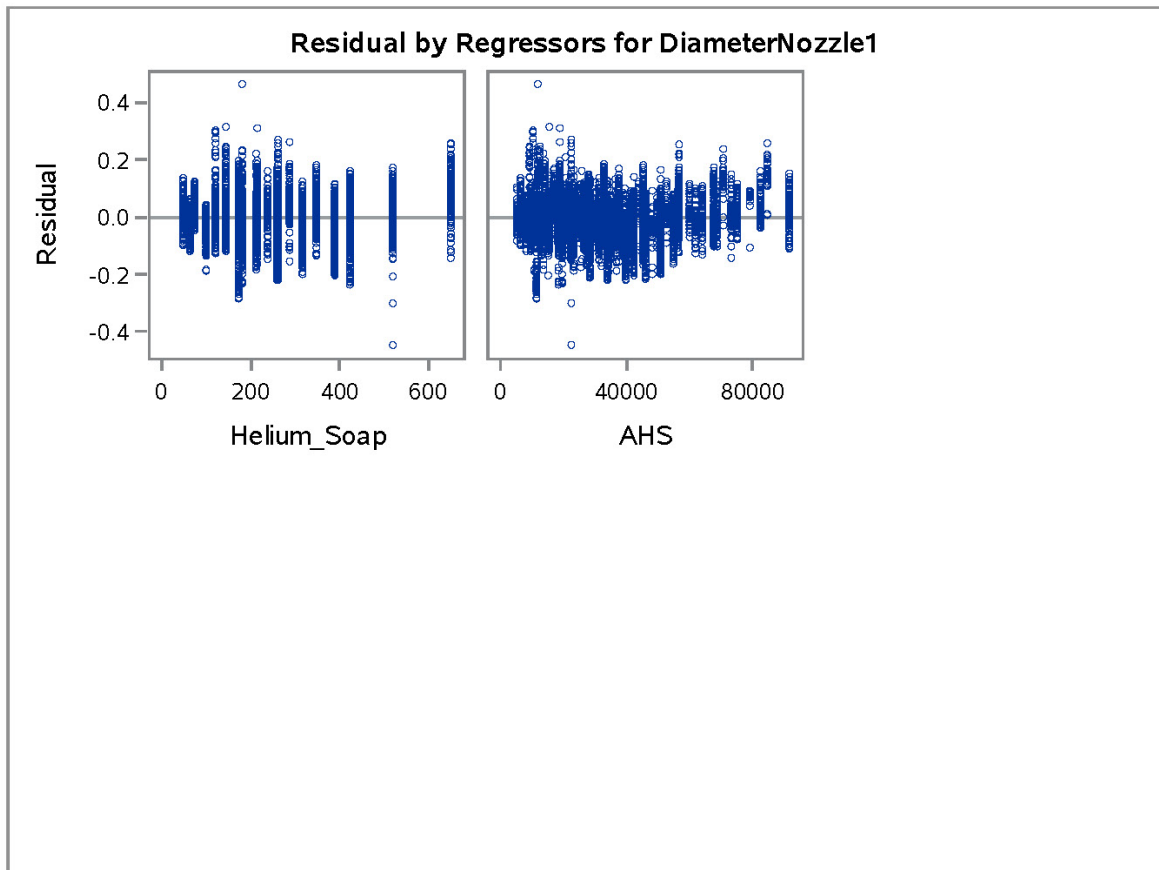


Figure 49: Neutrally and non-neutrally buoyant SAS data

Appendix F

Parts List

The parts list below was used to set up and run the HFSB system. The part list includes the Dwyer flow meters required to operate one nozzle (RMA-1-BV and RMA-1-BV) and multiple nozzles (RMB-49-SSV and RMB-52-SSV). Other parts could be used instead of the ones listed in the table. Lab equipment, such as tools, air hoses, and regulators were not placed in this part list. Additional adapters may be required depending on the air source and helium source being used.

Table 5: Parts list for HFSB system

Part Number	Supplier	Description	Quantity
301-100-580	Bakers Gas	Harris light duty single stage inert regulator	1
RMA-1-BV	Dwyer	Flow meter, .05-.4 SCFH	1
RMA-4-BV	Dwyer	Flow meter, .5-5 SCFH	1
RMB-49-SSV	Dwyer	Flow meter, .5-5 SCFH	1
RMB-52-SSV	Dwyer	Flow meter, 5-50 SCFH	1
CL 20ES	GE Additive	316L stainless steel powder	≈ 21 g / nozzle
1424T11	McMaster-Carr	Compact Plastic Backflow-Prevention, NPT Male	1
3847K71	McMaster-Carr	0-30 PSI Pressure Gauge, 1/8 NPT Male	1
3847K73	McMaster-Carr	PSI Gauge Panel Mount	1
4017T14	McMaster-Carr	Dual Shutoff Directional Control Valve, 1 × 3/4 × 3/4	1
44665K419	McMaster-Carr	2 NPT, 8" Long, Aluminum Pipe	1
44705K381	McMaster-Carr	2 NPT Male Cap	2
46095K21	McMaster-Carr	Direction-Control Valve, 1/8 NPT Female × Male × Female	1
4912K41	McMaster-Carr	Chrome-Plated Brass Ball Shut-off Valve	1
50785K181	McMaster-Carr	Reducer, 1/4 to 1/8 NPT Female	1
50785K187	McMaster-Carr	Straight Reducer with Hex Body, 3/4 × 1/2 NPT Female	2
50785K64	McMaster-Carr	Hex Bushing Adapter, 1/2 NPT Male × 1/8 NPT Female	2
50785K67	McMaster-Carr	Hex Bushing Adapter, 3/4 NPT Male × 1/8 NPT Female	1
50785K79	McMaster-Carr	Hex Bushing Adapter, 1 NPT Male, 3/4 NPT Female	1
50915K311	McMaster-Carr	Compression Fitting 1/8" Tube OD × 1/8" NPT Male	1
50925K233	McMaster-Carr	Reducer, 1/4 × 1/8 NPTF Female	1
50925K541	McMaster-Carr	Adapter, 9/16"-18 UNF Female × 1/4 NPTF Male	1
5111K522	McMaster-Carr	Push-to-Connect, Tee Connector, 1/8" Tube OD	1
5112K61	McMaster-Carr	Flexible Nylon Tubing, 1/8" OD, 50 FT	1
5233K51	McMaster-Carr	PVC Clear Tubing, 1/16" ID, 1/8" OD, 50 FT	1
5779K102	McMaster-Carr	Push-to-Connect, 1/8" Tube OD × 1/8 NPT Male	15
5779K123	McMaster-Carr	Push-to-Connect, 1/8" Tube OD × 1/8 NPT Female	4
SAI 1035	Sage Action, Inc.	SAI 1035 Bubble Film Solution	1
SS-SS2-VH	Swagelok	Stainless Steel Low Flow Metering Valve, 1/8 in.	1

Appendix G

MATLAB Code

The MATLAB code used to identify the diameter and the production rate of HFSB is displayed below. The directory levels and the folder and file names will need to be edited depending on where the bubble images are saved. In the HFSB diameter code, Fig. 50, the lines that calculate the average bubble diameter and range of diameters were only used as a self-check to ensure the code was working properly. All of the raw bubble diameter data was exported from MATLAB and imported into the statistical software SAS to calculate bubble diameter averages, ranges, standard deviations, and regression models. If the images being used in the code depict multiple bubbles in each image and every bubble that enters the frame does not leave by the subsequent image, the code will count the bubbles multiple times. To prevent duplicate bubble counts, either a search area would have to be established within the MATLAB script, or the image files would need to be trimmed to prevent the same bubble being counted more than once.

In the production rate code, provided in Fig. 51, the Excel table outputs the most common production rate for each data set. To calculate the average production rates and deviations, the FFT images that the script saves were used to plot a Gaussian curve to analyze the data. Any remaining noise in the FFT plots was truncated. The code performs a background subtraction to alleviate some of the noise in the FFT plots. A Gaussian curve was then fitted over the remaining data and confidence intervals and standard deviations were determined.

```

clc; clear all; close all;

imageDir = uigetdir(path);
radii_total=0;
totalavg=0;
quantity=0;
data=0;

filePattern = fullfile(imageDir, '*.jpg');
jpegFiles = dir(filePattern);

for ii=1:length(jpegFiles)

    currentfilename = jpegFiles(ii).name;
    fullFileName = fullfile(imageDir, currentfilename);
    currentimage = imread(fullFileName);
    files = length(jpegFiles); % Number of files found

    % Subtract Background if needed
    % I_back = imread('Background.jpg');
    % I_back = rgb2gray(I_back); % Convert color to grayscale
    % deltaImage = im2double(I_back) - im2double(currentimage);
    % imshow(deltaImage)

    % currentimage = rgb2gray(currentimage); % Convert color to grayscale
    figure % starting new figure in every loop
    imshow(currentimage); % Showing image

    % Getting centers and radius of found circles, set search diameter in
    % pixels and set sensitivity
    [centers, radii] = imfindcircles(currentimage,[4 8],
'ObjectPolarity','dark','Sensitivity',0.95);
    h = viscircles(centers,radii); %Plotting circles on figure
    radii_total=radii_total+sum(radii); %sum of all radii in data set

    average=mean(radii);
    quantity=quantity+length(radii); %total bubbles in data set
    totalavg=radii_total/quantity; %avg bubble size across all bubbles in data set
    N=size(radii);
    for k=1:N
        y=quantity-N+k;
        radii_matrix(y(:,1),1)=radii(k);
    end
end
close all

calibration = 2.2/45*2; %pixels to mm and converting to diameter
avgMatrix=mean(radii_matrix)*calibration;
HFSB_diam = totalavg*calibration;
max_diam = max(radii_matrix)*calibration;
min_diam = min(radii_matrix)*calibration;
fprintf('The quantity of HFSBs detected in the images is %g\n', quantity)
fprintf('The average diamter of all HFSBs detected is %g mm\n', HFSB_diam)
fprintf('The range of HFSB diamters in the image is between %g mm and %g mm\n', min_diam,
max_diam)

```

Published with MATLAB® R2020a

Figure 50: MATLAB code for calculating HFSB diameters

```

% HFSB Production Rate FFT
clc; close all; clear all

% NEEDS TO BE DYNAMICALLY CHANGED
numProductions = 1;
activeProduction = 1;

% Locating home directory
homeDir = pwd;

% Locating nozzle folder directory level
nozDir = uigetdir;
cd(nozDir)
nozDirStruct = dir(nozDir);
nozDirNames = {nozDirStruct.name};
location = pwd;

% Counting number of nozzles and productions to format subplot
totalNozzles = 0;
totalProductionsArray = [];
totalProductions = 0;
for nozDirNum = 1:length(nozDirNames)
    if contains(nozDirNames{1, nozDirNum}, 'converted_nozzle')
        cd(fullfile(nozDir, nozDirNames{1, nozDirNum}))
        prodDirStruct = dir(pwd);
        prodDirNames = {prodDirStruct.name};

        for prodDirNum = 1:length(prodDirNames)
            if contains(prodDirNames{1, prodDirNum}, 'Production')
                cd(fullfile(pwd, prodDirNames{1, prodDirNum}))

                totalProductions = totalProductions + 1;
                cd('../')
            end % if - production
        end % Production loop
        totalNozzles = totalNozzles + 1;
        totalProductionsArray = [totalProductionsArray; totalProductions];
        totalProductions = 0;
        cd('../')
    end % if - Converted
end % Converted Nozzle loop

% Moving back to 'location' to reset
cd(location)

% Excel table variables/plots
subPlotLoc = 1;
nozzleNameArray = [];
productionNameArray = [];
productionCountArray = [];
pwdArray = [];
activeBubbleArray = [];

```

```

for nozDirNum = 1:length(nozDirNames)
    if contains(nozDirNames{1, nozDirNum}, 'converted_nozzle')
        cd(fullfile(nozDir, nozDirNames{1, nozDirNum}))
        prodDirStruct = dir(pwd);
        prodDirNames = {prodDirStruct.name};

        for prodDirNum = 1:length(prodDirNames)
            if contains(prodDirNames{1, prodDirNum}, 'Production')
                cd(fullfile(pwd, prodDirNames{1, prodDirNum}))

                % Find Background Intensity if Needed
                image_nos = imageDatastore(pwd); % the path to the folder of
images
                A = imread('0002.jpg'); %image in data set to determine
background intensity

                figure('Name', sprintf('Select Background Point (%s)', pwd));
                imshow(A)
                [x_b,y_b] = ginput(1);
                close(sprintf('Select Background Point (%s)', pwd));

                intensity_background = [];
                while hasdata(image_nos)
                    img=read(image_nos);
                    intensity_background = [intensity_background,
img((floor(y_b)),(floor(x_b)))];
                intensity_background_avg = mean(intensity_background);
                end

                % Now looping through each of the bubbles
                % Active moving directory
                A = imread('0002.jpg');
                figure('Name', sprintf('Intensity Selection (%s)', pwd));
                imshow(A)
                % Enter how many points to select to determine frequency
                numBub = input('Number of Points you want to select: ');
                [x,y] = ginput(numBub);
                x = floor(x);
                y = floor(y);
                close(sprintf('Intensity Selection (%s)', pwd));

                for activeBubbleLocation = 1:numBub
                    intensity = [];
                    image_nos = imageDatastore(pwd);
                    while hasdata(image_nos)
                        img=read(image_nos);
                        intensity = [intensity,img((y(activeBubbleLocation)),
(x(activeBubbleLocation)))];
                    end
                    % WITH background subtract
                    intensity_datum = intensity_background_avg - intensity; % subtract
background, if images have noise

                    % WITHOUT background subtract
                    %intensity_datum = intensity;

```

```

Fs = 105356;           % Sampling frequency
T = 1/Fs;             % Sampling period
L = length(intensity); % Length of signal
t = (0:L-1)*T;       % Time vector
Y = fft(intensity_datum); %FFT of the corrected intensity signal
P2 = abs(Y/L);       % power of the FFT
P1 = P2(1:L/2+1);    % single sided power of FFT
f = Fs*(0:(L/2))/L; % computing frequency - x axis of the plot

% Save Production Count ~~~REPLACE~~~
productionCount = -1;

% Plotting
% subplot(totalNozzles, max(totalProductionsArray) , subPlotLoc)
figure
h(activeBubbleLocation)=plot(totalNozzles, max(totalProductionsArray));
h(activeBubbleLocation)=plot(f,P1);
hold on
    title(sprintf('%s %s Active Bubble Location: %f', nozDirNames{1,
nozDirNum},prodDirNames{1, prodDirNum}, activeBubbleLocation), 'Interpreter', 'none')
% ASSUMING the first 500 on the x-axis is invalid
[~, indexOfMax] = max(P1(500:end));
index_add_crop = indexOfMax + 499;
productionCount = f(index_add_crop);
xlim([500 inf]) % limiting x axis to remove initial outlier

P1_short=P1(500:end);
f_short=f(500:end);
f_short_size = length(f_short);
x_vector=1:f_short_size;
stdDev = std(P1_short);
mu=mean(P1_short);
export=[f_short;P1_short]';
i=1;
%Binning the data before fitting a normal curve
binlength=10;
start=1;
    for count=i:1:length(f_short)/10
        bin_x(count,:)=f_short(start:binlength);
        bin_xmean(:,count) = [mean(bin_x(count,:))];
        binlength=10+binlength;
        start=10+start;
    end

    i=1;
    binlength=10;
    start=1;
    for count=i:1:length(P1_short)/10
        bin_y(count,:)=P1_short(start:binlength);
        bin_ymean(:,count) = [mean(bin_y(count,:))];
        binlength=10+binlength;
        start=10+start;
    end
end

```

```

        % Excel file
        nozzleNameArray = [nozzleNameArray; convertCharsToStrings(nozDirNames{1,
nozDirNum})]];
        productionNameArray = [productionNameArray;
convertCharsToStrings(prodDirNames{1, prodDirNum})]];
        productionCountArray = [productionCountArray; productionCount];
        activeBubbleArray = [activeBubbleArray; activeBubbleLocation];

        saveas(h(activeBubbleLocation),sprintf('Figure_%d.png',activeBubbleLocation))
        close all

        end % bubble location loop
        cd('../')
    end % if - production
end % Production loop
end % if - Converted
end % Converted Nozzle loop

cd(homeDir)

% Getting date
fileName =
sprintf('output_%s.xlsx',datetime(datetime(now,'ConvertFrom','datetime'),'Format','dd_MM_yyyy_HH_m
m_ss'));

% writing most frequent production rate to table
statsTable = table(nozzleNameArray, productionNameArray, activeBubbleArray,
productionCountArray);
writetable(statsTable, fileName, 'sheet', 'stats');

```

Published with MATLAB® R2020a

Figure 51: MATLAB code for calculating production rate using FFT